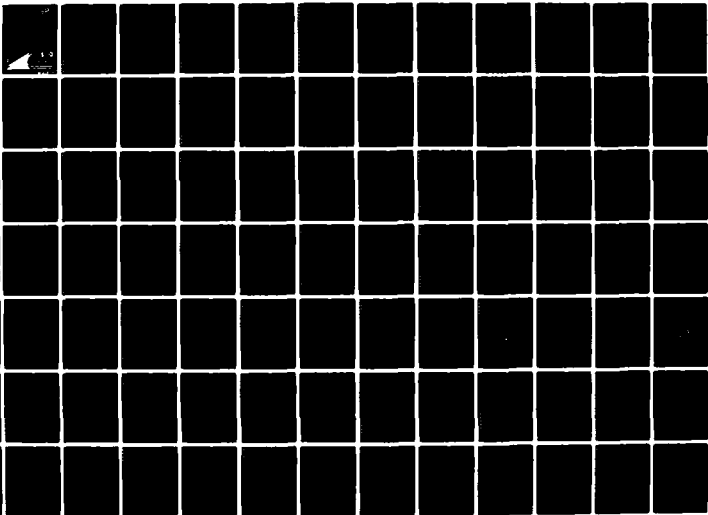


AD-A120 216

NIELSEN ENGINEERING AND RESEARCH INC MOUNTAIN VIEW CA F/G 20/4  
EULER SOLUTIONS OF SUPERSONIC WING-BODY INTERFERENCE AT HIGH IN--EYC(U)  
AUG 82 J N NIELSEN, G D KUHN, G H KLOPFER N00014-78-C-0490  
UNCLASSIFIED NEAR-TR-263 NL

1 of 2  
AD A  
120216



12

AD A120216

DTIC FILE COPY

DTIC  
ELECTE  
OCT 14 1982  
S D  
D

DISTRIBUTION STATEMENT A  
Approved for public release;  
Distribution Unlimited

**NIELSEN ENGINEERING  
AND RESEARCH, INC.**

OFFICES: 510 CLYDE AVENUE / MOUNTAIN VIEW, CALIFORNIA 94043 / TELEPHONE (415) 958-0457

22 10 18 186

EULER SOLUTIONS OF SUPERSONIC WING-BODY INTERFERENCE AT HIGH INCIDENCE INCLUDING VORTEX EFFECTS

by

Jack N. Nielsen, Gary D. Kuhn, and Goetz H. Klopfer

Accession For	
NTIS GRA&I	<input checked="" type="checkbox"/>
DTIC TAB	<input type="checkbox"/>
Unannounced	<input type="checkbox"/>
Justification	
By	
Distribution/	
Availability Codes	
Dist	Avail and/or Special
A	



NEAR TR 263  
August 1982

Prepared Under Contract No. N00014-78-C-0490

for

OFFICE OF NAVAL RESEARCH  
Arlington, VA 22217

by

NIELSEN ENGINEERING & RESEARCH, INC.  
510 Clyde Avenue, Mountain View, CA 94043  
Telephone (415) 968-9457

**DISTRIBUTION STATEMENT A**  
Approved for public release  
Distribution Unlimited

### Change of Address

Organizations receiving reports on the initial distribution list should confirm correct address. This list is located at the end of the report. Any change of address or distribution should be conveyed to the Office of Naval Research, Code 432, Arlington, VA 22217.

### Disposition

When this report is no longer needed, it may be transmitted to other organizations. Do not return it to the originator or the monitoring office.

### Disclaimer

The findings and conclusions contained in this report are not to be construed as an official Department of Defense or Military Department position unless so designated by other official documents.

### Reproduction

Reproduction in whole or in part is permitted for any purpose of the United States Government.



Unclassified

SECURITY CLASSIFICATION OF THIS PAGE(When Data Entered)

(Block 20 continued)

this purpose. A series of calculations for a wing-body combination with delta wings, at Mach numbers of 3, 4, and 5 and angles of attack up to  $25^\circ$  was made to demonstrate the feasibility of the use of the Euler equations to handle separated rotational flows. Some comparisons with experimental pressure distributions and fin load were made with good agreement. The Euler code was used to evaluate the accuracy of a panel method for calculating the wing-body pressure distributions as influenced by body vortices.

Unclassified

SECURITY CLASSIFICATION OF THIS PAGE(When Data Entered)

## SUMMARY

The work reported herein demonstrates the feasibility of applying the Euler equations to calculating flow about supersonic wing-body combinations at high angles of attack where significant effects of shock waves and flow separation occur. Body separation vortices and leading-edge separation from the wings are both present. It is necessary to input the body primary separation line locations to apply the Euler code. Special data correlations to yield these quantities were carried out.

To start the computations in a supersonic marching code for a sharp-nosed configuration, it was necessary to have initial solutions for circular cones with separated turbulent flow. Such solutions were developed which yield conical pressure distributions in good agreement with data.

The code was applied to a wing-body combination utilizing a cone-cylinder body and  $AR = 1$  delta wings. Calculations were performed for Mach numbers up to 5 and angles of attack up to  $25^\circ$ . The method is limited in angle of attack only by the angle of shock detachment for the cone. This limit could also be raised if starting solutions above shock detachment were available. The body pressure distributions are generally in good agreement with data. The fin normal force also agrees with experiment.

A special comparison was made between the load induced on the fins as determined by the Euler code and as calculated by a panel method. While gross loads were nearly equal, the spanwise variation of the pressure differed.

## PREFACE

This technical report covers the work performed under Contract N00014-78-C-0490 from December 1, 1980 to November 30, 1981. The program is sponsored by the Office of Naval Research, Arlington, Virginia. Dr. Robert E. Whitehead is the Scientific Officer.

## TABLE OF CONTENTS

<u>Section</u>	<u>Page No.</u>
1. INTRODUCTION	5
2. GENERAL CONSIDERATIONS	6
3. RÉSUMÉ OF CALCULATIVE METHOD	8
3.1 Coordinates and Mesh Generation	8
3.2 Governing Equations	10
3.3 Boundary Conditions at Bow Wave and Regular Points on the Solid Boundary	10
3.4 Boundary Conditions at a Sharp Subsonic Leading Edge	11
3.5 Boundary Conditions at Separation Lines on a Circular Body	12
3.6 Initial Conditions	13
4. PRIMARY SEPARATION LINE LOCATIONS	14
4.1 Circular Cylinders	14
4.2 Pointed Cones	17
4.2.1 Preliminary remarks	17
4.2.2 Description of available data	18
4.2.3 Correlation of the data	20
4.2.4 Applicable cone-cylinder results	22
5. CALCULATED RESULTS FOR POINTED CONES	23
5.1 Introductory Remarks	23
5.2 Starting Solution with No Kutta Condition	24
5.3 Solution with Kutta Condition	26
6. SAMPLE CALCULATIONS FOR WING-BODY COMBINATIONS	31
6.1 Introductory Remarks	31
6.2 Body Pressure Distributions and Loadings	32
6.3 Aerodynamics of the Finned Section of the Combination	34
7. EFFECTS OF ANGLE OF ATTACK AND MACH NUMBER ON LOADING OF EXAMPLE WING-BODY COMBINATION	36

<u>Section</u>	<u>Page No.</u>
8. COMPARISON OF BODY VORTEX EFFECTS PREDICTED BY EULER EQUATIONS AND A PANEL METHOD	39
8.1 Introductory Remarks	39
8.2 Comparison of Upwash Distributions	40
8.3 Comparison of Loading Distributions	41
9. CONCLUDING REMARKS	43
REFERENCES	47
APPENDIX A	49
LIST OF SYMBOLS	51
TABLES 1 THROUGH 2	53
FIGURES 1 THROUGH 24	59

## 1. INTRODUCTION

Wing-body interference at high angles of attack and high supersonic speeds is characterized by significant loss of fin lift (Ref. 1) and by the lack of good prediction methods to aid missile designers. The increased emphasis on airbreathing missiles, which usually utilize noncircular bodies, has further increased the need for a reliable and rapid predictive method.

For the low angle range and supersonic Mach numbers approaching 3, panel methods (Ref. 2) have proved useful. At angles above the linear range and Mach numbers above 3, the nonlinearities due to compressibility and vorticity require more powerful methods for their predictions. The Navier-Stokes equations represent a possibility in this connection, but their use for three-dimensional configurations requires large amounts of computer time. A viable alternative appears to be the Euler equations when used in the supersonic marching mode. This mode covers much of the range of angle of attack and Mach number of interest.

The Euler equations have been applied to supersonic missiles by investigators at the Naval Surface Weapons Center (Ref. 3) and by the present investigators (Refs. 1 and 4). The former investigators treated cases of attached flow while the present investigators have concentrated on separated flows. In Reference 1, the Euler equations were applied to a cruciform wing-body combinations at zero roll angle with fins having subsonic leading edges. A Kutta condition was imposed at the sharp leading edges to make the computer solution unique, and the entire flow field without body vortices was calculated. In Reference 4, a special study was made of generating body vortices with the Euler code, and a method developed which calculates the flow field well except near secondary separation. (The method can include secondary separation within its framework.) The primary purpose of the present study is to adapt

the methods previously developed to the calculation of wing-body interference with the effects of compressibility and vortices both present. Subsonic leading edges are treated.

This report, after discussing the general background of the problem, gives a résumé of the new calculation method leaving the mathematical details to the earlier reports. Since the location of the primary separation line is an input to the method, the report next addresses this question. A number of calculative examples of wing-body interference are discussed to illustrate the nature of the phenomena as a function of angle of attack and Mach number. Finally, the Euler method is used to investigate the accuracy of panel methods for calculating the effect of body vortices on fin loading.

The work herein was carried out under Office of Naval Research Contract No. N00014-78-C-0490 under the scientific direction of Dr. Robert E. Whitehead.

## 2. GENERAL CONSIDERATIONS

The present investigation is not meant to develop a production computer code for supersonic cruciform wing-body combinations, but is meant to develop the necessary methodology leading to such a code. The present calculations are limited to cruciform wing-body combinations at zero roll angle although the mathematical steps to handle non-zero roll angle are clear. The Mach number range is supersonic and is specifically limited to that angle-of-attack range for which the axial Mach number is supersonic. For subsonic axial Mach numbers, problems can be solved by using the unsteady Euler equations and calculating hyperbolically in time at considerable expense in computer time.

At the present time sharp-nosed bodies of revolution are being considered. As long as a cone solution is available for the given angle of attack and Mach number to start the solution, it should proceed subject to the limitation of axial supersonic

Mach number. If a blunt nose is used, the solution can proceed behind any station of the starting solution for which the axial Mach number exceeds unity everywhere. For noncircular bodies of revolution, the solution can still be carried out if an appropriate starting solution is available or can be generated.

In the present work any pointed body of revolution can be handled; cone-cylinders, ogive-cylinder, etc. However, the wings generally have thickness distributions of a kind which correspond to blended wing-body junctures. This results from the way in which conformal mapping is used in the method.

The flow around wing-body combinations at supersonic speed and moderate to high angles of attack is dominated by compressibility and vortex nonlinearities. The Navier-Stokes equations are applicable to these flows but take much computer time. The application of the Euler equations to these problems is motivated by the possibility of getting faster solutions and by the fact that diffusion of vorticity not accounted for by the Euler equations is of little importance in many problems of missile aerodynamics. The convection of vorticity as in trailing vortices is of importance, and can be accounted for by the Euler equations provided the vorticity is properly introduced into the flow. The vorticity generated at curved shock waves is generated external to the solid surfaces and appears in the Euler solutions. The vorticity which arises at the surface such as body vortices or leading-edge vortices, must be controlled in the Euler equations by use of appropriate boundary conditions.

The conditions required to control the vorticity discharged into the flow at solid boundaries include a knowledge of the separation line locations together with additional conditions required to tie down all the dependent variables. In the first year's work, we showed how the Kutta condition at a subsonic leading edge plus certain auxiliary boundary conditions were sufficient to allow calculation of separated flows about wings

alone and the fins of wing-body combinations. The problem here is simplified by the fact that the separation location at the sharp leading edge is known.

For bodies the locations of the separation lines at supersonic speeds are not well known. We will subsequently enlarge on this subject as an aid in applying the Euler equations to the problem. However, the position of the separation line is not enough information to tie down all the dependent variables. Certain other conditions relating to the direction of the vortex lines leaving the separation line were used together with mean value conditions for the pressure and density in the separation sheet at separation. These conditions were sufficient to determine the rate of vorticity shedding at the separation point as shown by comparison (Fig. 22, Ref. 4) with the data of Oberkampf (Ref. 5). A parametric study of the boundary conditions revealed a general insensitivity of the flow field to the directions of the vortex sheets leaving the separation line.

### 3. RÉSUMÉ OF CALCULATIVE METHOD

A complete description of the mathematical method is lengthy and is contained in References 1 and 4. However, a résumé of the method is given here as an aid to the future sections of the report.

#### 3.1 Coordinates and Mesh Generation

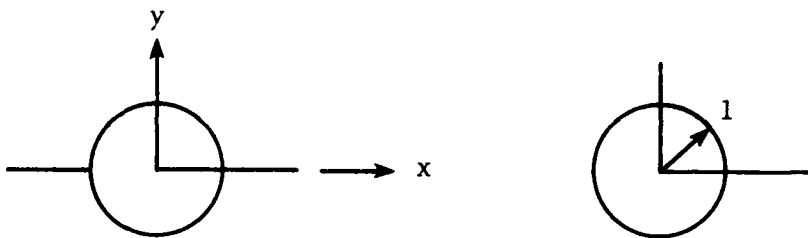
The physical coordinate system is an  $x,y,z$  Cartesian system as shown in Figure 1 for a cone-cylinder combination. The origin is at the apex of the cone with the  $z$ -coordinate rearward. The  $y$  coordinate is vertically upward. At each section the configuration has a cross section which is mapped conformally into the unit circle in the transformed space. This transforms the body or wing body into a cylinder. The bow wave is generally not concentric with the body. Accordingly,

with the cylinder fixed, a radial linear transformation which depends on  $\phi$  is applied to make the bow wave concentric with the body.

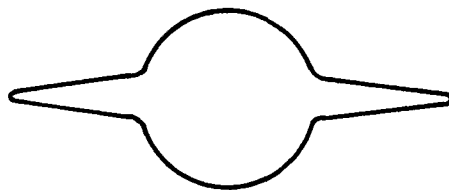
$$\xi = \frac{r - r_b}{r_s - r_b} \quad (1)$$

This makes  $\xi = 0$  on the body and unity on the bow wave. An orthogonal mesh can now be laid out and carried back to the transformed space and physical space where it is no longer orthogonal.

Under these transformations, the metric terms are obtained algebraically from the transformation equations. For a wing-body cross section the Joukowski transformation carries it into a circle as shown. The Jacobian of the transformation



shows singularities at the tip of a sharp wing or at the wing-body juncture. To avoid the singularity at the wing-body juncture, the contour of the configuration has been taken as a circle of radius  $1 + \epsilon$ , where  $\epsilon$  is a small number. The resulting wing-body combination is blended as shown in the following sketch:



The singularity at the leading edge of the fin is handled by a Kutta condition as subsequently described.

### 3.2 Governing Equations

The governing equations for the steady inviscid flow of an ideal compressible fluid in three dimensions, are the Euler equations. In Cartesian coordinates the equations are

$$\frac{\partial \hat{E}}{\partial x} + \frac{\partial \hat{F}}{\partial y} + \frac{\partial \hat{G}}{\partial z} = 0 \quad (2)$$

where  $\hat{E}$ ,  $\hat{F}$ , and  $\hat{G}$  are defined as

$$E = \begin{bmatrix} \rho u \\ \rho u^2 + kp \\ \rho uv \\ \rho uw \end{bmatrix} \quad F = \begin{bmatrix} \rho v \\ \rho uv \\ \rho v^2 + kp \\ \rho vw \end{bmatrix} \quad G = \begin{bmatrix} \rho w \\ \rho uw \\ \rho vw \\ \rho w^2 + pk \end{bmatrix}$$

The equations involve five dependent variables, three velocity components,  $u$ ,  $v$ , and  $w$  and two thermodynamic variables of state,  $p$  and  $\rho$ . Another relationship is provided by the constancy of total temperature or total enthalpy. These equations in the transformed space are still fully conservative, but the radial stretching operation to make the bow shock correspond to  $\xi = 1$  makes the equations quasi-conservative.

### 3.3 Boundary Conditions at Bow Wave and Regular Points on the Solid Boundary

At the bow wave, the Rankine-Hugoniot relationship must be satisfied. By utilizing information for data at the shock and one point below the shock, a prediction-correction scheme is used to determine the shock shape as the calculation proceeds axially.

The flow normal to the wing-body surface at all nonsingular points must be zero for steady flow. The values of the

dependent variables are calculated at the next station on the body using the MacCormack prediction-correction scheme used for the body tangency condition. A scheme due to Abbett (Ref. 6) is used to correct the boundary values. In this prediction-correction scheme, simple expansion or compression waves are used at the surface in the tangent plane. The possibility of correcting the surface values of the entropy for shock waves which reach to the body surface is included. The boundary conditions are applied at the wing and body surfaces.

#### 3.4 Boundary Conditions at a Sharp Subsonic Leading Edge

At a wing tip the metric can be expanded in powers of small perturbations of the radial and angular variables from their values at the wing tip. Using those results to expand the Euler equations in the neighborhood of the wing tip, it is found (Ref. 1) that the equations are indeterminate. Accordingly, the Euler equations are satisfied by any continuous values of the variables approaching the wing tip. It was also found that the same is true of jump conditions across any sheet of discontinuity at the tip. Accordingly, we have five independent conditions that can be specified at the subsonic edge. The three conditions which we have chosen to use on the basis of physical arguments are:

1. The static pressure is continuous across the sheet.
2. The vortex sheet leaves the leading edge in the  $y = 0$  plane (Kutta condition).
3. The total enthalpy is constant.

The other two conditions which have been specified are:

4. The density at the wing tip is the average of the density on the wing on each side of the sheet.
5. The initial direction of the vortex lines in the sheet is the average of the boundary streamlines just inboard of the tip on the upper and lower

surfaces provided it is outboard. Otherwise it is taken tangent to the wing leading edge.

These conditions are adequate to remove the indeterminateness of the Euler equations at the leading edge. The significance of each of these conditions in determining the gross flow is another matter.

### 3.5 Boundary Conditions at Separation Lines on a Circular Body

At a separation line on a circular or noncircular body, the Euler equations are not indeterminate as at a sharp subsonic leading edge. However, the tangency condition is not valid. The flow variables,  $u$ ,  $v$ ,  $w$ ,  $p$ , and  $\rho$  must satisfy the conditions for a tangential discontinuity. What we have done is let the Euler equations capture the discontinuities which are determined by global conditions, not local conditions. We rather express the mean values in the sheet based on various physical assumptions.

1. The pressure across the sheet is continuous. This is expressed by the equation that the static pressure at separation is the average of the body pressure above and below the separation line.
2. The mean density within the sheet is specified by a relationship similar to that for the pressure.
3. The total enthalpy is constant.

In addition to these conditions, certain conditions on the position and direction of the vortex lines at separation are also needed to close the problem. Figure 2 shows three angles which specify this information for the vortex lines leaving the surface of a round body. The angle  $\phi_s$  specifies the polar angle of the separation line in the crossflow plane. The angle  $\phi_c$  is the angle of the plane containing the separation line and the velocity vector with respect to the tangent plane. The angle  $\phi_a$  is related to the sweepback of the

velocity vector, being the complement of the sweepback angle. The velocities  $u_o$ ,  $v_o$ , and  $w_o$  at the separation point are:

$$\begin{aligned}u_o &= q_o \sin\phi_a \cos(\phi_s - \phi_c) \\v_o &= q_o \sin\phi_a \sin(\phi_s - \phi_c) \\w_o &= q_o \cos\phi_a\end{aligned}\tag{3}$$

In these equations, the two angles  $\phi_a$  and  $(\phi_s - \phi_c)$  yield the ratios  $u_o/q_o$ ,  $v_o/q_o$ , and  $w_o/q_o$ . The three conditions above yield  $q_o$  so that  $u_o$ ,  $v_o$ , and  $w_o$  are known from Equation (3). The first two conditions yield  $p_o$  and  $\rho_o$ . Thus, five conditions yield the five dependent variables at separation.

A parametric study (Ref. 4) of the flow dependence on  $\phi_a$ ,  $\phi_c$ , and  $\phi_s$  indicates that the rate of vortex shedding and the height of the separation region are insensitive to the values of the first two parameters. The important parameter is  $\phi_s$ .

### 3.6 Initial Conditions

It is necessary to initialize the program at some axial station at which a crossflow solution is known. The common case is that of a pointed body of revolution which is initialized by the solution for the tangent cone to the nose at the given Mach number and angle of attack. If a cone solution close to the desired solution is known, it can be used to determine the precise starting solution. If a certain cone half angle is needed, for instance, we can start the solution with a known half angle and then change to a different half angle as soon as the calculation is started. The solution is then continued downstream until the effect of the initial solution has died out. This is determined by testing the solution for conical flow as it proceeds downstream. This procedure is valid up to the shock-detachment angle of attack.

The present program can also be used to study wing-alone characteristics at high angles of attack. The solution is started with a known solution for a cone, but the cross section is changed from a circle to an ellipse of high eccentricity as the calculation proceeds downstream to form a wing. Again the solution is carried downstream until it is conical to generate a starting solution for the real wing. While not all wings of interest can be handled this way, many can.

In some cases bodies have blunt noses which cause detached bow waves and imbedded subsonic flow regions. In this case the starting solution can be generated by an unsteady Euler code (Ref. 7), and the marching program can be engaged downstream of the region of imbedded subsonic flow. A question arises concerning how to start a solution for a body with a conical nose when separation starts at the apex. This point will be subsequently addressed.

#### 4. PRIMARY SEPARATION LINE LOCATIONS

##### 4.1 Circular Cylinders

The location of the separation point for circular cylinders is of interest for what light it might shed on the location of the separation point on the cylindrical part of a body of revolution. One does not have to go very deeply into the subject to appreciate the complexity of the problem for the circular cylinder. In this connection consider Figure 3 from Reference 8 which shows the separation positions on smooth circular cylinders as a function of Reynolds number for incompressible flow. In the subcritical region the boundary layer is laminar at the separation point with no reattachment. In the critical region a laminar separation bubble forms with turbulent reattachment and subsequent turbulent separation. In the supercritical region the transition occurs in front of separation and the separation is all turbulent. The separation

locations were determined from local skin-friction measurements.

The effect of Mach number on the location of the separation point is of interest as it might apply to estimation of primary separation lines on bodies of revolution at angles of attack. The increase of Mach number up to about  $M_\infty = 0.4$  will not cause any part of the flow to exceed the speed of sound, but above this Mach number inviscid flow theory predicts imbedded regions of supersonic flow and shock waves. It could be expected that the shock waves would have an effect on separation, and if strong, may control the position of separation.

Very little data are available on this point, the recent work (1977) of Murthy and Rose (Ref. 9) being a notable exception. Some interesting facts can be gleaned from a study of these data, which include the critical and supercritical regimes. The ranges of the test parameters are:

$$\begin{aligned} .083 \times 10^5 \leq Re_D \leq 0.5 \times 10^6 \\ 0.25 \leq M_\infty \leq 1.2 \end{aligned}$$

The Reynolds number is based on cylinder diameter. For  $M_\infty \geq 0.5$  and  $Re_D = 0.5 \times 10^6$  boundary-layer transition occurs on the front of the cylinder, and the separation appears to be turbulent. It is of interest that this supercritical state is achieved at a Reynolds number for which the data of Achenbach (Fig. 3) are in the critical regime. This result may not be entirely due to compressibility.

The following separation points were obtained (Ref. 9) from the skin-friction measurements made by a buried wire with supercritical crossflow.

<u>Re</u>	<u>M<sub>∞</sub></u>	<u>Fig.</u>	<u>φ<sub>sep</sub></u>	<u>φC<sub>p</sub><sub>min</sub></u>	<u>Δφ</u>
0.5 × 10 <sup>6</sup>	0.6	9	82° <sup>1</sup>	75°	7°
0.5 × 10 <sup>6</sup>	0.8	10	80°	73°	7°
0.5 × 10 <sup>6</sup>	1.0	12	105°	99°	6°
0.5 × 10 <sup>6</sup>	1.2	14	108°	102°	6°

<sup>1</sup>Estimated by extrapolating the  $c_f$  curves.

These points, shown in Figure 4 as a function of Mach number, indicate a strong effect of Mach number. In Figure 5 a plot is shown of the skin friction and pressure distribution around the cylinder for the  $M_\infty = 0.8$  case. The data exhibit the interesting phenomenon that the pressure becomes uniform for  $\phi > 75^\circ$ , but separation is not seen until  $\phi \approx 80^\circ$ . An angular separation between minimum pressure onset and separation of about  $6^\circ - 7^\circ$  occurs at nearly constant pressure. There is no pressure rise in the experimental pressure distribution before separation which can be used to estimate the separation point by such criteria as that due to Stratford (Ref. 10). It appears that the separation position may be controlled by some other mechanism than an adverse pressure gradient in the Stratford sense.

Another noteworthy fact is that there is no evidence of a shock wave in any of the surface pressure distributions although a weak one might exist. Somehow the boundary-layer separation must act to eliminate the shock pressure discontinuity at the surface. This raises the conjecture of whether separation occurs at or near the shock location. Let us examine this question by comparing theoretical and experimental results. The use of potential theory and CFD calculations will yield a position of the theoretical shock position. Such a calculation for  $M_\infty = 0.51$  is given in Reference 11. This point is shown in Figure 4 for comparison with the experimental separation-point locations. It is clearly well behind the

probable position of the separation point. This is not surprising in view of the fact that the full potential equation is known to calculate shock locations behind the experimental ones for airfoils in transonic flow.

We will address the question of the application of the circular cylinder results to the cylindrical portion of bodies of revolution at angle of attack subsequently.

## 4.2 Pointed Cones

4.2.1 Preliminary remarks. If a cone is pitched up to an angle of attack equal to its half angle,  $\theta_c$ , the top meridian is parallel to the free stream and the local pressure is close to the free-stream pressure. Further increases in angle of attack are usually accompanied by separation on the leeward side of the cone starting at the top meridian and moving downward as the angle of attack is increased. It is observed experimentally that flow separation occurs along a straight line at a constant value of azimuth angle,  $\phi_s$ . The flow pattern on the attached side of the cone appears conical even for a finite cone. It is known that the position  $\phi_s$  depends on the ratio  $\alpha/\theta_c$  to a significant degree.

Another parameter that might be expected to have a significant effect on the value of  $\phi_s$  is the crossflow Mach number. If we draw an analogy between the flow in the crossflow plane of a cone and that for a circular cylinder at the same crossflow Mach number, we might expect a change in the qualitative nature of the flow with increases in Mach number when supersonic flow occurs in the crossflow plane. For this reason the data for  $M_n$  greater than a certain value might be expected to correlate differently than that for Mach numbers less than this value.

An interesting discussion of the flow over cones, including separated flow, treating both experiment and theory is given by Peak and Toback in Reference 12. In that reference the

authors have collected together some of the data on primary cone separation angle,  $\phi_{s1}$ . Both laminar and turbulent flow are represented as well as low and high crossflow Mach numbers. We will now discuss the available data before presenting the correlations.

4.2.2 Description of available data. We will first consider the data on primary separation for cones from a number of references. Probably the best collection of data is that of Rainbird in Reference 13, Figure 14. Rainbird tested cones with  $\theta_c = 5^\circ$  at  $M_\infty = 1.8$  and 4.25 over a wide angle-of-attack range. The measurements were made in the NAE 5-Ft Trisonic Blowdown Tunnel on a 54-inch long cone. The turbulence and noise of the tunnel induced early transition within 10 percent of the body length from the nose. The cone had essentially the same temperature as the tunnel total temperature so that little heat transfer occurred. The location of the separation and attachment lines was determined using the oil-film technique. Results on a 40.6-inch long cone of  $\theta_c = 12.5^\circ$  are also available from tests under similar conditions. In Reference 14 the data for the  $12.5^\circ$  cone are presented, but no further primary separation data are included not already contained in Reference 13. The results are given in Table 1.

Another useful set of data is given by Nebbeling and Bannink in Reference 15. Their cone of half angle  $7.5^\circ$  was tested in two supersonic blowdown wind tunnels at the University of Technology, Delft. The 0.27m by 0.27m tunnel was used to provide flow-surface visualization. A mixture of oil, detergent and titanium dioxide was used as a surface film to provide the flow visualization. The tests were conducted at  $M_\infty = 2.94$  at a Reynolds number per meter of  $5 \times 10^7$ . Data on the secondary separation line position,  $\phi_{s2}$ , are also given. The results agree with the turbulent flow results of Rainbird (Ref. 13). The model was cooled down during the runs but it is thought that the heat transfer rate was small. The flow visualization pictures are of excellent detail and quality.

McElderry (Ref. 16) provides some data on separation line position at  $M_\infty = 6.0$ . His tests were performed in the 50-inch continuous flow hypersonic wind tunnel of the AEDC von Kármán facility with pointed and blunted cones. The nominal test conditions were:  $M_\infty = 6.05$ ,  $Re/ft = 5 \times 10^6$ ,  $P_o = 280$  psia,  $T_o = 850^\circ R$ . The model surface temperature started out well below the tunnel stagnation temperature. Based on a model length of 38.06 in., the Reynolds number based on length is about  $1.27 \times 10^7$ . The flow visualization was carried out using a white pigmented silicone oil on the dark model. The model was inserted into the airstream for a few minutes and then photographed from top and side viewing ports. Data are given for the primary and secondary line location for a blunted cone. The data are for the turbulent separation region which occurred behind the tip of the cone. There is a band of  $\phi$  given in Figure 12 of Reference 16 which is included in the results of Table 1. It was noted that at  $\alpha/\theta_c$  of unity, flow separation had not appeared.

Peake, Fisher, and McRae (Ref. 17) have conducted a combined wind tunnel, flight, and analytical investigation of the flow about a cone of  $5^\circ$  semiapex angle. The wind-tunnel tests were conducted in the Ames Research Center 6- by 6-Foot Supersonic Wind Tunnel. The flight tests were conducted with the cone mounted on a nose boom on an F-15 airplane. The cone was 44.5-inches long with roughness at 4.9 inches from the apex to ensure early transition. Since oil film techniques were not appropriate to determine separation line locations, obstacle blocks were used. The obstacle blocks were similar to a total-head tube flush with the cone surface. The measured results are given in Table 1. The correspondence between the flight results and the wind-tunnel results is remarkable.

Feldhuhn and Pasiuk (Ref. 18) have also provided data on primary and secondary separation-line position for a cone of  $5^\circ$  semiapex angle at a Mach number of about 6.0. Their tests were conducted in the hypersonic tunnel of the old Naval

Ordnance Laboratory. The cone was sting supported and had a slightly blunted nose of radius .0313 in. compared to a base diameter of 1.25 in. The overall length was 13.967 in. The separation-line locations were determined using flow visualization based on a mixture of lamp black and silicone oil. After application of the mixture, the model was shielded while the tunnel was started. The model was exposed to the flow for about 30 seconds and then was again shielded. Measurements of the angular position of the separation lines were made outside the tunnel at length stations of 5.7, 8.5, and 11.4 in. The angular positions are accurate to about  $\pm 5^\circ$ . Secondary separation was found for angles of attack of  $20^\circ$  or less. The data are given in Figure 25 of Reference 18. The data are for a highly-cooled cone.

4.2.3 Correlation of the data. A correlation of the data of Table 1 was developed from the observation that the static pressures on cones for the supersonic case can be shown to follow an hypersonic similarity law of the following type.

$$P = \frac{P}{1/2 \rho V_\infty^2 \sin^2 \alpha} = f \left( \frac{\alpha}{\theta_c}, M_\infty \alpha \right) \quad (4)$$

Neglecting differences between the sine of an angle and the angle itself, Equation (4) can be changed to an equivalent form

$$P = \frac{P}{q_\infty \sin^2 \alpha} = F \left( \frac{\alpha}{\theta_c}, M_n \right) \quad (5)$$

where  $F$  is a new function. The quantity  $q_\infty \sin^2 \alpha$  is the component of  $q_\infty$  in a direction normal to the cone axis within the small angle approximation. If a cone of small semiapex angle at angle of attack can be thought of as a swept wire, then the simple-sweep laminar flow analogy of R.T. Jones, Reference 19, can be invoked. In this case the flow in the crossflow plane completely determines the viscous flow. Assuming that the

form of the azimuthal pressure distribution still follows Equation (4) even with separated flow, then the primary separation point location,  $\phi_{s1}$ , should depend only on  $\alpha/\theta_c$  and  $M_n$ . This functional relationship thus suggests the form of a trial correlation. Another noteworthy point is that generally separation on a cone starts approximately at  $\alpha = \theta_c$ . If  $\phi_{s1}$  is plotted versus  $\alpha/\theta_c$ , the lines for different values of  $M_n$  should thus have a common point near  $\alpha/\theta_c = 1$

With regard to correlating the separation angle  $\phi_{s1}$  versus  $\alpha/\theta_c$  for various  $M_n$  certain statements can be made. It is suspected that for subcritical crossflow Mach numbers the data should correlate differently from those for supercritical crossflow Mach numbers. This turns out to be the case if  $M_n < 0.6$ . For the transonic range taken to be  $0.6 < M_n < 1.2$  deviations from the correlation for  $M_n < 0.6$  would be anticipated. The  $0.6 < M_n < 1.2$  correlation might be expected to hold for  $M_n > 1.2$  since the separation point is now controlled by crossflow shocks rather than by smooth pressure rise as for  $M_n < 0.6$ . Accordingly, we now have correlated the data differentiating three ranges of Mach number

$$0 < M_n \leq 0.6$$

$$0.6 < M_n \leq 1.2$$

$$1.2 < M_n$$

The resultant correlation is shown in Figure 6. The symbols are defined in Table 1.

Figure 6 exhibits a number of interesting points. Consider the circles for a  $12.5^\circ$  cone and the diamonds for a  $7.5$  degree cone. They both exhibit a sharp decrease in  $\phi_{s1}$  as  $M_n$  becomes greater than  $M_n = 0.6$ . All the data correlate on two lines as shown within fairly good accuracy. (This does not prove that all other data will fall into the correlation since tests varying  $M_n$  and  $\alpha/\theta_c$  systematically are not available.) As  $M_n$  exceeds  $0.6$  the value of  $\phi_{s1}$  falls from the upper curve

to the lower curve. While the correlation shows a discontinuous change at  $M_n = 0.6$ , the actual change is steep but continuous.

It is noted that  $\phi_{s1}$  does not approach  $180^\circ$  at  $\alpha/\theta_c = 1$  but a small region of separated flow is indicated. Questions will arise for cones of large  $\theta_c$  when  $M_n$  exceeds 0.6 for values of  $\alpha/\theta_c$  less than unity. Our data do not span this regime.

We now consider how the foregoing information can be used in predicting the primary separation lines for cone-cylinder combinations.

4.2.4 Applicable cone-cylinder results. In addition to the data already discussed, a systematic series of oil-flow pictures is available for a cone-cylinder combination for a wide range of angles of attack and Mach numbers. The investigation was carried out by Landrum and Babb (Ref. 20) on a  $9.47^\circ$  half-angle cone followed by a cylinder  $3\text{-}2/3$  diameters long. The angle of attack range was  $-4^\circ$  to  $60^\circ$  and the Mach number range was 1.6 to 4.63. Oil-flow pictures are given for the entire range of angle of attack and Mach number from which values of the cone primary separation angle can be measured. An index line for  $\phi = 90^\circ$  helped greatly in this process, but nevertheless the accuracy of the estimated angles of  $\phi_{s1}$ , are estimated to be  $\pm 7.5^\circ$ . The method of estimating the angle of the primary separation line from the photographs of the oil flow pattern is described in Appendix A. The positions so obtained are summarized in Table 2.

Table 2 gives the measured separation line positions both on the conical nose and on the cylindrical part of the cone-cylinder body over wide Mach number and angle-of-attack ranges. We now consider the measured angle near the base of the body at  $x/l = 0.925$  and compare these with the angles for circular cylinders in normal crossflow in Figure 4. Following Figure 4 and the correlation of Figure 31 in Reference 21, we have plotted  $\phi_s$  versus crossflow Mach number  $M_n$  for all the

data, and the results are presented in Figure 7. As  $M_n$  increases from a subsonic value, the value of  $\phi_{s1}$  increases and becomes fairly constant above  $M_n = 1.2$  at a value of about  $110^\circ$ . The shape of the correlation is similar to that of Figure 31, Reference 21, since the data for the two correlations overlap. However, the present correlation goes up to  $M_n = 4.0$  while the former goes up only to  $M_n = 1.9$ . It seems clear that the data from the circular cylinder in normal crossflow and the cone-cylinder bodies at angle of attack correlate well together.

As a matter of interest, let us see how the correlation curves of Figures 6 and 7 predict the primary separation angle locations on the cone-cylinder body of Reference 20 on the cone at  $x/l = 0.325$  and on the cylindrical part of the body at  $x/l = 0.925$ . Since the data from these runs have been used in the correlation of Figure 7, we expect accuracy of prediction at  $x/l = 0.925$  to be within the scatter of correlation. However, the prediction of  $x/l = 0.325$  is based solely on cone-alone data. The comparisons are made in Figure 8 for four Mach numbers. Examining first the comparisons for  $x/l = 0.925$ , we see that the agreement is within the scatter of Figure 7 as expected. Examining now the comparisons for  $x/l = 0.325$ , we see the agreement is almost as good as for  $x/l = 0.925$  except at  $M_\infty = 1.60$  at  $\alpha = 20^\circ$ . This condition is just before the onset of the transonic regime at  $M_n = 0.6$  as shown on the abscissa. The rapid fall in  $\phi_s$  for a cone alone at this Mach number could explain this disagreement.

## 5. CALCULATED RESULTS FOR POINTED CONES

### 5.1 Introductory Remarks

To start the calculations for most supersonic missile configurations, a sharp cone is fitted to the nose and the cone solution is used for the initial conditions. For sharp cones

up to an angle of attack approximately equal to the cone semi-apex angle, the flow is attached and no particular problem exists in determining the starting solution. However, for angles of attack above the semiapex angle, the flow is usually separated and a question arises concerning the proper starting solution. We have observed in the previous section that experimentally separated flows on cones are essentially conical. What we now consider is the starting solution for the cone with  $\alpha/\theta_c$  greater than unity with and without a Kutta condition imposed.

## 5.2 Starting Solution with No Kutta Condition

The calculation was made for a conical nose of fineness ratio 3 so that the semiapex angle is  $9.465^\circ$ . The free-stream Mach number is 3.0 and the angle of attack is  $25^\circ$ . The first problem is to start the solution since the initial conditions required are the flow field in a crossflow plane at some small value of axial distance,  $z$ . The solution is continued until the effect of the starting solution dies out. For conical flow we can test the conicity of the flow to determine when the effect of incorrect initial conditions are damped out.

Since there is no length scale in the problem, arbitrary units of axial length have been introduced and a cone of length 50 was chosen. Up to  $z \approx 10$  the mesh was laid out in increments of  $\Delta\phi$  of  $15^\circ$  with 10 radial bands of mesh quadrilaterals. At  $z \approx 10$ , the value of  $\Delta\phi$  was reduced to  $10^\circ$  with 16 radial bands of mesh quadrilaterals. At  $z \approx 20$  the increments in  $\phi$  were reduced to  $5^\circ$  with 31 radial bands of grid quadrilaterals.

In the calculated case the solution was started at small  $z$  with the  $\alpha = 0^\circ$  solution for a cone having the  $9.46^\circ$  semi-apex angle and the angle of attack was increased to  $\alpha = 25^\circ$  in 100 steps. The solution was continued downstream 846 steps to a nominal distance of  $z = 50$  in arbitrary units. Let us examine the flow field about the cone at  $z = 50$ . If we plot

particle paths\* in the crossflow plane as shown in Figure 9(a), they will not be tangent to the cone since the conical surface is expanding. If we transform from Cartesian coordinates to spherical polar coordinates, this problem disappears since the streamlines are conical as seen by an observer at the apex. Figure 9(b) shows this picture based on the flow field calculated at  $z = 50$ . It is seen that the streamlines are altogether different from the particle paths in the crossflow plane. It appears that separation occurs near the top of the body.

The occurrence of separation with the use of the Euler equations has been observed many times. It is usually attributed to artificial viscosity due to the numerics. It is, however, interesting to see how the separation angle obtained by the Euler equations with no Kutta conditions compares with experiment. The calculated separation points are shown in Figure 10 as a function of axial length along the cone. It is seen that no separation occurs until  $z > 20$ , and the separation travels down the side of the body. The solution is not valid since the separation line is not conical for the whole length of the cone as found experimentally.

It was decided to carry out the calculations to larger values of  $z$  to see if the separation would approach a conical state asymptotically. The calculations were extended to  $z = 250$  where  $\phi_{s1}$  was approximately  $150^\circ$ , but there was no firm indication that an asymptotic solution was being approached. The calculations were not calculated further because of cost. It is possible that an asymptotic separation position might have been achieved. However, there is no a priori reason to believe that the value of  $\phi_{s1}$  would agree with experiment. This is to be expected in view of the fact that the artificial viscosity in the calculation cannot be expected to be equal to that for a turbulent boundary layer. The Euler equations will not automatically yield the proper separated solution if left to their

---

\*Partical paths are solutions to the equations  $dx/dy = u/v$ .

own devices. Instead we must impose separation where we want it, and then apply the Euler equations. This procedure is essential in obtaining efficient starting solutions at high angles of attack for configurations with pointed noses.

### 5.3 Solution with Kutta Condition

The Euler equation applied to a cone will yield a conical solution if the cone is not above its shock detachment angle. If we specify conical separation boundary conditions, then the solution should still be conical since no characteristic length has been introduced into the problem. For an angle of attack of  $25^\circ$ , a Mach number of 3.0, and a cone angle of  $9.46^\circ$  we find that

$$\frac{\alpha}{\theta_n} = 2.64 \quad M_n = 1.27$$

From Figure 6 we find that

$$\phi_{s_1} = 132^\circ$$

In the calculation, we have used an increment in  $\Delta\phi$  of  $5^\circ$  and have used  $\phi_{s_1} = 130^\circ$  to put separation on a nodal point of the mesh. Let us now address the initial conditions and the separation boundary conditions.

The initial condition was taken to be the solution for calculation with no Kutta condition at  $z = 50$  where  $\phi_{s_1} = 162^\circ$ . The calculation was initialized at  $z = 0.1$  on this basis and the Kutta condition was turned on at  $z = 0.2$ . In the Kutta condition we have used the conditions that

$$\begin{aligned}\phi_a &= \theta_c \\ \phi_c &= 90^\circ\end{aligned}$$

so that Equation (3) yields

$$\begin{aligned}
 u_0 &= q_0 \sin\theta_c \sin\phi_s \\
 v_0 &= q_0 \sin\theta_c \cos\phi_s \\
 w_0 &= q_0 \cos\theta_c
 \end{aligned}
 \tag{6}$$

Letting  $\vec{i}$ ,  $\vec{j}$ , and  $\vec{k}$  be unit vectors along x, y, and z, respectively, and remembering that x,y,z is a left-handed Cartesian system, we find that the unit vector lying in the cone along the  $\phi = \phi_s$  line is

$$\vec{i}_r = \vec{i} \sin\theta_c \sin\phi_s + \vec{j} \sin\theta_c \cos\phi_s + \vec{k} \cos\theta_c
 \tag{7}$$

It is clear, therefore, that  $\vec{q}_0$  lies along the  $\vec{i}_r$  direction. With this version of the Kutta condition, the calculations were carried out on a grid with a  $\Delta\phi$  increment of  $5^\circ$  and with 31 rings in the r direction. The calculations were carried to  $z = 10$  without changing the mesh.

In Figure 11 the calculated flow field streamlines as seen by an observer at the cone apex are shown. The flow does separate at the  $\phi = 130^\circ$  lines, shown on the figure, and no secondary separation is apparent. It is of interest to show the degree of conicity of the surface pressure distribution, the bow shock, and the flow field. Also the comparison between the experimental and calculated pressure distribution will be shown. Some account of the magnitude and sources of the vorticity of the flow field is then given.

The calculated body pressure coefficients at  $z = 2, 4, 6, 8,$  and  $10$  are shown in the following table. The body pressure distribution exhibits a high degree of conicity.

$\phi$	$z = 2$	$z = 4$	$z = 6$	$z = 8$	$z = 10$
0	0.6159	0.6158	0.6158	0.6158	0.6159
30	0.4997	0.4995	0.4993	0.4992	0.4991
60	0.2451	0.2447	0.2445	0.2444	0.2443
90	0.0180	0.0183	0.0183	0.0183	0.0183
120	-0.1068	-0.1069	-0.1069	-0.1070	-0.1065
150	-0.1129	-0.1116	-0.1101	-0.1098	-0.1098
180	-0.0678	-0.0680	-0.0686	-0.0688	-0.0689

The bow waves, if conical, will exhibit constant value of  $R_s$  for a given  $\phi$  as  $z$  increases. The following values are given

$z$	$R_s$	$R_s$
	$\phi = 0$	$\phi = 180$
2	1.584	5.700
4	1.584	5.753
6	1.584	5.778
8	1.584	5.794
10	1.584	5.806

The bow wave is closely conical.

The flow field on the horizontal plane of symmetry of the body ( $\phi = 90^\circ$ ) is now exhibited.

$\phi = 90^\circ$						
R	$z = 4.0$			$z = 10$		
	U	V	W	U	V	W
1.0000	0.11133	0.37369	0.67022	0.11133	0.37371	0.67022
1.6387	0.14217	0.28260	0.67055	0.14216	0.28256	0.67056
2.2794	0.14062	0.26327	0.67224	0.14064	0.26324	0.67223

As a second sample of the flow field, consider a line,  $\phi = 130^\circ$ , through the separation point.

$\phi = 130^\circ$						
	$z = 4.0$			$z = 10$		
R	U	V	W	U	V	W
1.0000	0.10576	0.08874	0.82833	0.10575	0.08873	0.82827
1.0880	-0.10190	0.45520	0.70642	-0.10128	0.45388	0.70646
1.1760	-0.10610	0.43003	0.70588	-0.10572	0.43033	0.70571
3.6401	0.05600	0.34271	0.69840	0.05589	0.34266	0.69850

Both samples of the flow field show that it is closely conical.

It is of interest to see the calculated pressure distribution at the cone surface since it was essentially conical. The calculated distribution for the present example is shown in Figure 12 as plotted against conical polar angle. The calculated pressure distribution is smooth on the windward surface and on the leeward surface up to the separation point. Thereafter it is no longer smooth as a result of shock and expansion waves. The pressure coefficient almost approaches  $C_{p_{min}}$ , the value for a vacuum.

The pressure coefficient has been plotted versus lateral distance from the vertical plane of symmetry in Figure 13. The pressure coefficient is shown for the calculation without the Kutta condition and with the Kutta condition. Also included on the figure are the measured pressure distributions from the results of Landrum, Reference 22. It is clear that the data are in close agreement with the calculation based on the Kutta condition except at  $\phi = 180^\circ$ . The use of the Kutta condition changes the pressure distribution only on the leeward side above the separation point.

Let us now examine the circulation for several contours in the crossflow plane. The first contour is one which enclose the region between the bow wave (including the bow wave) and

the body contour as shown in Figure 14 constructed from the calculations for the case with no Kutta condition. Up to  $z = 20$  there is no separation yet a circulation is calculated. This could be associated with the starting solution. However, for  $z > 20$  the circulation parameters start to increase more rapidly as would be expected for flow with separation.

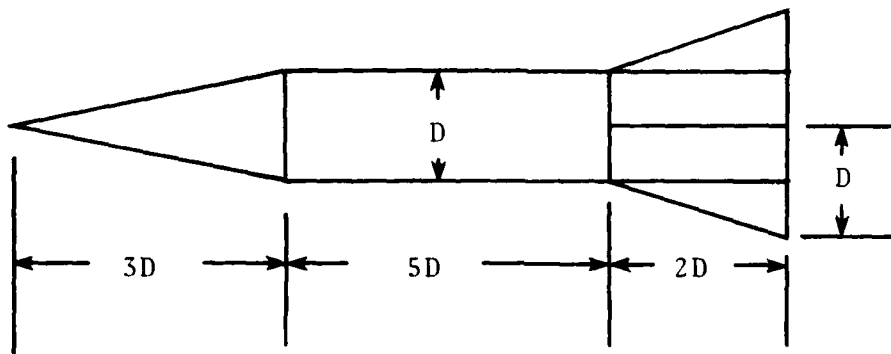
More to the point is the circulation as calculated for the case with the Kutta condition. The total circulation is shown in Figure 15 by the circles, and it increases almost linearly as would be expected for conical flow. A separate contour was used enclosing only the bow shock to determine the magnitude of the vorticity generated by it as measured by the circulation about the contour. It turns out to be quite small, about two orders of magnitude less than that due to separation, and is difficult to calculate accurately. The amount of circulation below the  $\phi = 90^\circ$  line was also calculated to see how much of the total vorticity is on the windward side. The quantity could not be accurately determined but it is about 1% to 2% of the total vorticity.

The foregoing calculation has demonstrated the method for obtaining solutions for the flow about pointed cones at angles of attack above the cone semi-apex angle but below the cone shock detachment angle. These solutions are required for starting Euler solutions for supersonic configurations with sharp noses. It is believed the separated flow solutions are accurate representations of the flow field when secondary separation does not occur or when it is not important. Further calculations are needed to determine the limitations of the method with respect to cone angle, angle of attack, and Mach number.

## 6. SAMPLE CALCULATIONS FOR WING-BODY COMBINATIONS

### 6.1 Introductory Remarks

It is our desire to do a complete pressure distribution calculation for a sample wing-body combination to illustrate the various nonlinear aerodynamic phenomena influencing the loading and to compare with experiment where possible. For this purpose we have chosen the following configuration. The



case of  $M_\infty = 3.0$  and  $\alpha = 25^\circ$  will be taken. We will compare pressure distributions and axial loading distributions on the body as measured and as predicted up to the beginning of the winged part. We will compare the fin normal force with measurements on a similar body using a fineness ratio three ogival nose rather than a conical nose. This difference should not be significant.

The solution for the conical nose in the previous section was used to start the solution. For  $z/D = 3$  to  $z/D = 7$  a mesh of 36 azimuthal points (every  $\Delta\phi = 5^\circ$ ) was used with 30 radial points. From  $z/D = 7.0$  to  $z/D = 10$  the number of radial points was increased to 50. From  $z/D = 7$  to  $z/D = 8$ , an integration interval of  $\Delta z/D = 0.004$  was used, and this interval was halved over the winged section of the combinations.

On the cone the separation parameters of the previous section were used.

$$\phi_{s_1} = 130^\circ \quad \phi_c = 90^\circ \quad \phi_a = 9.46^\circ$$

On the cylinder the following separation parameters were used.

$$\phi_{s_1} = 120^\circ \quad \phi_c = 90^\circ \quad \phi_a = 0^\circ$$

At the fin leading edge the velocity vector was taken tangent to the leading edge in fulfillment of the Kutta condition.

In the following discussions we will first discuss the pressure distributions and loading on the body up to the wing section and then discuss the results for the winged section.

## 6.2 Body Pressure Distributions and Loadings

Before discussing the pressure distributions let us look at the axial variation of the normal loading. This can be most simply considered in terms of an effective crossflow drag coefficient.

$$c_{d_c} = \frac{2 \int_0^\pi C_p r \cos\phi \, d\phi}{D \sin^2\alpha} \quad (8)$$

$r$  = local body radius

$D$  = body diameter

The appearance of  $D$  in the denominator normalized  $c_{d_c}$  to the cylindrical diameter and  $\sin^2\alpha$  put  $c_{d_c}$  on the basis of crossflow dynamic pressure. From the Euler calculation, crossflow pressure distributions at a number of axial stations have been determined and have been integrated to obtain the effective crossflow drag coefficient. The results are shown in Figure 16.

Up to  $z/D = 3$ , the flow field is conical so that  $c_{d_c}$ , which used the cylinder diameter as the reference length, increases linearly as shown. However, crossing the nose-cylinder juncture the loading falls discontinuously. On the upper meridian

( $\phi = 180^\circ$ ) and the lower meridian, the flow expands around the juncture by  $9.46^\circ$ . However, the expansion on the upper meridian starts from a much higher Mach number than that on the lower meridian, so that it does not fall so far in pressure. For instance, the average upper surface pressure coefficient is  $-0.10$  before expansion and  $-0.135$  after expansion. For the lower surface the comparable pressure coefficients are  $0.45$  and  $0.19$ . From  $z/D = 3.0$  to  $z/D = 6.0$ , there is not much change in  $c_{dC}$ , its value falling from about  $1.8$  to about  $1.55$  in three body diameters.

Pressure distributions are available at a number of body stations from Reference 22. In fact, the conical pressure distributions calculated for the conical nose have already been favorably compared with data in Figure 12. Pressure distributions as calculated and measured are compared for 5 axial stations on the cylinder in Figure 17. Examination of these comparisons shows that the pressure coefficients on the impact surface are predicted as closely as could be expected. (The data are for  $M_\infty = 2.98$  and the theory is for  $M_\infty = 3.0$ .) The theory on the upper surface indicates a shock in front of the separation and an expansion behind it, which is not borne out by the data. Switching to a finer grid at  $z/D = 7$  reduced this shock jump from about  $0.1$  at  $z/D = 6.5$  to about  $0.06$  at  $z/D = 8$ . It thus is, in part, grid dependent. Other factors are probably also responsible. However, the average pressure on the upper surface is quite well represented by the calculated pressure distribution. It follows that the local loading is closely predicted by the Euler code. The only exception is possibly at  $z/D = 3.8$  where the measured loading is about 12 percent low. This is thought to be a viscous effect associated with the sharp corner at the cone-cylinder juncture.

It has already been stated that only primary separation has been involved in the present model. The inclusion of secondary separation in the model is possible but is not warranted on the basis of the loading results. It is not clear

that the neglect of secondary separation is the reason for the pressure fluctuations on the upper surface since these seem to be mesh dependent.

### 6.3 Aerodynamics of the Finned Section of the Combination

Several interesting aspects of the aerodynamics of the finned section of the wing-body combination are shown by the Euler calculations. First, let us examine the pressure distributions acting on the combination in crossflow planes normal to the axis. These are shown in Figure 18 for fin axial location starting at  $z/D = 8.0$ , the start of the fin root chord, to  $z/D = 10$  at the fin trailing edge. At  $z/D = 8.0$  the upper surface pressure shows a crossflow shock in front of separation, the magnitude of which is mesh dependent as discussed in connection with Figure 17. However, this shock and the subsequent expansion damp out quickly over the finned section, and the upper surface pressure becomes quite uniform by the time the trailing edge is reached.

On the lower surface there is a compression where the body fairings into the fin followed by a later expansion slightly before the fin tip is reached. There is some roughness in the calculation on the curved undersurface of the wing.

Since we have included realistic body vortex effects in the present calculation, the fin normal-force coefficient as calculated should be comparable with experiment. A numerical integration of the fin pressure coefficients yields a normal-force coefficient for the fin based on fin planform area of 0.468. An experimental value of the fin normal-force coefficient from Reference 21 gives 0.457. This agreement is as good as can be expected considering experimental error and the fact that the thickness effects are not included in the Euler calculations.

Some idea of the character of the vortex field and the loading on the body due to the fin is given by the Euler

calculations. At the beginning of the finned section, the Kutta condition at the body ( $\phi_{s1} = 120^\circ$ ) is no longer carried along in the calculation. However, what happens to the body vortex in view of the persistency of vorticity is of interest. Examination of the crossflow velocity components on the body yields an approximate idea of the location of separation since the body is almost cylindrical, the effects of blending being small near the separation lines. The lateral positions of the separation point were estimated to vary with  $z/D$  as given below.

<u><math>z/D</math></u>	<u><math>x_s/D</math></u>
8.0	0.44
8.25	0.43
8.50	0.44
8.75	0.48
9.00	0.48
9.25	0.47
9.50	0.46
9.75	0.44
10.0	0.43

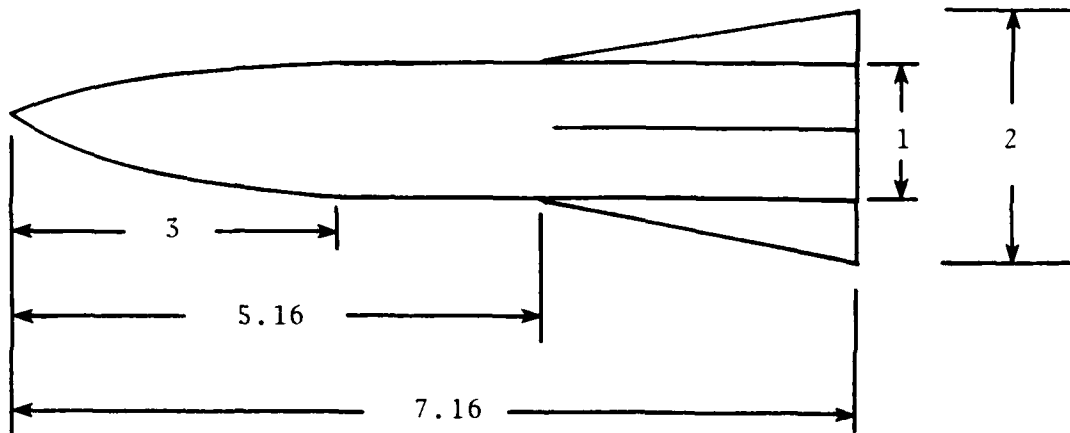
Since a value of  $x_s/D$  of 0.444 corresponds to a separation point at  $\phi_{s1} = 120^\circ$ , it is seen that the separation line varies above and below the  $\phi_{s1} = 120^\circ$  line. Within the accuracy of the determination of  $x_s/D$ , it is well approximated by a line parallel to the body centerline over the winged part of the configuration. However, the persistency of circulation has perpetuated separation without imposing the Kutta condition.

Since the body vortices persist over the fins, what can we say about the "lift carry-over" from the fin to the body? Figure 19 shows the effective crossflow drag coefficient curve of Figure 16 extended over the fin. It is noted that a linear rate of increase in  $c_{d_c}$  starts at the leading edge of the fin root chord. This rate of increase is composed of components associated with the average pressure  $\bar{C}_{p_{up}}$  on the

upper surface and the average pressure  $C_{p_\ell}$  on the lower surface. It turns out that  $\bar{C}_{p_{up}}$  does not change significantly going from the cylinder to the finned surface. (The average pressure is almost that of a vacuum.) Accordingly, the body lift on the upper surface is not changed by fin-body interference, but is the same as that in front of the fin with the body vortices present. The increase in  $c_{d_c}$  over the finned section is due mainly to an increase in  $\bar{C}_{p_\ell}$ . This effect is associated with the damming effect of the fin on the flow on the impact side of the configuration.

#### 7. EFFECTS OF ANGLE OF ATTACK AND MACH NUMBER ON LOADING OF EXAMPLE WING-BODY COMBINATION

In order to demonstrate the use of the Euler code for determining pressure distributions, it was decided to do some parametric calculations for a sample wing-body calculation varying angle of attack and Mach number. The basic configuration chosen for these calculations has the following dimensions:



The configuration has a cruciform wing and an ogival nose. At each axial station of the computation the cross section of the configuration is transformed analytically into a circle of

unit radius assuming the fins have no thickness. The boundary conditions are applied on a circle of radius  $1 + \epsilon$  where  $\epsilon = 0.025$  at the leading edge of the wing-body juncture. The value of  $\epsilon$  varies from 0 at  $z = 4.16$  to 0.025 at  $z = 5.16$ . Since the boundary conditions are applied slightly off the unit circle, the wing is faired smoothly into the body and forms a blended wing-body combination. The wing has thickness as a result.

The separation line position on the body was not varied during the calculations since a strictly parametric study was desired. The separation line was taken at  $\phi_{s1} = 120^\circ$  from  $z = 1.5$  to  $z = 5.16$ . The separation angles, defined in Figure 2, were taken to be

$$\phi_c = 30^\circ; \phi_a = 10^\circ$$

The streamline at separation was thus in a plane  $30^\circ$  from the tangent plane to the body and  $10^\circ$  from the axial direction. This prevented it from entering the body on the ogival nose. These conditions were kept constant for the following set of calculations.

$$\begin{array}{ll} M_\infty = 3 & \alpha = 15^\circ, 20^\circ, 25^\circ \\ \alpha = 20^\circ & M_\infty = 3, 4, 5 \end{array}$$

A variable grid was used in calculating the separated flow up to the leading edge of the wing-body juncture. However, over the winged part of the configuration, a constant mesh was used with  $\Delta\phi = 3^\circ$  and 51 radial rings of quadrilaterals. The integration along the wing was carried out in 1000 steps of equal axial distance (0.002).

It is of interest to examine first the effect of Mach number on the fin pressure distributions at the wing trailing edge as shown in Figure 20(a). On the impact surface the pressure is not far from the Newtonian value of  $2 \sin^2 \alpha$  and

does not vary significantly with Mach number. On the upper surface the pressure coefficient is nearly uniform and is close to that for zero pressure, a value dependent on Mach number. By using the above approximations, the fin normal force could be estimated.

At  $M_\infty = 5$ , the body upper surface pressure coefficient at the trailing edge varies from -0.042 to 0.0498 to be compared with a value of  $C_{p_{\min}}$  of -0.0574. At a Mach number of 3.0 the body upper surface pressure coefficient varies from about -0.10 to -0.12 versus a value of  $C_{p_{\min}}$  of -0.159.

Comparison of the fin pressure distributions at the fin trailing edge at  $M_\infty = 3$  for angles of attack  $15^\circ$  and  $25^\circ$  is made in Figure 20(b). The pressures on the upper surfaces are close to  $C_{p_{\min}}$ , the  $\alpha = 25^\circ$  pressures being closer than the  $\alpha = 15^\circ$  ones. On the impact surface the pressure shows considerable difference between  $\alpha = 15^\circ$  and  $\alpha = 25^\circ$  as would be expected on the basis of Newtonian impact theory.

A point of interest in connection with the foregoing calculations is how the vorticity due to the body compares in magnitude with that due to the fin leading edge. The circulation about a contour similar to that in Figure 14 is useful in illustrating these effects. The value of  $\Gamma/2\pi V_\infty a$  has been plotted versus axial distance in Figure 21(a) for  $\alpha = 15^\circ$  and  $25^\circ$  at  $M_\infty = 3.0$ . The amount of vorticity generated before the separation point on the body is negligible, but on the cylindrical section it grows approximately linearly until the winged section is reached. Over the winged part of the missile, the rate of vorticity generation is smaller at  $\alpha = 15^\circ$  than at  $\alpha = 25^\circ$  as would be expected.

A comparison of the circulation distributions for  $M_\infty = 3$  and 5 for  $\alpha = 20^\circ$  is given in Figure 21(b). Over the body up to the winged section, the circulation results show a slightly lower value for  $M_\infty = 5.0$  than for  $M_\infty = 3.0$ , but the differences are not large. Over the winged part of the body it would be

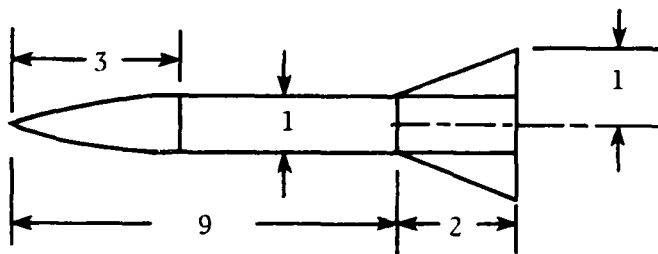
expected that less vorticity would be generated at  $M_\infty = 5$  than at  $M_\infty = 3$  since the fin normal force is somewhat less (see Fig. 20(a)).

## 8. COMPARISON OF BODY VORTEX EFFECTS PREDICTED BY EULER EQUATIONS AND A PANEL METHOD

### 8.1 Introductory Remarks

It is possible to obtain the fin and body pressure distributions with or without body vortices present using either the Euler equations or a supersonic panel method such as that given in Reference 2. The panel method is basically a linear method for the velocity flow field, even though it uses the nonlinear Bernoulli equation for the pressure field. We have chosen as the example the following wing-body combination at  $\alpha = 10^\circ$  and  $M_\infty = 3.0$ . The comparison between the Euler method and the panel method will thus be in the possible range of applicability of the panel method.

The wing-body combination has a fineness ratio 3 ogival nose followed by a cylindrical section 6 body diameters long up to the winged section. The  $AR = 1$  delta fin has a root chord of 2 diameters and an exposed semispan of 0.5 diameter.



For the purpose of comparing body loadings the same body vortex model is used for both the Euler and panel methods. It

was assumed that separation occurred from  $z/D = 3$  to  $z/D = 9$  along the  $\phi_{s1} = 90^\circ$  line. The angular parameters at separation were

$$\phi_a = 10^\circ$$

$$\phi_c = 30^\circ$$

for the entire cylindrical length.

In the panel method the vortex downwash distribution across the wing panels is determined from external and image line vortices using the Biot-Savart law, thereby neglecting compressibility. First we will compare the vortex induced downwash as calculated by the Euler equation and then the Biot-Savart law. Next we will determine the fin loading distributions due to the Euler downwash distribution using both the Euler and panel methods. It is noted that the loading distribution calculated for the Euler equations is for a fin with thickness and that using the panel method is for a fin without thickness.

## 8.2 Comparison of Downwash Distributions

We will compare the downwash distributions resulting from the vortical flow field at  $x/D = 9$  calculated by the panel code and by the Euler code with the above separation model. The downwash due to the body vortices in the plane of the wing calculated by the Euler equations was determined by subtracting the downwash calculated with no Kutta condition from that with the Kutta condition. This procedure eliminates the downwash that occurs without body vortices. The body vortex downwash in the plane of the wing as used in the panel method is determined by considering the body vortex strengths and positions in the cross-flow plane, putting the appropriate images inside the body, and calculating the induced velocities by the Biot-Savart law. In the present calculation there are 60 mesh quadrilaterals in the  $\phi$  direction and 49 in the radial direction. The vorticity in each quadrilateral was determined from the Euler solution by

calculating the circulation around its boundary, and a point vortex was placed at its centroid. The downwash on the horizontal plane was then determined by considering all external and image vortices on each side of the combination, calculating their induced downwash, and summing over all the vortices.

The calculated results are shown in Figure 22 for both the Euler method and the Biot-Savart method. The induced flow is downward over the entire fin span. The two results are fairly close although the Euler solution yields on the average more downwash than the Biot-Savart method. Since the Biot-Savart method neglects compressibility, some difference is to be expected.

### 8.3 Comparison of Loading Distributions

In order to make a meaningful comparison of the loading distributions calculated by the Euler equations and the panel method, it was decided to use the same downwash distribution at  $z/D = 9.0$  for both. The loading is defined to be the lower surface pressure coefficient minus the upper surface pressure coefficient at the same position on the planform. By comparing loadings we minimize any effects due to thickness accounted for in the Euler approach but not in the panel method since to the second order in  $\alpha$ , thickness has no effect on the normal-force coefficient for supersonic airfoils.

The comparisons are presented in Figure 23. In Figure 23(a) the Euler pressure distributions in the upper and lower surfaces are presented with and without the Kutta condition. It is noted that the effects of body vortices are larger on the upper surface. However, near  $x/D = 0.5$  on the lower surface, the position of the shock is changed in a way which is probably a function of the algorithm sensitivity. In Figure 23(b) the loading as determined from the pressure distributions in Figure 23(a) is shown. The loading at the wing-body juncture from the Euler solution may be spurious because of the

change in the shock location noted above. Also in Figure 23(b) the loading as computed by the panel method is compared with that due to the Euler code. There are differences, but the average load is about the same.

The panel method utilized as a downwash boundary condition on the fins of zero thickness the difference in downwash between the Euler code with and without the Kutta condition. As a matter of interest the vorticity axial distribution for the body alone up to  $z/D = 9.0$  with and without the Kutta condition is shown in Figure 24(a). The nonzero values of  $\Gamma/2\pi V_\infty a$  for the body without the Kutta condition are not due to body flow separation since no separation due to numerical viscosity occurred before  $z/D = 9.0$ . The downwash in of the fin due to the vorticity distribution without the Kutta condition causes very small downwash angles relative to those with the Kutta condition. The panel calculations were made with 10 panels chordwise and 10 rows of panels spanwise.

There are a number of reasons why the panel method is only approximate. First the loading calculations were made at  $\alpha = 0$  using the fin boundary conditions described above. We could have calculated the loading at  $\alpha = 10^\circ$  with and without body vortices and subtracted the differences. The results would be different from those in Figure 23 if the full nonlinear Bernoulli equations were used. However, it should be noted that the results of Figure 23 were calculated with the nonlinear Bernoulli equation including the effects of a strong sidewash due to the vorticity distribution. Without including this sidewash effect the agreement is not nearly so good.

In the second place there are thickness effects included in the Euler results but neglected in the panel results. However, by using loadings rather than pressure coefficients this effect is minimized. Thirdly, the panel method assumes that the downwash distribution at  $z/D = 9$  is the same for all  $z/D$  values over the wing. Both of these latter effects could be treated by the panel method.

This example, taken at the edge of the range of applicability of panel theory, shows that the method for handling vortex effects in that theory is basically sound for gross forces. However, several nonlinear effects which reduce the accuracy of panel theory have been noted.

## 9. CONCLUDING REMARKS

The primary purpose of this report has been to demonstrate the applicability of the Euler equations to the calculation of flow about supersonic wing-body combinations at high angles of attack for cases where significant effects of compressibility and flow separation are both present. The treatment of separated flows by the Euler equations requires a knowledge of the positions of the separation lines. Special boundary conditions are used on these lines to make the Euler solution unique. It was found that methods such as those of Stratford for predicting the separation line location are not valid at high crossflow Mach numbers since separation does not necessarily occur in a rising pressure field. It was thus necessary to rely principally on empirical correlation for separation line positions.

Since most high-speed missiles (and airplanes) have sharp noses which can be fitted by a cone and since the flow separates over cones at angles of attack in excess of the cone half angle, it is necessary to have solutions for cones with separation to start the Euler solutions at high angles of attack. Accordingly, the separation data on cones, which exhibit conical separation, were correlated so that the primary separation line locations could be estimated. At the same time primary separation angles for two-dimensional circular cylinders and circular cylinders at angles of attack were correlated for application to the cylindrical section of wing-body combinations.

The Euler equations were applied to a cone at an angle of attack well above its semiapex angle for which separation is to be expected. Without applying the separation boundary condition, the solution finally exhibits nonconical separation as a result of artificial viscosity. Such a solution does not agree with experiment. By imposing a conical separation boundary condition, the Euler equations developed a conical separation flow for which the pressure distribution was in good agreement with experiment. This solution demonstrated how to develop a proper starting solution for a wing-body combination when the nose is pointed and separation starts at the nose. Cone tables for angles of attack greater than the cone semi-apex angle can be developed by this technique.

Having demonstrated how to start the solution for bodies or wing-bodies when separation starts at the nose, we carried out a series of calculations to demonstrate the feasibility of using the Euler equations to determine the flow field of wing-body combinations with both body vortices and leading-edge vortices present. A range of Mach numbers up to 5 and a range of angles of attack up to  $25^\circ$  were covered with results which were in good agreement with available data. No attempt to determine the limits on the method with regard to angle of attack was carried out. However, it is felt that the method in its present form should work up to the angle of shock detachment for the nose.

Since the Euler equations treat the combined effects of compressibility and vortices on a true nonlinear basis, it was decided to apply them to a case for comparison with a supersonic panel method (DEMON2) which linearly superposes these effects. A case at  $M_\infty = 3.0$  and  $\alpha = 10^\circ$  was chosen which is near the limits of applicability of linear panel methods. It was found that the Euler equations predicted somewhat more downwash on the horizontal fins than did the Biot-Savart law used in the panel method. For the same downwash distribution on the fins, both methods predicted about the same normal-force increment

due to the body vortices, but the shapes of the loading distributions differed. Further comparisons are needed between panel and Euler methods to determine the accuracy and shortcomings of panel methods for estimating the effects of vortices on pressure distributions.

While the present work has demonstrated the applicability of the Euler equations to supersonic wing-body combinations with significant compressibility and vorticity effects, it has not addressed certain additional problems which arise for wing-body-tail combinations. One of these problems is the rolling-up of the fin wakes between the wing and tail, and the subsequent effect on the tail panels. Another effect, known to be important at high angles in certain cases, is the vortex wake developed by the afterbody between the wing and tail particularly as influenced by the presence of the wing vortices. These questions are susceptible to solution by Euler methods, but the technology remains to be demonstrated.

## REFERENCES

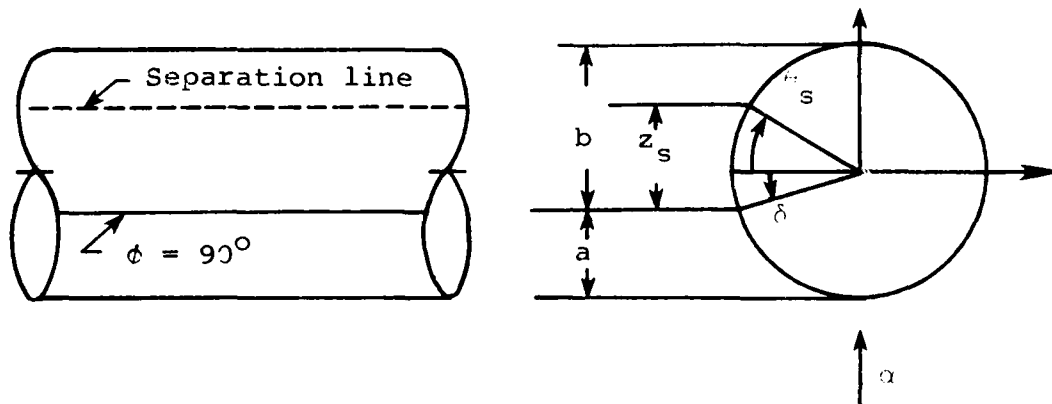
1. Klopfer, G. H. and Nielsen, J. N.: Basic Studies of Wing-Body Interference at High Angles of Attack and Supersonic Speeds. Report ONR-CR215-263-1, Oct. 1979.
2. Dillenius, M. F. E. and Nielsen, J. N.: Computer Program for Calculating Pressure Distributions Including Vortex Effects on Supersonic Monoplane or Cruciform Wing-Body-Tail Combinations With Round or Elliptical Bodies. NASA CR 3122, Apr. 1979.
3. Wardlaw, A. B., Jr., Solomon, J. M., and Baltakis, F. P.: Supersonic Inviscid Flowfield Computations of Missile Type Bodies. AIAA Paper No. 80-0271, presented at AIAA 18th Aerospace Sciences Meeting, Pasadena, CA, Jan. 1980.
4. Klopfer, G. H. and Nielsen, J. N.: Basic Studies of Body Vortices at High Angles of Attack and Supersonic Speeds. Nielsen Engineering & Research, Inc. TR 226, Oct. 1980.
5. Oberkampf, W. L. and Bartel, T. J.: Supersonic Flow Measurements in the Body Vortex Wake of an Ogive Nose Cylinder. AFATL-TR-78-127, Nov. 1978.
6. Abbett, M. J.: Boundary Condition Computational Procedures for Inviscid Supersonic Steady Flow Field Calculations. Aerotherm Corp, Mtn. View, CA, Final Report No. 71-41, 1971 (also NASA CR 114446).
7. Chaussee, D. S., Kutler, P., and Pulliam, T. H.: Three Dimensional Viscous Flow Field Program - Part 1: Viscous Blunt Body Program. Flow Simulations, Inc. Report 80-08, Oct. 1980.
8. Achenbach, E.: Distribution of Local Pressure and Skin Friction Around a Circular Cylinder in Cross-Flow up to  $Re = 5 \times 10^6$ . J. of Fluid Mech., Vol. 34, Pt. 4, 1968, pp. 625-639.
9. Murthy, V. S. and Rose, W. C.: Form Drag, Skin Friction, and Vortex Shedding Frequencies for Subsonic and Transonic Crossflow on Circular Cylinders. AIAA Paper No. 77-687, presented at AIAA 10th Fluid and Plasmadynamics Conf., Albuquerque, NM, June 1977.
10. Stratford, B. S.: The Prediction of Separation of the Turbulent Boundary Layer. J. of Fluid Mech., Vol. 5, Pt. 1, Jan. 1959, pp. 1-16.

11. Hafez, M., South, J., and Murman, E.: Artificial Compressibility Methods for Numerical Solutions of Transonic Full Potential Equation. AIAA Journ., Vol. 17, No. 8, Aug. 1979, pp. 838-844.
12. Peake, D. J. and Tobak, M.: Three-Dimensional Interactions and Vortical Flows with Emphasis on High Speeds. AGARDOGRAPH No. 252, July 1980.
13. Rainbird, W. J.: The External Flow Field About Yawed Circular Cones. Paper No. 19 in Hypersonic Boundary Layers and Flow Fields, Agard Conf. Proc. No. 30, May 1968.
14. Rainbird, W. J.: Turbulent Boundary-Layer Growth and Separation on a Yawed Cone. AIAA Jour., Vol. 6, No. 12, Dec. 1968, pp. 2410-2416.
15. Nebbeling, C. and Bannink, W. J.: Experimental Investigation of the Supersonic Flow About a Slender Cone at High Incidences. Report LR-233, Delft Univ. of Tech., Nov. 1976.
16. McElderry, E. D., Jr.: An Experimental Study of Sharp and Blunt 6 Degree Cones at Large Incidence with a Turbulent Boundary Layer at Mach 6. AFFDL-TM-74-170, Sept. 1974.
17. Peake, D. J., Fisher, D. F., and McRae, D. S.: Flight Experiments With a Slender Cone at Angle of Attack. AIAA Paper No. 81-0337, presented at AIAA 19th Aerospace Sciences Meeting, St. Louis, MO, Jan. 1981.
18. Feldhuhn, R. H. and Pasiuk, L.: An Experimental Investigation of the Aerodynamic Characteristics of Slender Hypersonic Vehicles at High Angles of Attack. U.S. Naval Ordnance Lab., NOLTR 68-52, May 1968.
19. Jones, R. T.: Effects of Sweep-Back on Boundary Layer and Separation. NACA Rept. 884, 1947.
20. Landrum, E. J. and Babb, C. D.: Wind-Tunnel Force and Flow-Visualization Data at Mach Numbers from 1.6 to 4.63 for a Series of Bodies of Revolution at Angles of Attack from  $-4^{\circ}$  to  $60^{\circ}$ . NASA Tech. Memorandum 78813, Mar. 1979.
21. Nielsen, J. N., Hensch, M. J., and Smith, C. A.: A Preliminary Method for Calculating the Aerodynamic Characteristics of Cruciform Missiles to High Angles of Attack Including Effects of Roll Angle and Control Deflection. Report ONR-CR215-225-4F, Nov. 1977.
22. Landrum, E. J.: Wind-Tunnel Pressure Data at Mach Numbers 1.6 to 4.63 for a Series of Bodies of Revolution at Angles of Attack From  $-4^{\circ}$  to  $60^{\circ}$ . NASA TM X-3558, Oct. 1977.

## APPENDIX A

### METHOD FOR SCALING SEPARATION LINE LOCATION FROM OIL-FLOW PHOTOGRAPHS

Oil flow pictures are presented in Reference 20 for a cone-cylinder at Mach numbers of 1.6, 2.3, 2.96, and 4.63 at angles of attack of  $12^\circ$ ,  $20^\circ$ ,  $28^\circ$ ,  $36^\circ$ ,  $44^\circ$ ,  $52^\circ$ , and  $60^\circ$  for most of the Mach numbers. Photographs of the oil flow patterns were taken from the side and above the body so that the near side edge of the body ( $\phi = 90^\circ$ ) appears closer to the bottom of the body than to the top of the body. The approximate side view, as seen by the camera, and an end projection are shown below.



The  $\phi = 90^\circ$  line measured from the bottom of the body is shown by an index mark on each photograph. It is possible to scale the distances  $a$ ,  $b$ , and  $z_s$  from the photographs with a divider. The values of  $a$  and  $b$  depend for their accuracy on the edge contrast in the photograph.

From these scaled values in arbitrary units of length, it is possible to determine  $\phi_{s1}$ , the primary separation location, given by

$$\phi_{s1} = 90^\circ + \delta + \theta_s \quad (A-1)$$

With the body radius given as

$$r = \frac{a + b}{2} \quad (A-2)$$

we find that

$$\sin \delta = \frac{b - a}{b + a} \quad (A-2)$$

$$\sin \theta_s = \frac{z_s}{r} - \sin \delta \quad (A-3)$$

This gives all the information necessary to get  $\phi_{s1}$  from Equation (A-1).

The photographs of the oil flow patterns have been read for flow distances along the body:  $x/\ell = 0.325, 0.475, 0.675,$  and  $0.925$ . The first station is on the cone and the last three are on the cylindrical part of the body. The scaled values of  $a, b,$  and  $z_s$  are given in Table 2 together with the position of the line of primary separation. In one instance the photograph was not sufficiently distinct to locate the separation line. The units of  $a, b,$  and  $z_s$  are arbitrary since the angles depend only on length ratios.

## LIST OF SYMBOLS

$a$	body radius
$AR$	aspect ratio of wing formed by joining two opposing fins together along their root chords
$c_{d_c}$	crossflow drag coefficient, $(C_{p_\ell} - \bar{C}_{p_{up}})/q_n$
$C_p$	pressure coefficient, $(p - p_\infty)/q_\infty$
$\bar{C}_{p_{up}}$	average pressure coefficient on top of body
$\bar{C}_{p_\ell}$	average pressure coefficient on bottom of body
$C_{p_{min}}$	pressure coefficient for $p = 0$
$\Delta C_p$	$C_{p_\ell} - C_{p_{up}}$
$D$	body diameter of cylindrical section
$k$	$2\gamma/(\gamma-1)$
$L$	length of cone-cylinder body
$M_n$	$M_\infty \sin \alpha$ , normal Mach number
$M_\infty$	free-stream Mach number
$p$	local static pressure
$p_\infty$	free-stream static pressure
$P$	$p/q_n$
$q_n$	$q_\infty \sin^2 \alpha$
$q_\infty$	free-stream dynamic pressure
$q_o$	velocity of fluid at a separation line; see Figure 2
$r$	radial coordinate in transformed plane; see Figure 1
$r_b$	value of $r$ at body surface
$r_s$	value of $r$ at bow wave
$Re_D$	cylinder Reynolds number based on diameter

R	$r/r_b$
$R_s$	value of R at bow shock
s	semispan of fin measured from body axis
u,v,w	components of local velocity along x, y, and z, respectively
$u_0, v_0, w_0$	u, v, and w components of $q_0$
x,y,z	Cartesian coordinates of physical space; see Figure 1
$x_s$	x coordinate of separation line on body
z,r, $\phi$	cylindrical coordinates of transformed space; see Figure 1
Z	$re^{i(\phi - \pi/2)}$
$\alpha$	angle of attack
$\gamma$	ratio of specific heats
$\Gamma$	circulation about a contour in a half-plane composed of the body surface and a contour containing the bow wave; see Figure 14
$\Gamma_{\text{shock}}$	circulation about a contour containing the shock in the right half-plane
$\theta_c$	semiapex angle of cone
$\lambda$	fin taper ratio
$\phi$	polar angle in cylindrical coordinates; see Figure 1
$\phi_{s1}$	polar angle of primary separation on cone or cylinder
$\phi_{s2}$	polar angle of secondary separation
$\phi_a$	angle between $q_0$ and $w_0$ ; see Figure 2
$\phi_c$	angle between plane of separation and tangent to cylinder at separation; see Figure 2

TABLE 1. PRIMARY AND SECONDARY SEPARATION LINE LOCATIONS  
FOR CONES AT INCIDENCE

Ref.	$\theta_c$	$M_\infty$	$R_{L_\infty}$	$\alpha/\theta_c$	$\phi_{s1}$	$M_n$	$\alpha$	$\phi_{s2}$
13	12.5°	1.8	$2.5 \times 10^7$	0.8	175°	.312	10°	
				1.0	169°	.388	12.5°	
				1.11	164°	.432	13.9°	
				1.24	158°	.482	15.5°	
				1.36	153°	.527	17.0°	
				1.49	146°	.575	18.6°	
				1.66	139°	.650	20.8°	
				1.70	133°	.655	21.3°	
				1.75	124°	.671	21.9°	
				1.80	122°	.688	22.5°	
				1.93	120°	.734	24.1°	
				2.00	120°	.761	25.0°	
				2.10	121°	.794	26.2°	
2.24	121°	.830	27.5°					
2.34	122°	.878	29.2°					
13	12.5°	4.25	$5.1 \times 10^7$	1.24	155°	1.14	15.5°	
				1.24	153°	1.14	15.5°	
				1.66	146°	1.51	20.8°	
				2.07	142°	1.85	25.8°	
2.33	139°	2.07	29.1°					
13	5°	1.8	$3.4 \times 10^7$	1.00	168°	.157	5°	
				2.09	139°	.328	10.5°	
				2.50	133°	.390	12.5°	
13	5°	4.25	$6.8 \times 10^7$	1.00	167°	.37	5°	
				2.09	123°	.775	10°	
2.50	122°	.922	12.5°					

TABLE 1. CONCLUDED.

Ref.	$\theta_c$	$M_\infty$	$R_{L_\infty}$	$\alpha/\theta_c$	$\phi_{s1}$	$M_n$	$\alpha$	$\phi_{s2}$
15	7.5°	2.94	$7.5 \times 10^6$	1.33	157°	.513	10°	161°
◇				1.60	140°	.615	12°	161°
				1.865	126°	.716	14°	158°
				2.13	118°-126°	.815	16°	160°
				2.40	119°	.913	18°	160°
				2.67	119°	1.013	20°	163°
				2.94	120°	1.11	22°	166°
				3.20	120°	1.203	24°	166°
				3.47	125°	1.30	28°	164°
16	6°	6.00	$1.3 \times 10^7$	1.5	136°-146°	.938	9°	162°-172°
△				2.0	128°-132°	1.25	12°	164°-170°
17	5°	0.6	$1.34 \times 10^7$	2.2	149°	.115	11°	165°
		1.5	$1.49 \times 10^7$	2.2	142°	.286	11°	157°
		1.8	$1.6 \times 10^7$	2.2	141°	.343	11°	158°
□		0.6	$1.11 \times 10^7$	2.2	148°	.115	11°	158°
		1.5	$1.08 \times 10^7$	2.2	143°	.286	11°	158°
		1.8	$9.65 \times 10^6$	2.2	143°	.343	11°	157°
18	5°	5.93	$2.7 \times 10^6$	2	123°-128°	1.03	10°	167°-170°
△				3	126°-135°	1.54	15°	165°-175°
				4	129°-142°	2.03	20°	165°-175°
				5	136°-142°	2.97	30°	
				8	129°-139°	3.82	40°	

TABLE 2. CONE-CYLINDER SEPARATION POINTS

$M_{\infty} = 1.6$

$\alpha$	$x/l$	$a$	$b$	$Z_{22}$	$Z_s$	$r$	$\frac{Z_{22}}{r}$	$\frac{b-a}{b+a}$	$\delta$	$\frac{z-s}{r}$	$e \sin \theta_s$	$\theta_s$	$\phi_{s1}$
20°	.925	67	90	35	-17	78.5	.407	.147	8.5°	-.216	-.363	-21.2°	77.3°
	.675	65	90	32	25	77.5	.413	.161	9.2°	.322	.161	9.2°	108.4°
	.475	64	89	32	31	76.5	.418	.1635	9.4°	.405	.241	13.9°	113.3°
	.325	43	53	32	26	48.0	.667	.1104	5.9°	.543	.439	26.0°	121.9°
28°	.925	70	95	34	-10	82.5	.412	.151	8.7°	-.121	-.272	-15.8°	82.9°
	.675	67	90	30	15	78.5	.381	.1465	11.1°	.191	.045	12.6°	103.7°
	.475	67	90	32	30	78.5	.408	.1465	11.1°	.382	.236	13.7°	114.8°
	.325	47	65	36	20	56.0	.655	.1605	9.2°	.357	.196	11.3°	110.5°
36°	.925	80	75	30	0	77.5	.387	-.0322	-1.9°	0	.0322	1.9°	90°
	.675	76	76	32	22	76.0	.420	0	0	.289	.289	16.8°	106.8°
	.475	78	76	32	30	77.0	.415	-.0130	.7°	.395	.408	24.2°	114.9°
	.325	58	59	33	22	58.5	.565	.0086	.5°	.376	.367	21.6°	112.1°
44°	.925	68	85	33	18	76.5	.431	.1112	6.4°	.236	.125	7.2°	103.6°
	.675	70	87	30	20	78.5	.384	.1083	6.2°	.255	.147	8.5°	104.7°
	.475	70	87	31	21	78.5	.395	.1083	5.2°	.268	.160	9.2°	105.4°
	.325	50	60	32	20	55	.582	.091	5.2°	.364	.273	5.2°	111°

TABLE 2. CONTINUED

$M_0 = 2.3$

$\alpha$	$x/l$	$a$	$b$	$Z_{22}$	$Z_s$	$r$	$\frac{Z_{22}}{r}$	$\frac{b-a}{b+a}$	$\delta$	$\frac{Z_s}{r}$	$\sin \theta_s$	$\theta_s$	$\phi_{s1}$
20°	.925	79	85	31	0	82	.376	.0366	2.1°	0	-.0366	-2.1°	92.1°
	.675	79	85	31	10	82	.376	.0366	2.1°	.123	.086	4.9°	96.9°
	.475	79	85	31	26	82	.376	.0366	2.1°	.317	.280	16.2°	108.3°
	.325	50	63	32	21	56.5	.567	.115	6.6°	.362	.247	14.3°	110.9°
28°	.925	59	95	30	8	77	.390	.234	13.5°	.104	-.130	-7.5°	96.°
	.675	59	95	30	18	77	.390	.234	13.5°	.234	0	0	103.5°
	.475	59	95	30	35	77	.390	.234	13.5°	.455	.221	12.8°	116.3°
	.325	37	70	32	31	53.5	.597	.307	17.9°	.591	.284	16.5°	124.4°
36°	.925	68	72	31	31	70	.442	.029	1.7°	.444	.415	24.5°	116.2°
	.675	68	80	31	22	74	.418	.081	4.6°	.297	.216	12.4°	107.°
	.475	70	80	31	25	75	.413	.067	3.8°	.333	.266	15.5°	109.3°
	.325	50	50	33	21	50	.660	0	0	.420	.420	24.8°	114.8°
44°	.925	76	68	31	20	72	.431	-.0352	-2.0°	.278	.313	18.3°	106.3°
	.675	76	73	31	38	74 1/2	.416	-.0201	-1.2°	.510	.530	32.0°	120.8°
	.475	76	74	31	39	75	.414	-.0133	-0.8°	.511	.524	31.5°	120.7°
	.325	52	55	30	30	53 1/2	.562	.028	1.6°	.561	.533	32.2°	123.8°
52°	.925	73	81	33	14	77	.428	.052	3.0°	.182	.130	7.4°	100.4°
	.675	72	83	33	13	77 1/2	.425	.071	4.1°	.168	.097	5.1°	99.7°
	.475	72	83	33	33	77 1/2	.425	.071	4.1°	.427	.356	21.0°	115.0°
	.325	55	59	30	26	57	.528	.070	4.0°	.456	.386	22.7°	116.7°
60°	.925	68	70	32	20	69	.464	.0145	0.8°	.290	.275	16.0°	106.8°
	.675	74	75	31	21	74.5	.416	.0067	0.4°	.282	.275	16.0°	106.4°
	.475	73	72	31	30	72.5	.428	-.0069	-0.4°	.414	.421	24.9°	114.5°
	.325	50	50	32	30	50	.640	0	0	.600	.600	36.9°	126.9°

TABLE 2. CONTINUED

$M_{\infty} = 2.96$

$\alpha$	$x/l$	$a$	$b$	$Z_{22}$	$Z_s$	$r$	$\frac{Z_{22}}{r}$	$\frac{b-a}{b+a}$	$\delta$	$\frac{Z_a}{r}$	$\sin \theta_s$	$\theta_s$	$\phi_{s1}$
20°	.925	65	103	35	19	84	.417	.226	13.1°	.226	0	0	103.1°
	.675	65	103	35	34	84	.417	.226	13.1°	.405	.179	10.3°	113.4°
	.475	65	103	35	51	84	.417	.226	13.1°	.608	.382	22.5°	125.6°
28°	.325	52	75	35	40	58 1/2	.598	.272	15.8°	.683	.411	24.3°	130.1°
	.925	60	89	31	19	74.5	.416	.194	11.2°	.255	.061	3.5°	104.7°
	.675	60	95	31	25	77.5	.399	.161	9.5°	.323	.162	9.3°	108.8°
36°	.475	60	95	31	42	77.5	.399	.161	9.5°	.541	.381	22.4°	121.9°
	.325	41	65	30	30	53	.565	.226	13.0°	.566	.340	19.9°	122.9°
	.925	65	83	30	28	74	.405	.1215	7.0°	.378	.257	14.8°	111.8°
44°	.675	65	83	30	41	74	.405	.1215	7.0°	.554	.433	25.7°	122.7°
	.475	65	83	30	58	74	.405	.1215	7.0°	.783	.662	41.5°	138.5°
	.325	50	65	30	40	57.5	.523	.1305	7.5°	.695	.564	34.3°	131.8°
52°	.925	72	80	33	13	76	.433	.0527	3.0°	.171	.118	6.8°	99.8°
	.675	72	80	33	15	76	.433	.0527	3.0°	.1975	.144	8.3°	101.3°
	.475	72	80	33	30	76	.433	.0527	3.0°	.395	.342	20.0°	113.0°
60°	.325	51	57	30	31	54	.574	.0555	3.2°	.574	.519	31.2°	124.4°
	.925	80	70	32	20	75	.426	-.0667	-3.8°	.267	.333	19.5°	105.7°
	.675	80	70	32	20	75	.426	-.0667	-3.8°	.267	.333	19.5°	105.7°
60°	.475	80	70	32	25	75	.426	-.0667	-3.8°	.333	.400	23.6°	109.8°
	.325	55	50	30	27	52.5	.515	-.0953	-5.5°	.515	.610	37.6°	122.1°

TABLE 2. CONCLUDED.

$M_{\infty} = 4.63$

$\alpha$	$x/l$	$a$	$b$	$z_{22}$	$Z_s$	$r$	$\frac{Z_{22}}{r}$	$\frac{b-a}{b+a}$	$\delta$	$\frac{Z_s}{r}$	$\sin \theta_s$	$\theta_s$	$\phi_{s1}$
20°	.925	65	70	32	34	67.5	.473	.037	2.2°	.503	.466	27.8°	120.0°
	.675	69	75	32	44	72	.445	.0418	2.4°	.612	.570	34.7°	127.1°
	.475	69	73	32	52	71	.451	.0281	1.1°	.731	.703	45.6°	136.6°
28°	.325	45	53	30	41	49	.617	.0815	4.7°	.838	.757	49.3°	144.0°
	.925	65	85	31	31	75	.413	.1333	7.7°	.413	.280	16.3°	114.0°
	.675	65	85	31	40	75	.413	.1333	7.7°	.533	.400	23.7°	121.4°
36°	.475	65	85	31	53	75	.413	.1333	7.7°	.707	.574	35.0°	132.7°
	.325	52	60	31	38	56	.554	.143	8.2°	.678	.535	32.4°	130.6°
	.925	71	80	32	27	75.5	.423	.0595	3.4°	.358	.299	17.4°	110.8°
44°	.675	71	80	32	33	75.5	.423	.0595	3.4°	.437	.378	22.2°	115.6°
	.475	71	80	32	50	75.5	.432	.0595	3.4°	.663	.604	37.1°	130.5°
	.325	50	57.5	32	37	53.7	.595	.0698	4.0°	.689	.619	38.2°	132.2°
52°	.975	80	71	30	28	75.5	.397	-.0596	-3.4°	.371	.431	25.5°	112.1°
	.675	80	71	30	32	75.5	.397	-.0596	-3.4°	.424	.484	28.9°	115.4°
	.475	80	71	30	45	75.5	.397	-.0596	-3.4°	.596	.656	41.0°	127.6°
60°	.325	52	50	30	37	51	.588	-.0196	-1.3°	.725	.745	48.0°	136.7°
	.925	61	78	30	17	69.5	.432	-.1234	-7.1°	.244	.367	21.5°	104.5°
	.675	61	79	30	14	69.5	.432	-.1234	-7.1°	.201	.385	22.6°	105.5°
60°	.475	61	79	30	30	69.5	.432	-.1234	-7.1°	.432	.355	33.8°	116.7°
	.325	42	56	30	33	49	.613	-.1429	-8.2°	.675	.798	52.9°	134.7°
	.925	67	67	29	22	67	.432	0	0	.328	.328	19.2°	109.2°
60°	.675	67	67	29	20	67	.432	0	0	.299	.299	17.4°	107.4°
	.475	67	67	29	25	67	.432	0	0	.373	.373	21.9°	111.9°
	.325	50	48	30	25	49	.613	-.0204	-1.2°	.510	.531	32.0°	120.8°

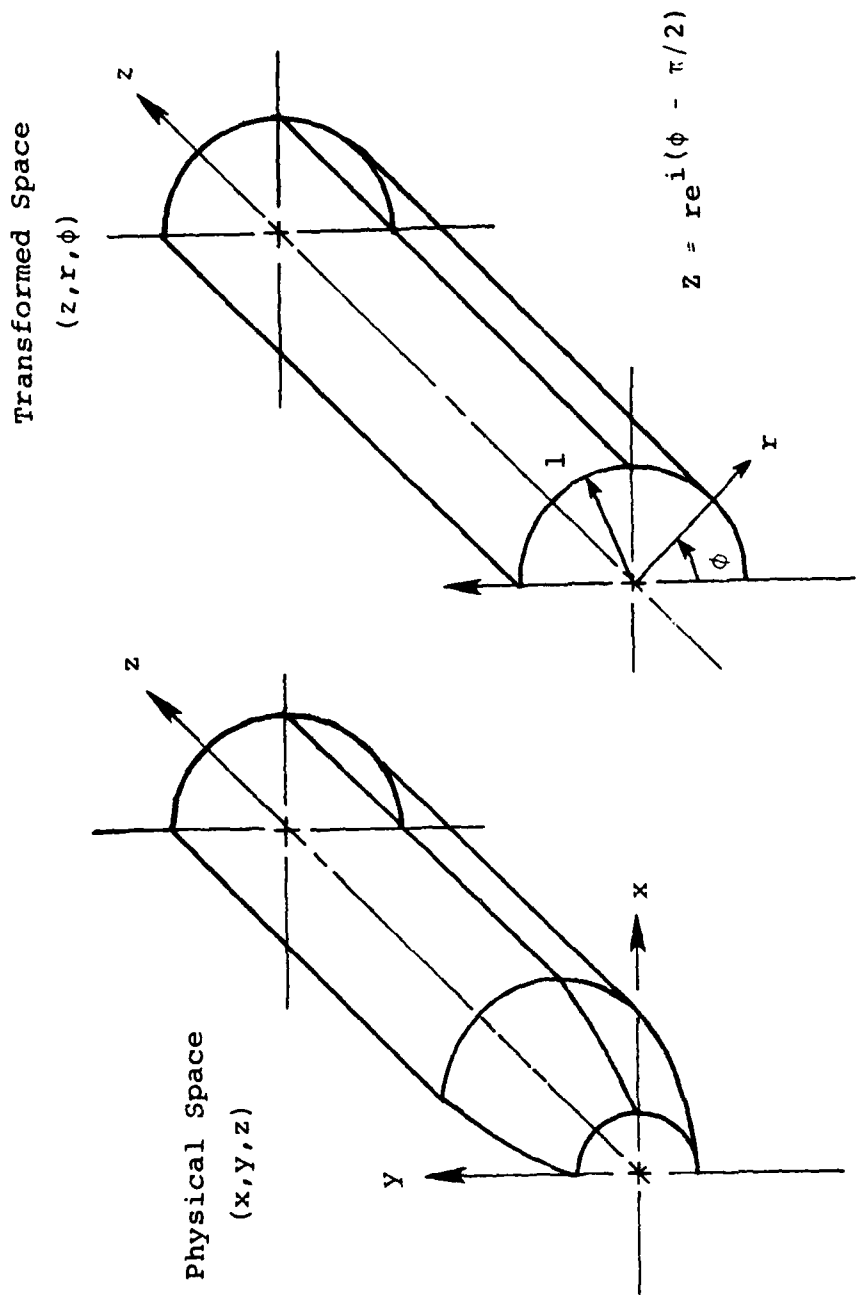


Figure 1.- The transformation between the physical space and the transformed curvilinear space.

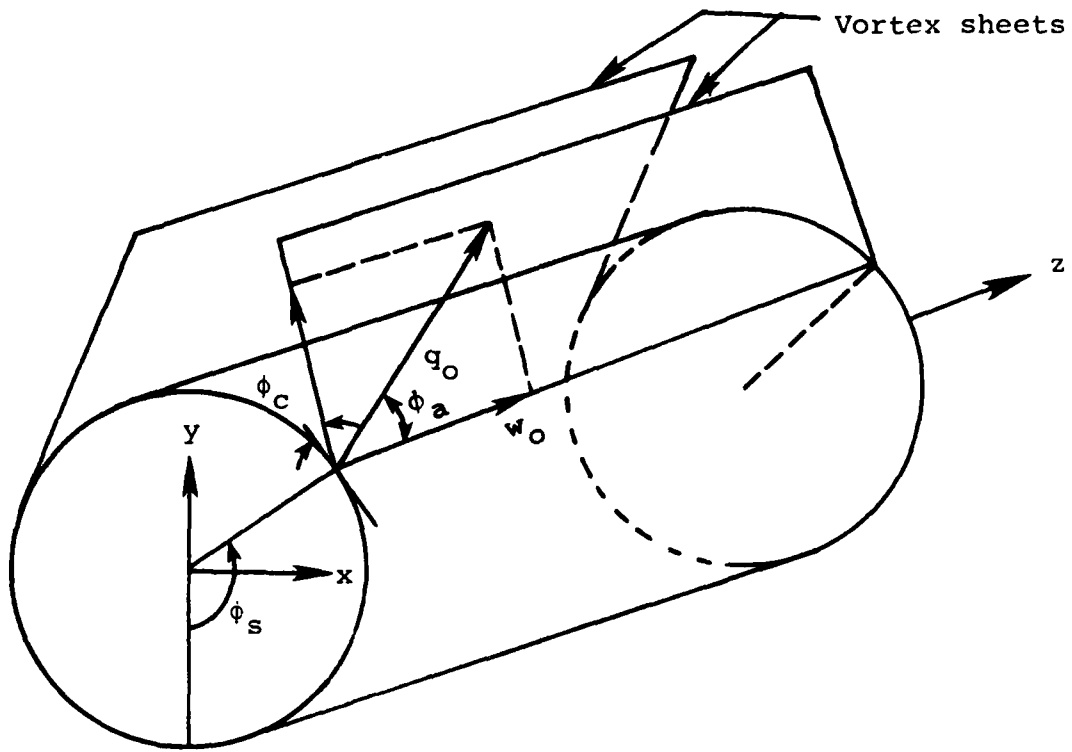


Figure 2.- Velocity components and angles of the vortex sheet defining the parameters for the Kutta condition.

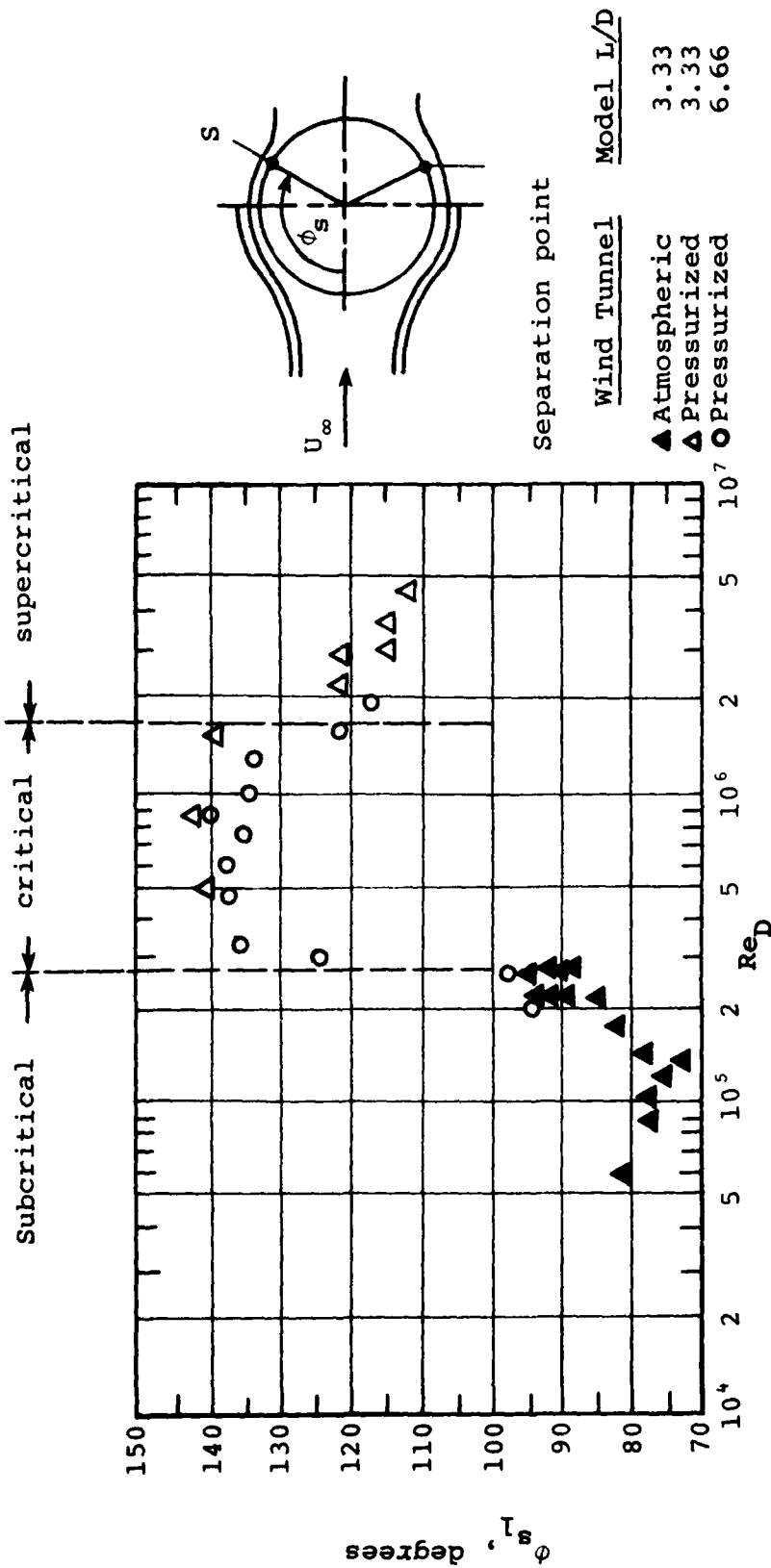


Figure 3.- Correlation of data on separation point location for incompressible flow past circular cylinders; taken from reference 8.

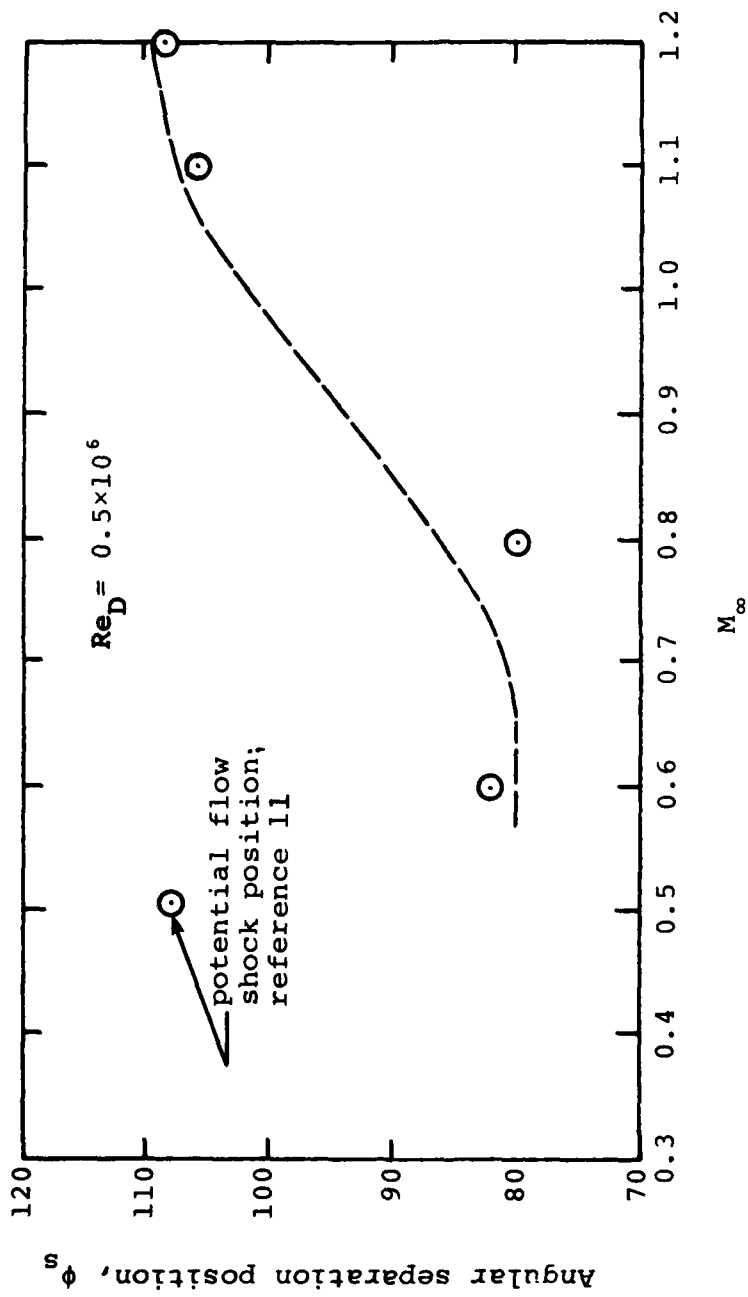
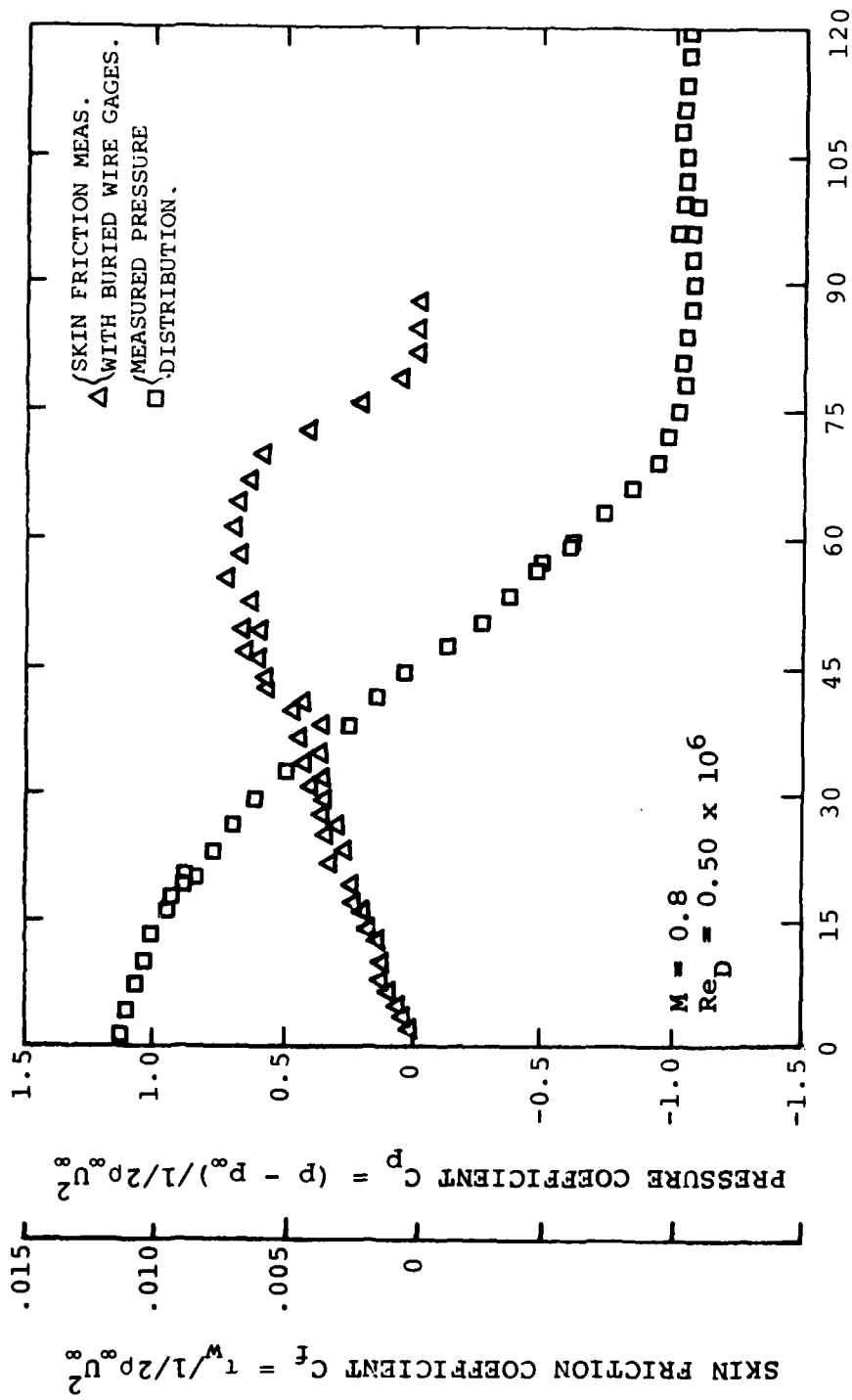


Figure 4.- Effect of Mach number on position of turbulent separation on circular cylinder in crossflow.



ANGLE FROM FORWARD STAGNATION POINT, deg  
 Figure 5.- Skin friction and pressure distribution on circular cylinder in crossflow.

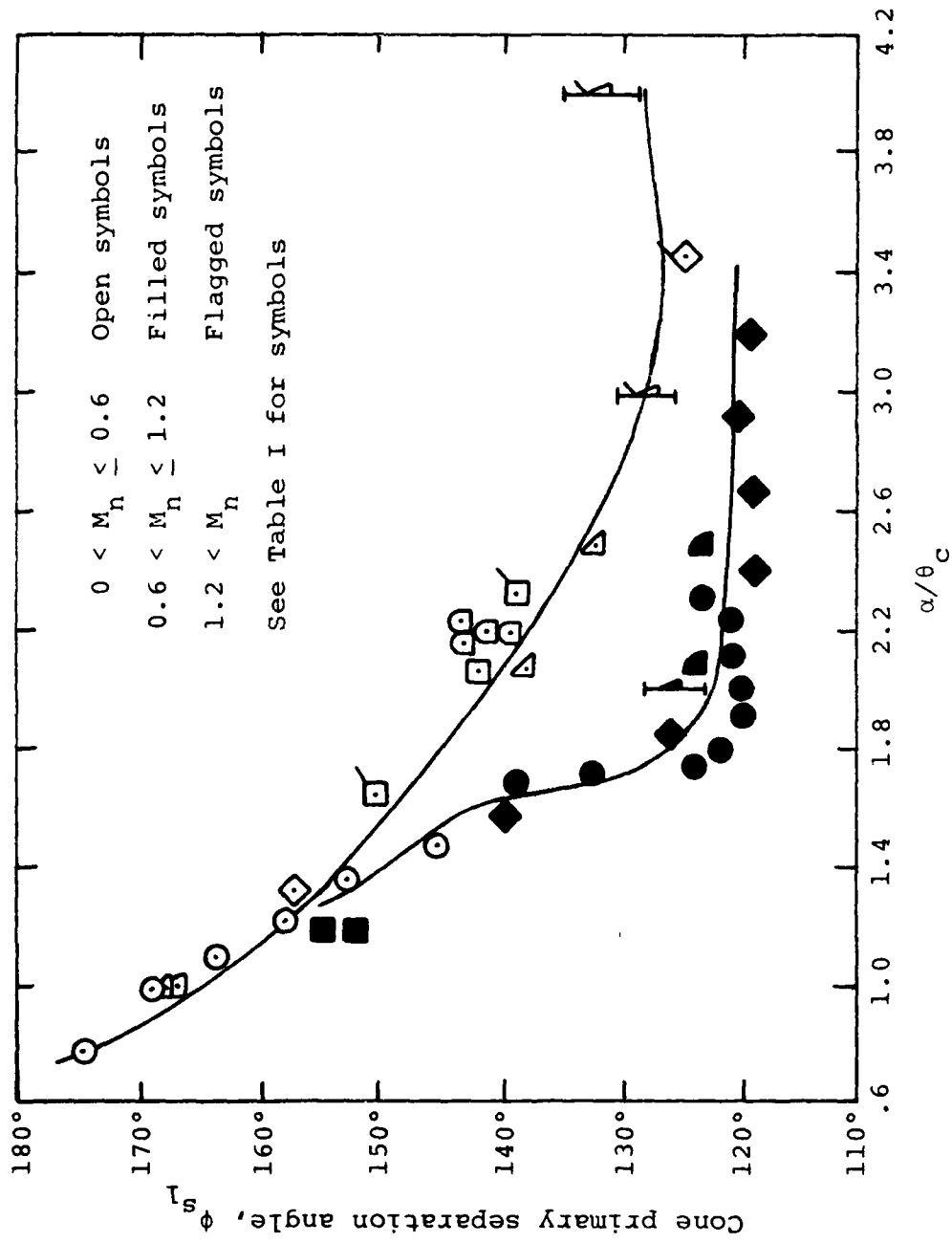


Figure 6.- Correlation of cone primary separation location.

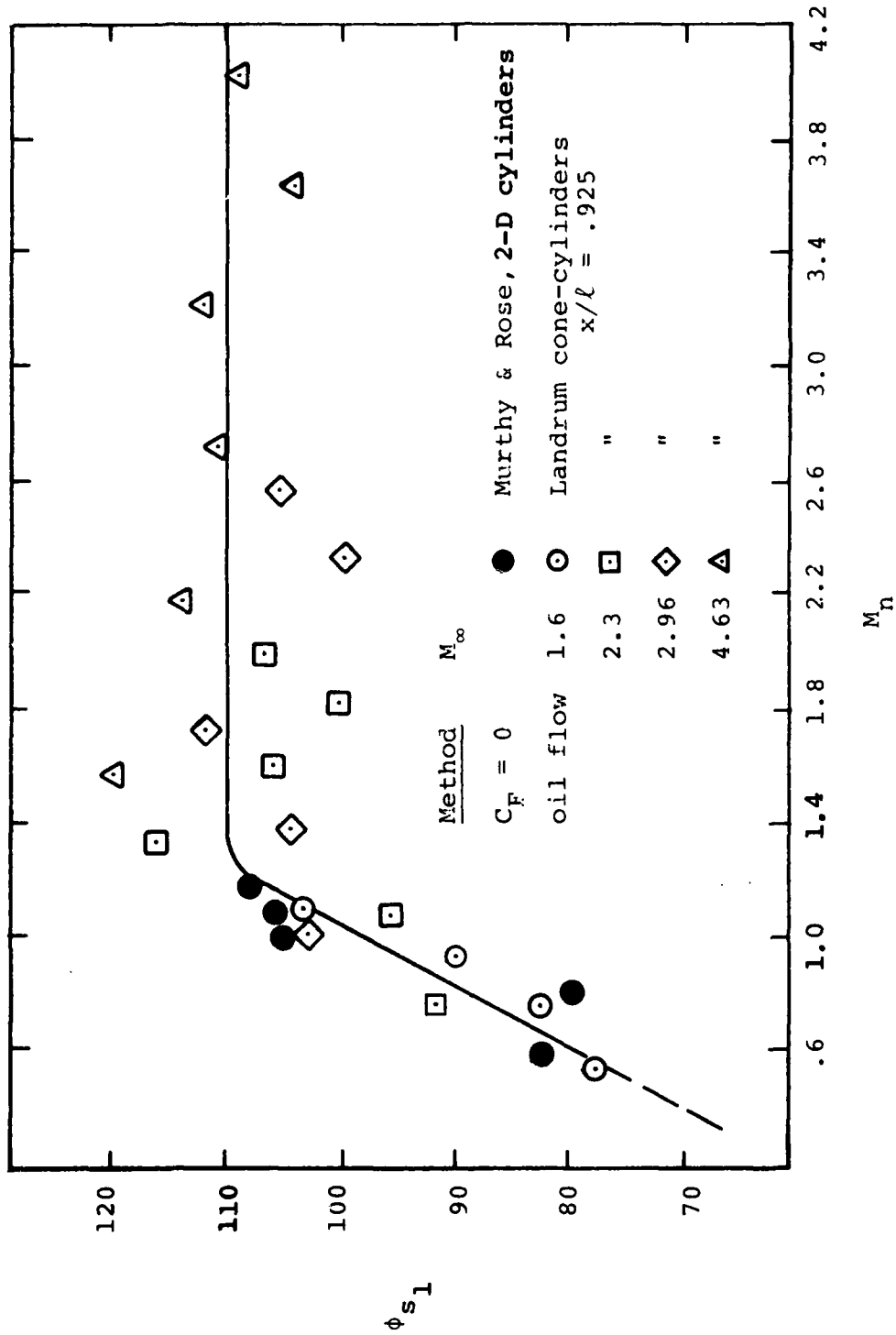


Figure 7.- Primary separation line locations for 2-D circular cylinders and cylindrical afterbodies ( $x/l = .925$ ) of cone-cylinders.

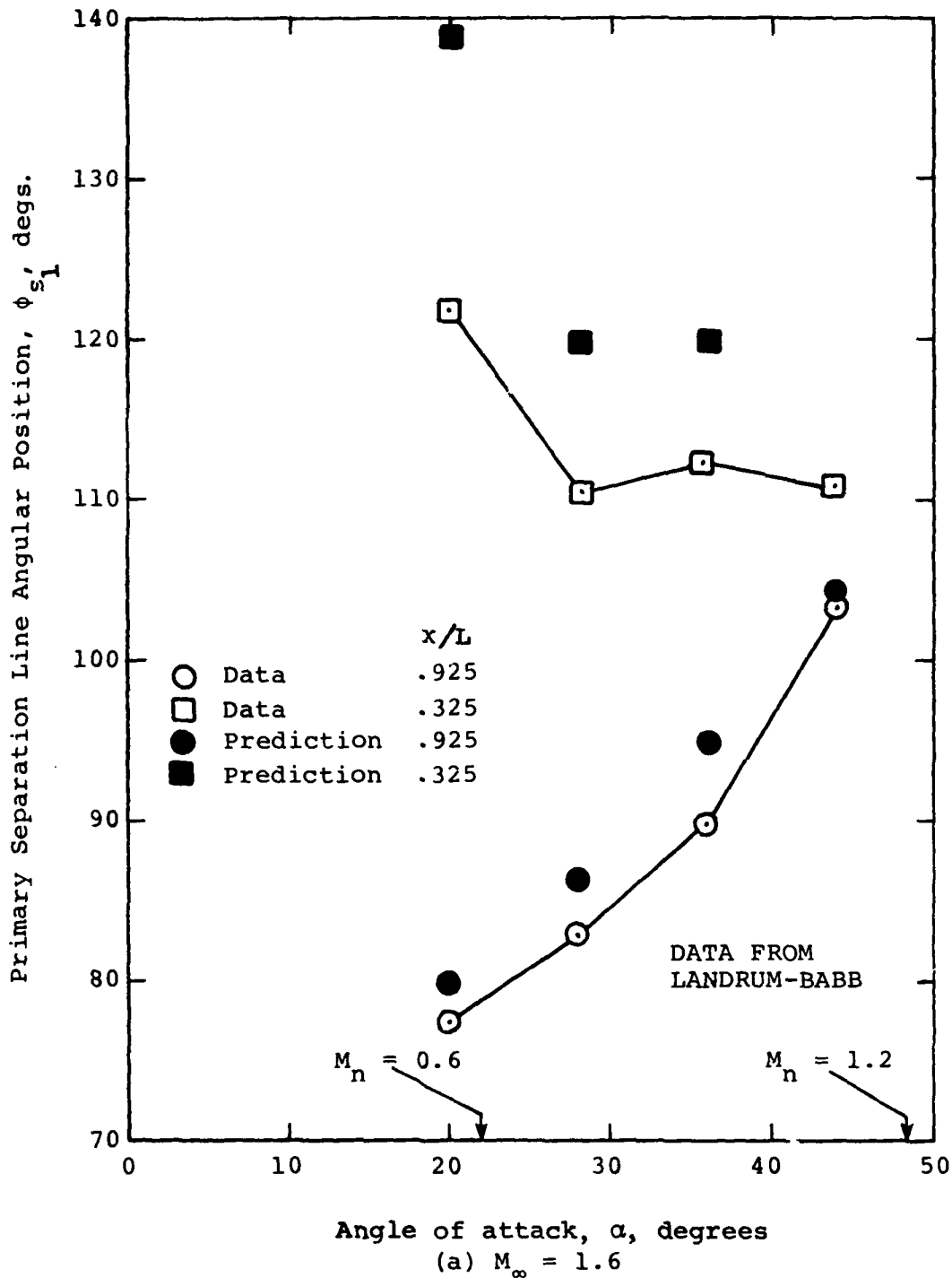
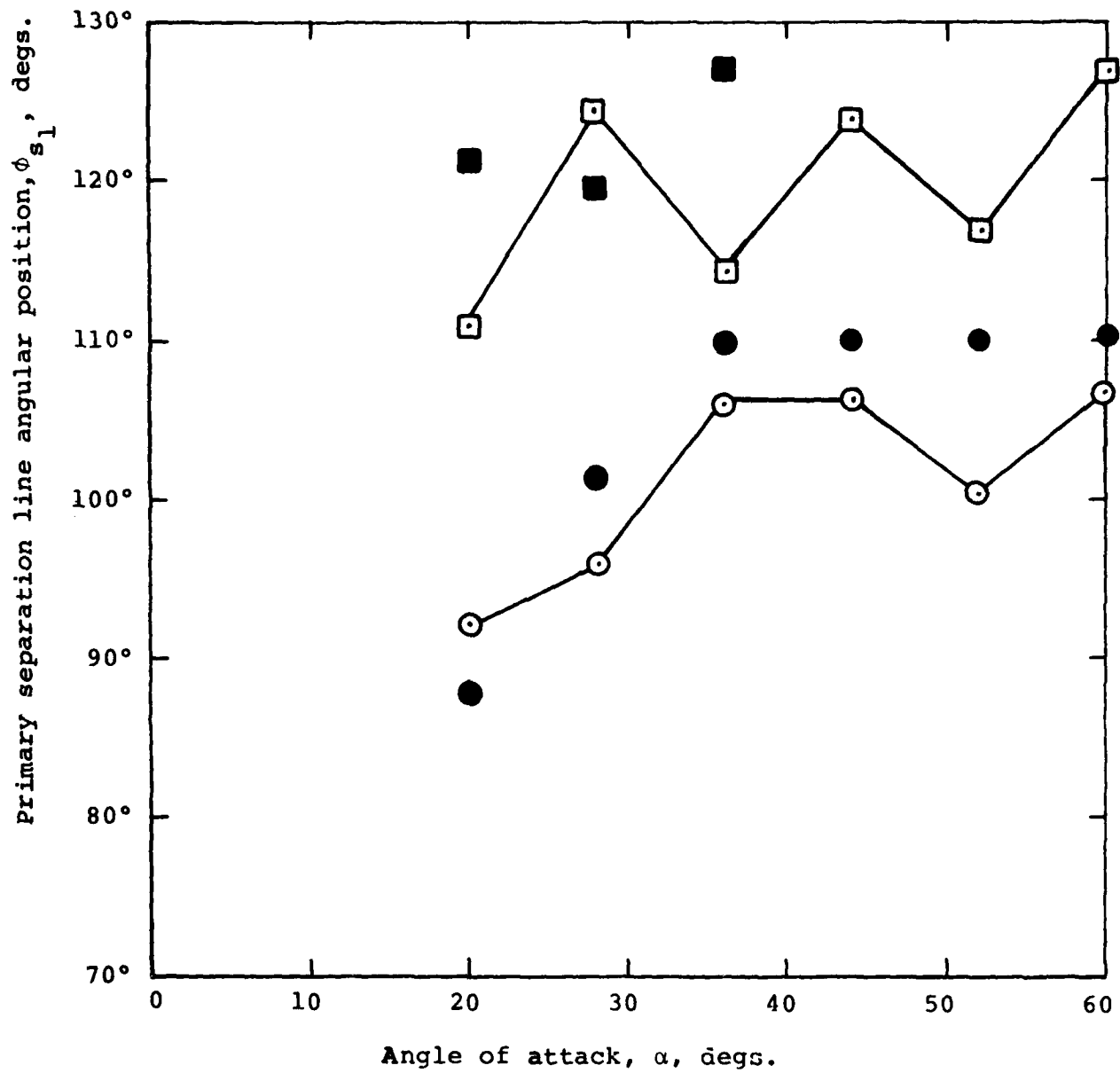
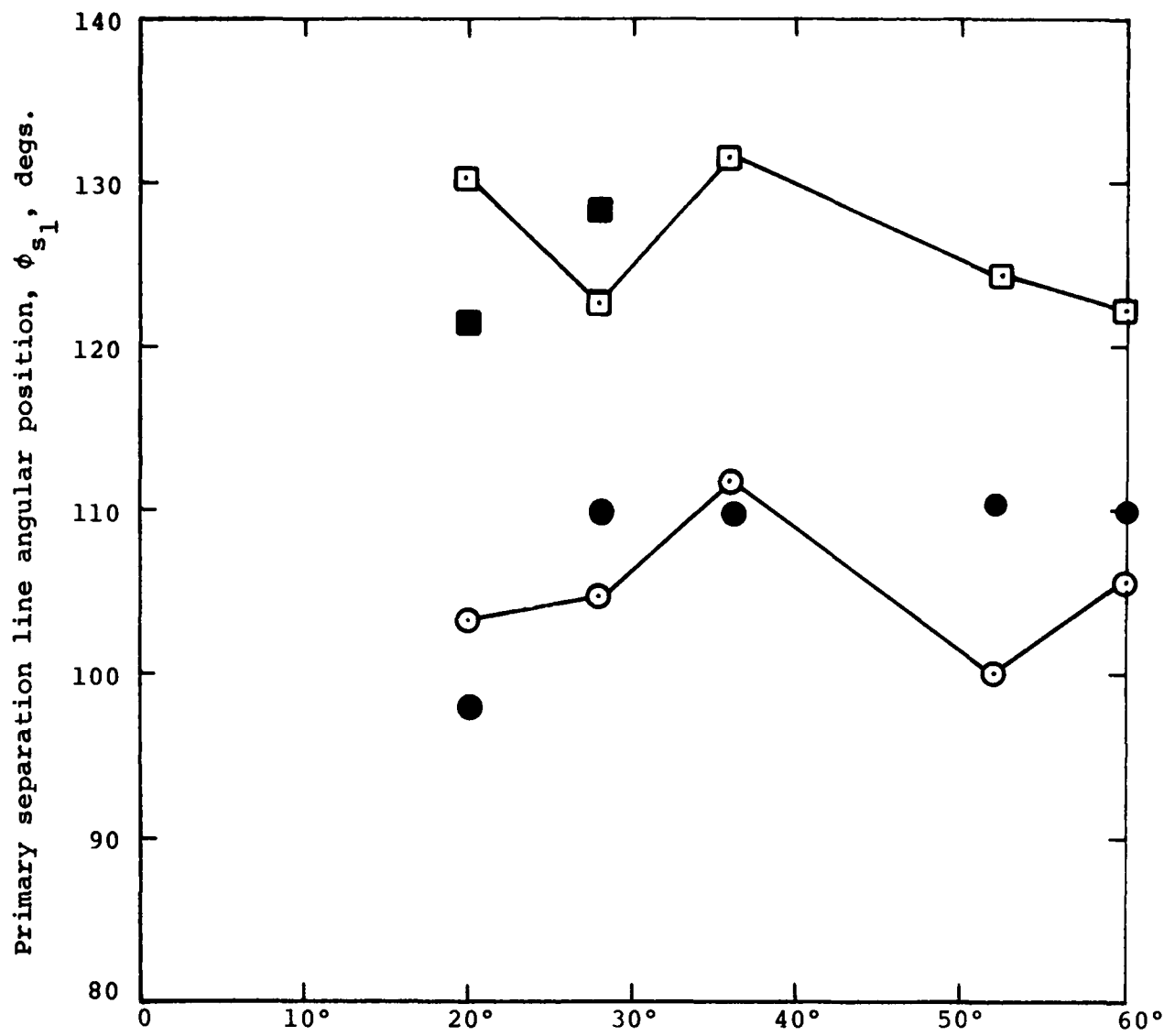


Figure 8.- Comparison of predicted and measured primary separation line positions on cone-cylinder body;  $\theta_c = 9.5^\circ$ ,  $L/D = 6.67$ .



(b)  $M_\infty = 2.30$

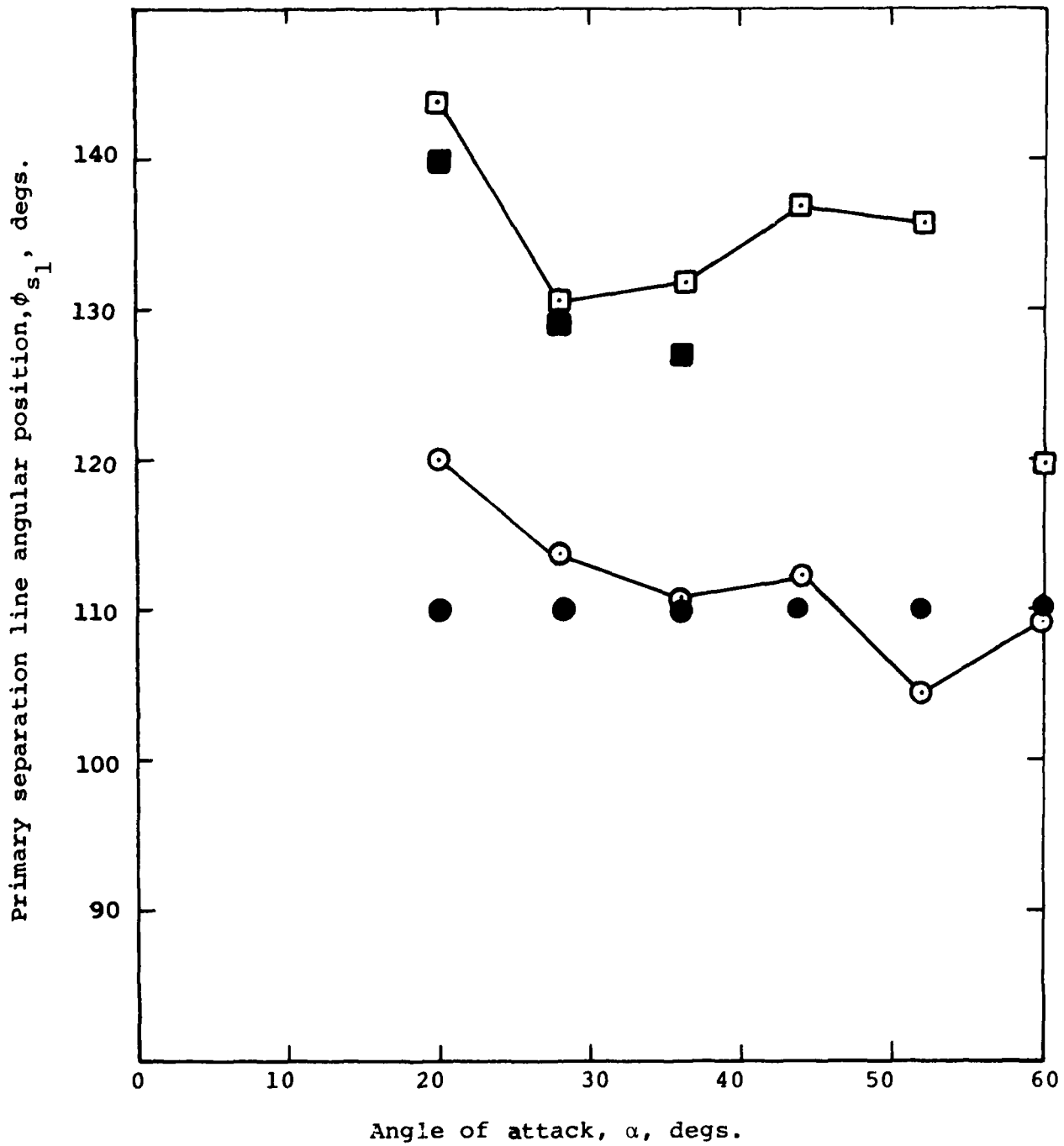
Figure 8.- Continued.



Angle of attack,  $\alpha$ , degs.

(c)  $M_\infty = 2.86$

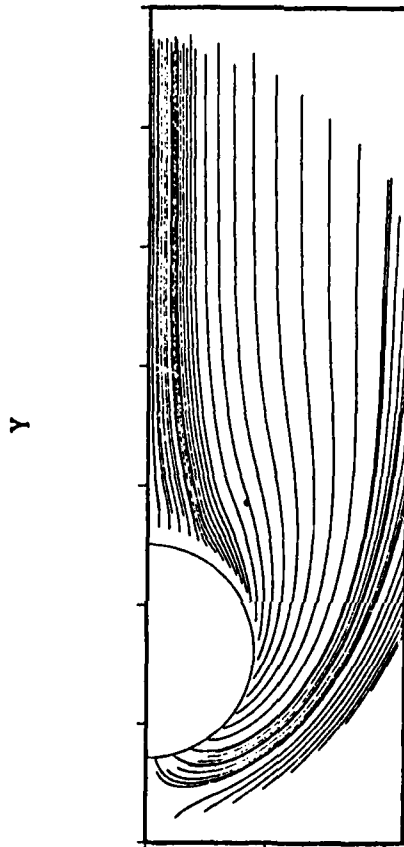
Figure 8.- Continued.



(a)  $M_{\infty} = 4.63$

Figure 8.- Concluded.

30X36 MESH



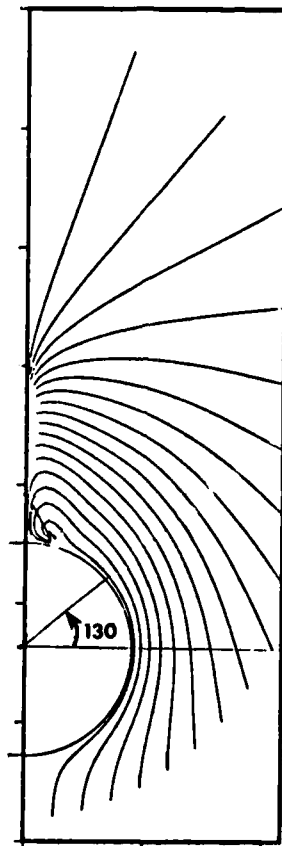
$M_\infty = 3.00$      $\alpha = 25.00$

$z = 50$

(a) Crossflow plane

Figure 9.- Streamlines (particle paths) from Euler code solution with no Kutta condition

30X36 MESH



$M_\infty = 3.00$      $\alpha = 25.00$

$z = 50$

(b) On spherical surface centered on apex

Figure 9.- Concluded

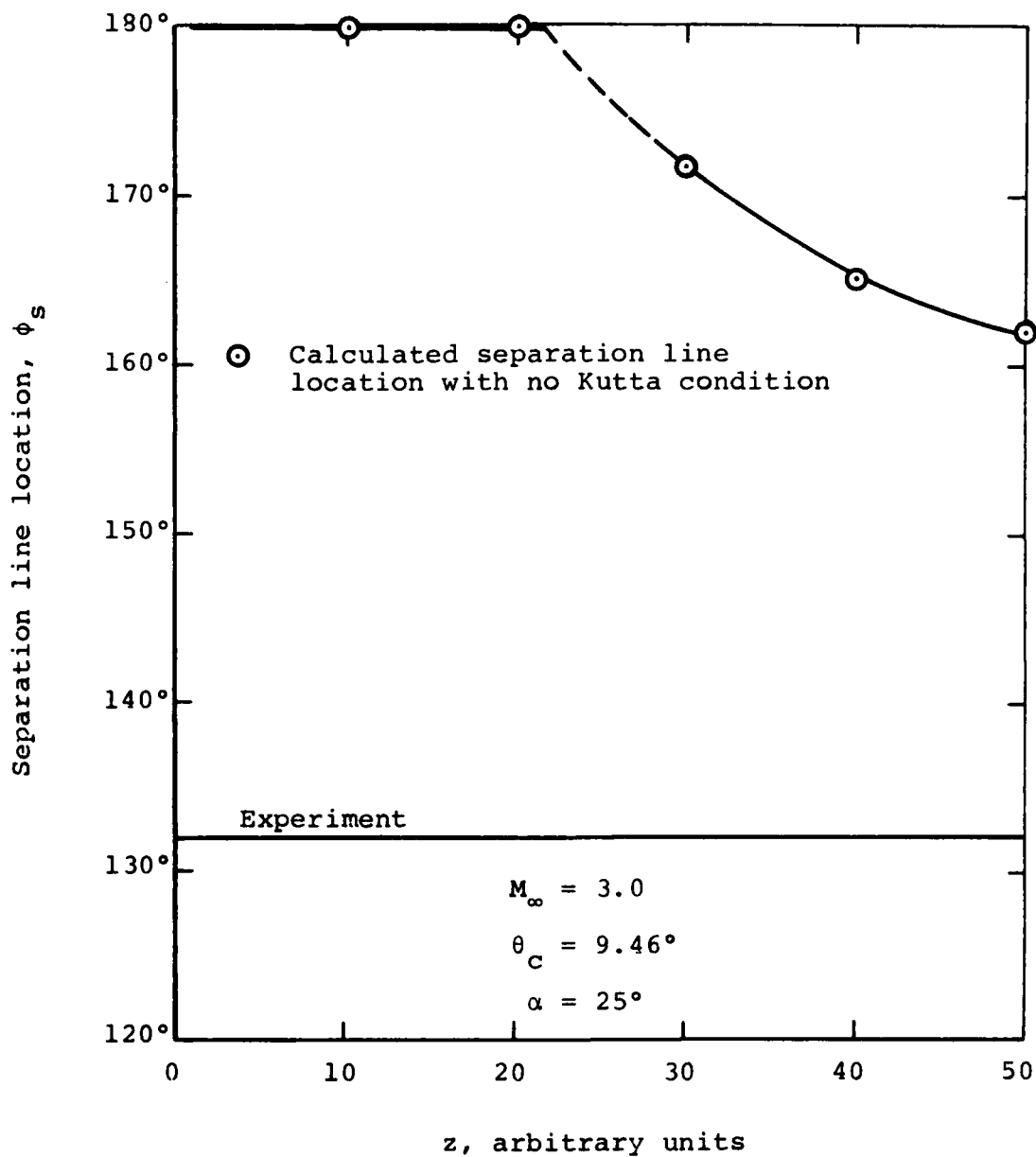
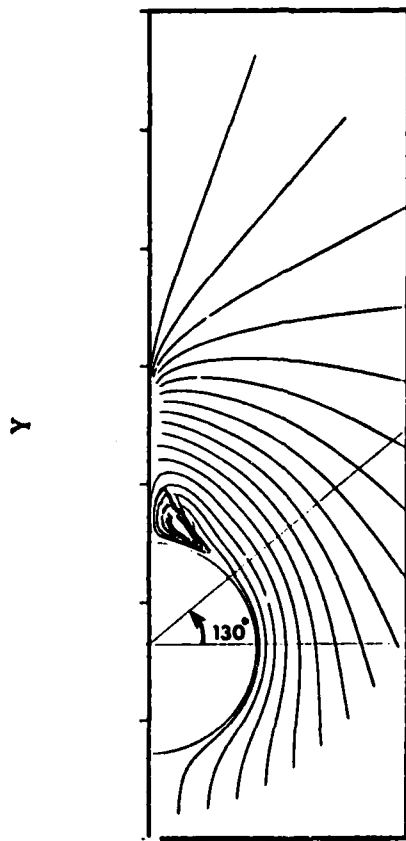


Figure 10.- Development of separation by Euler equation on cone at angle of attack; no imposed Kutta condition.

30X36 MESH



$$M_{\infty} = 3.00 \quad \alpha = 25.00$$

$$\phi_{s_1} = 130^\circ \quad \theta_c = 9.46^\circ$$

Figure 11.- Streamlines on spherical surface centered at apex from Euler solution for cone with Kutta Condition

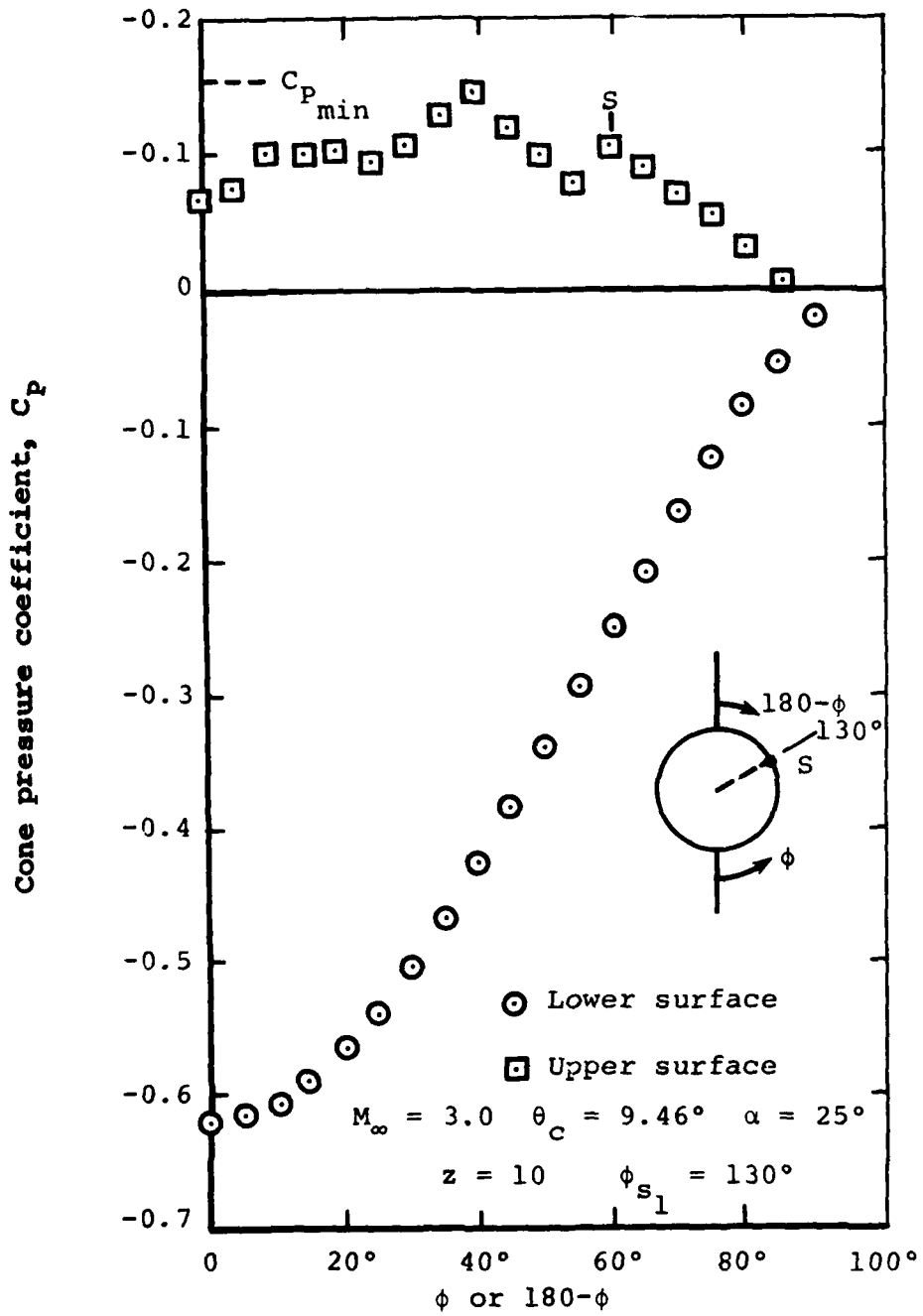


Figure 12.- Calculated surface pressure distribution on cone with Kutta condition

30 x 36 MESH

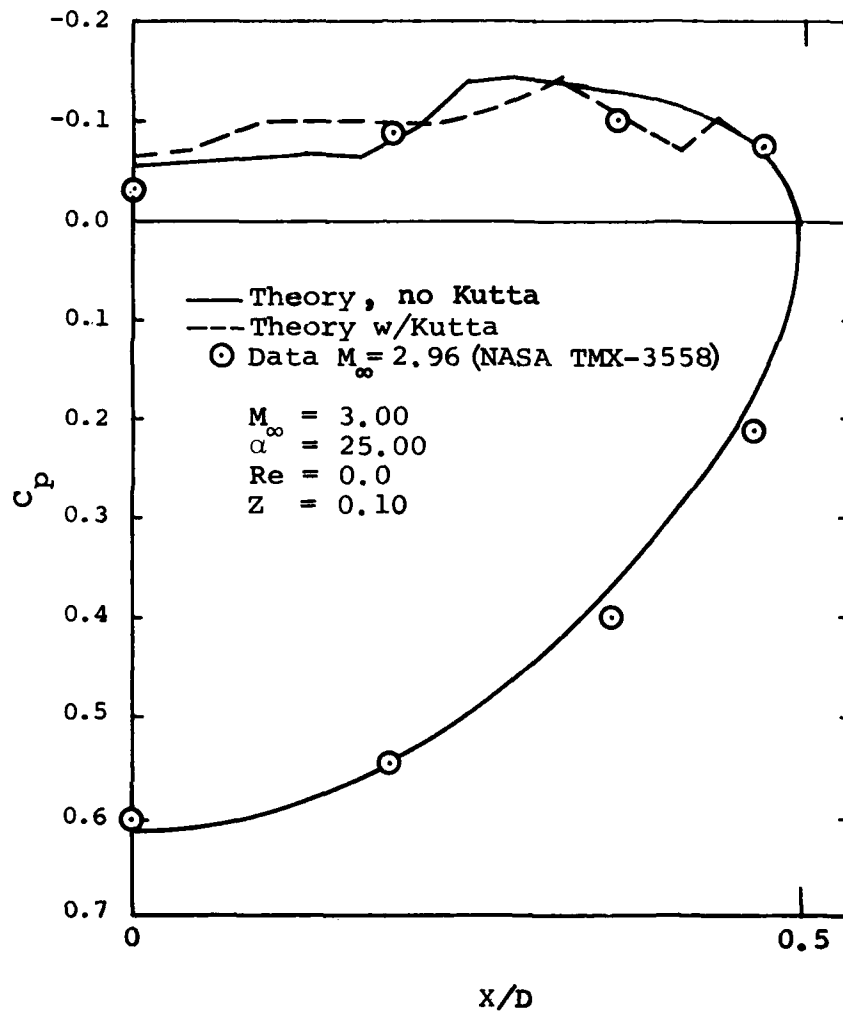


Figure 13.- Pressure distribution on cone as calculated by Euler equation with Kutta condition and as measured.

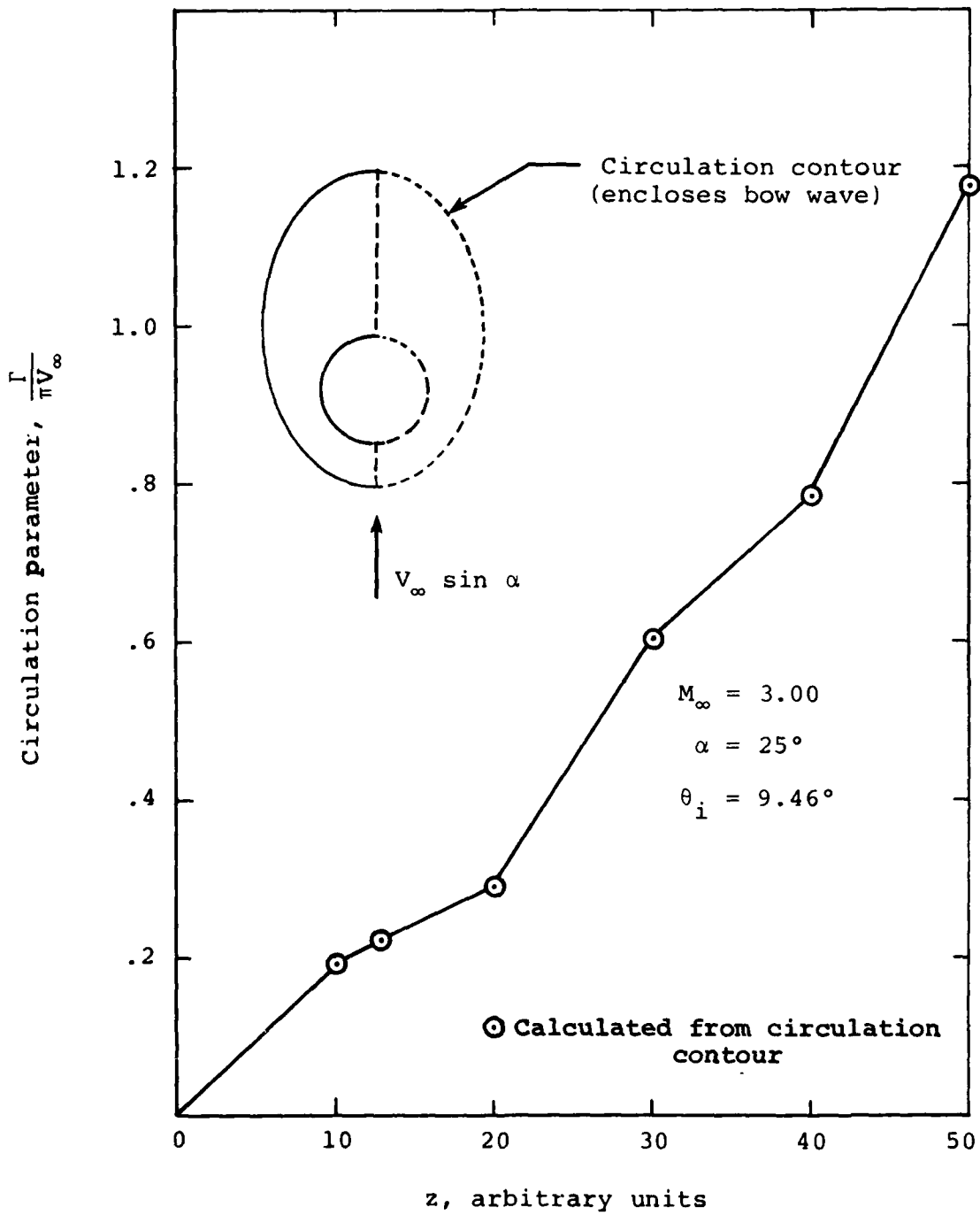


Figure 14.- Growth of circulation parameter along cone with no Kutta condition imposed.

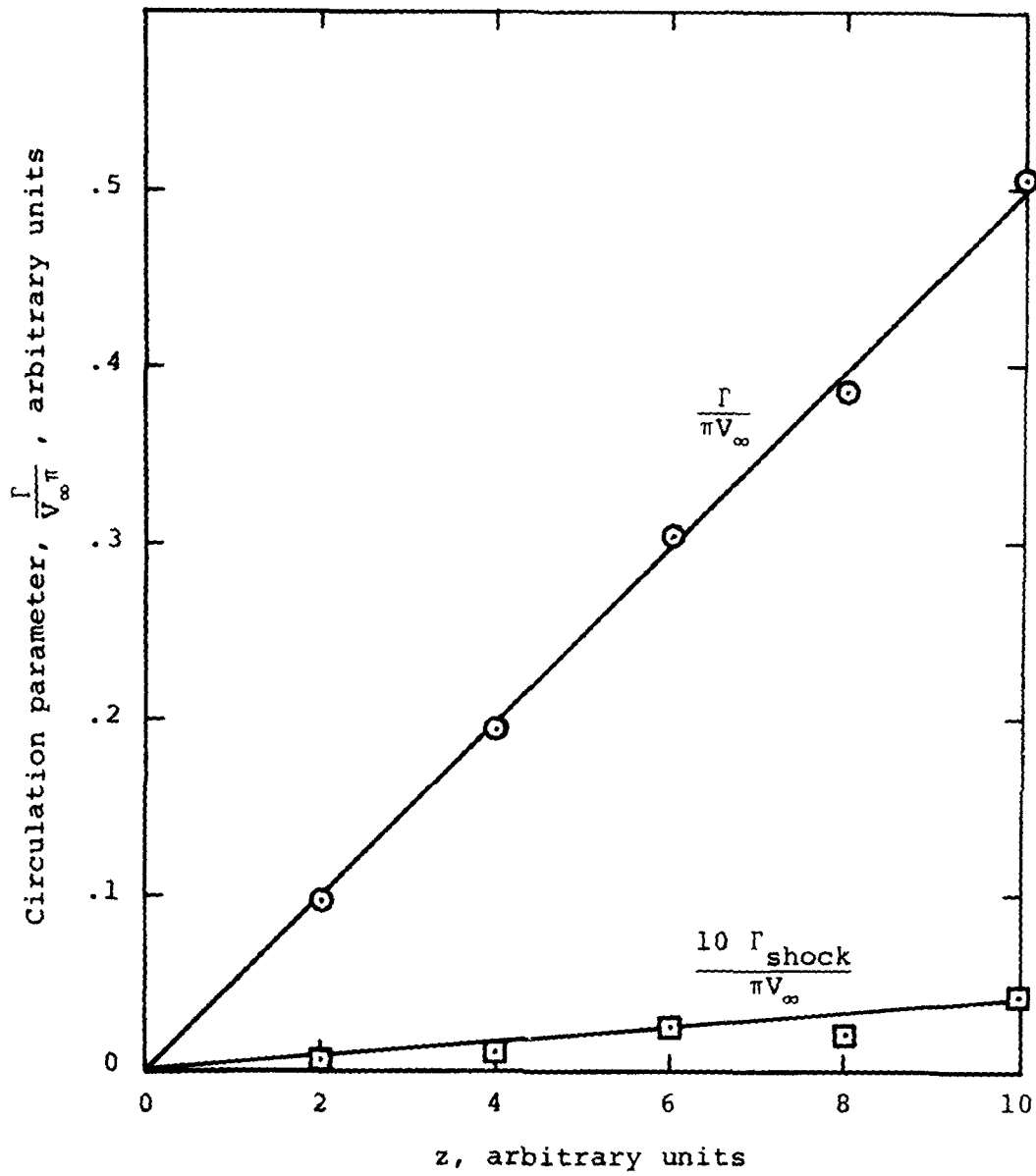


Figure 15.- Growth of circulation parameters along cone with Kutta condition

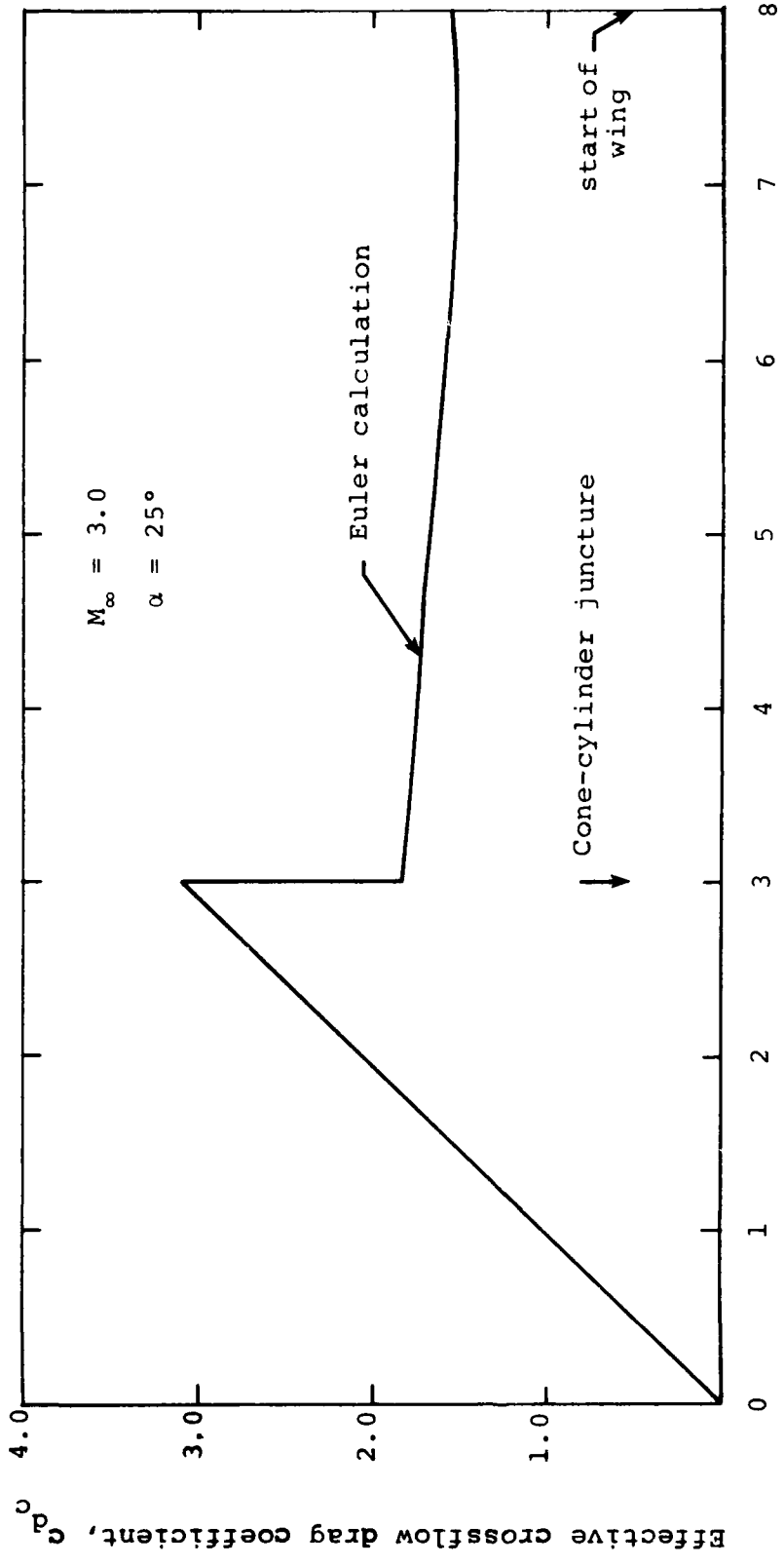
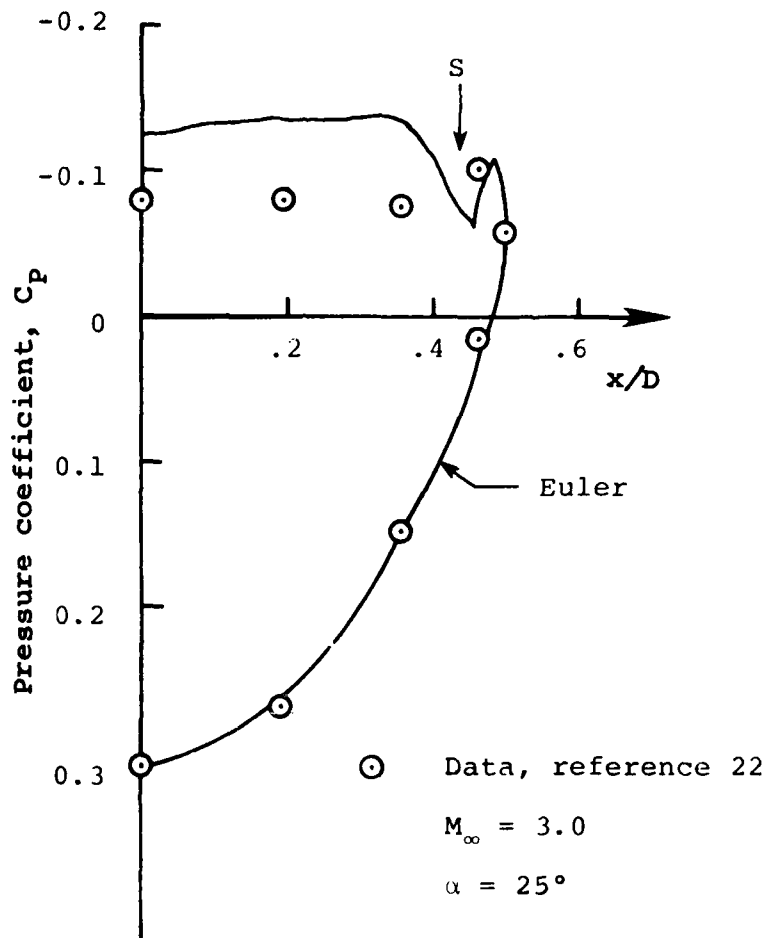
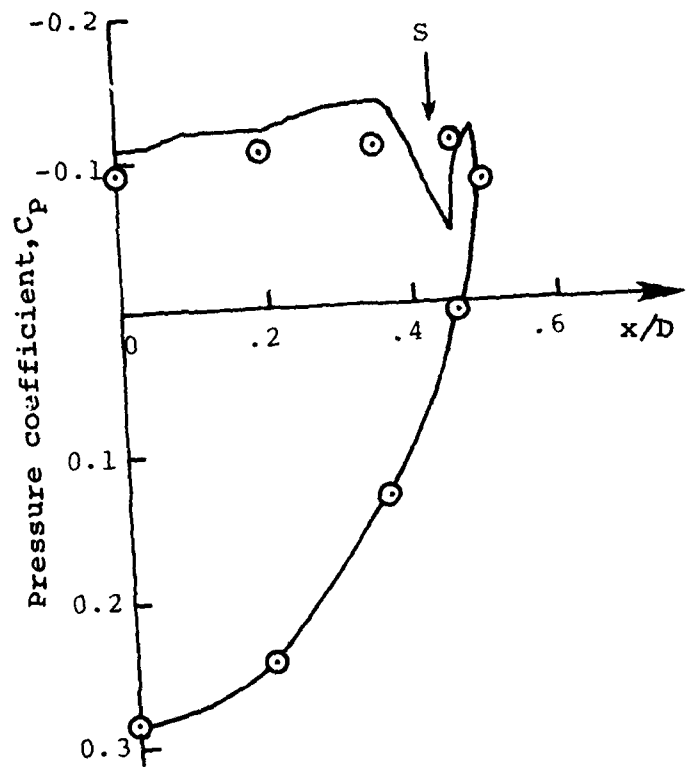


Figure 16.- Shape of body axial loading distribution for subject wing-body combination



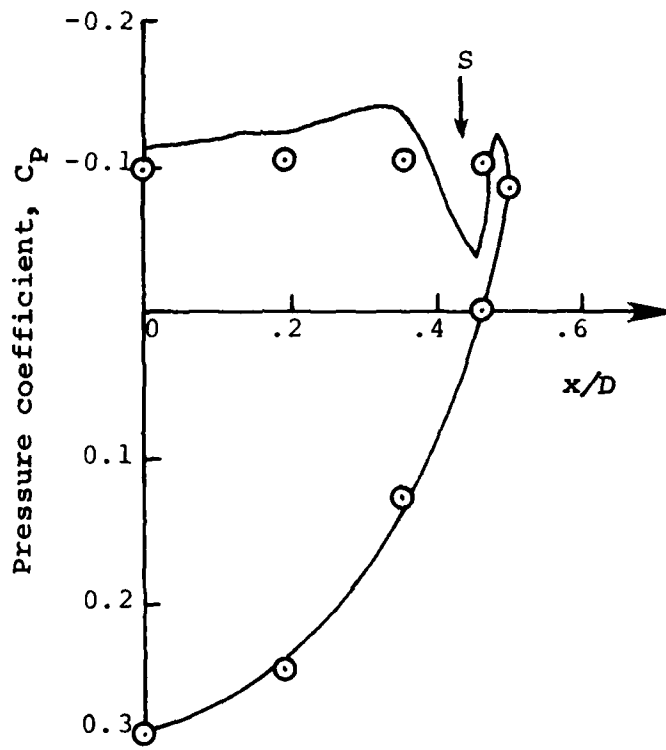
(a)  $z/D = 3.8$

Figure 17.- Comparison of pressure distribution as calculated by the Euler code and as measured for example wing body combination.



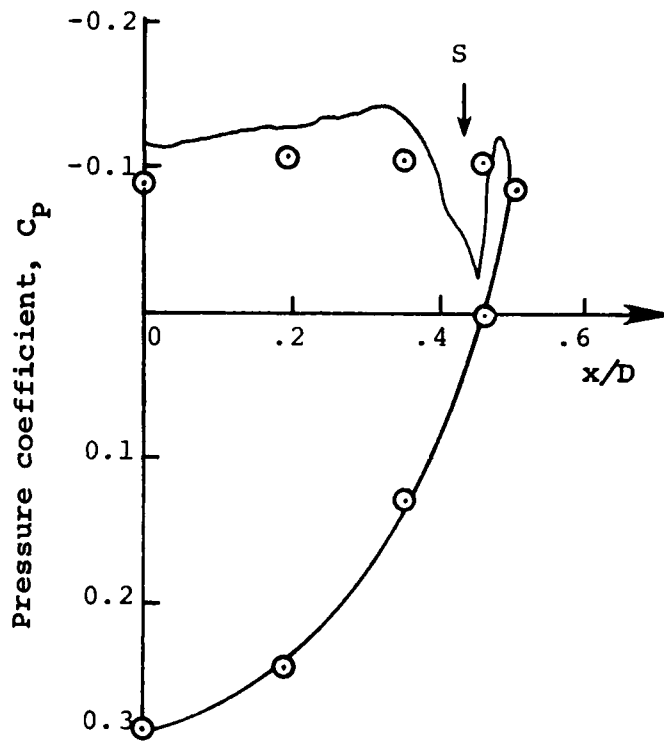
(b)  $z/D = 5.2$

Figure 17.- Continued



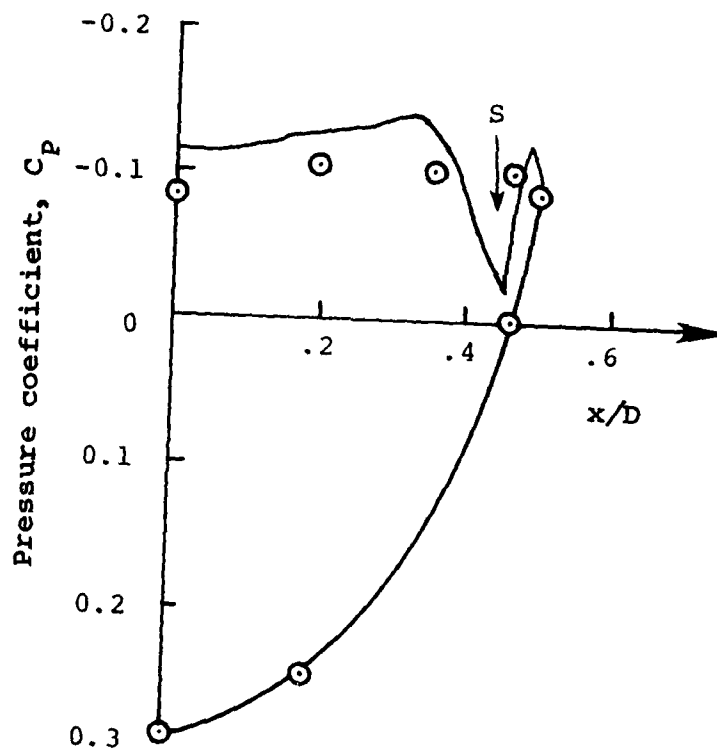
(c)  $z/D = 5.8$

Figure 17.- Continued



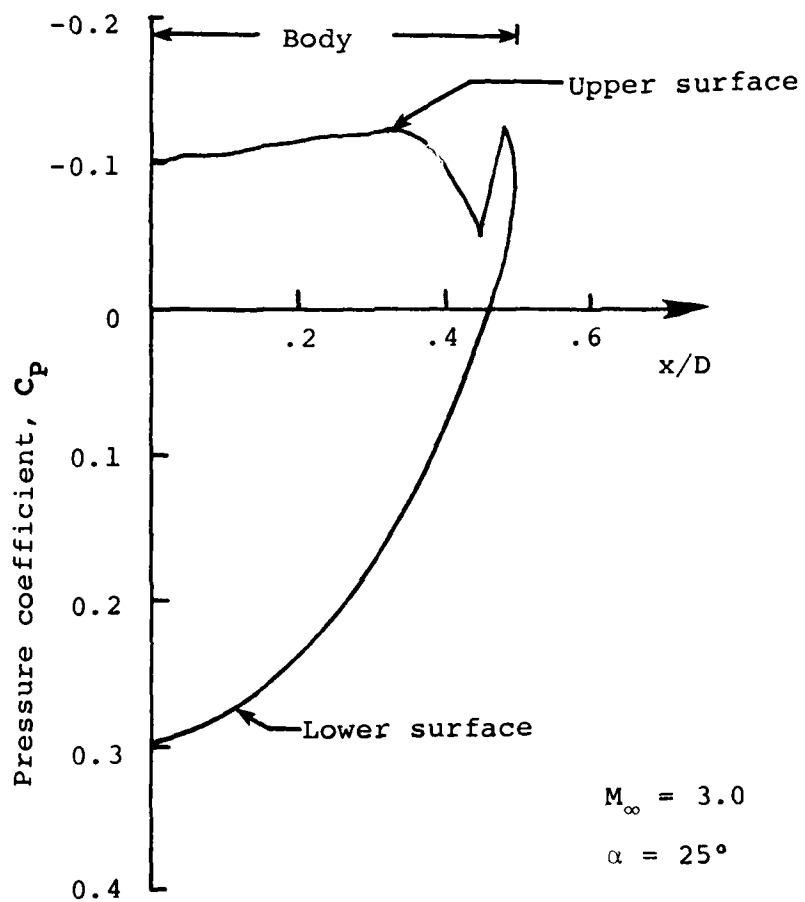
(d)  $z/D = 6.2$

Figure 17.- Continued



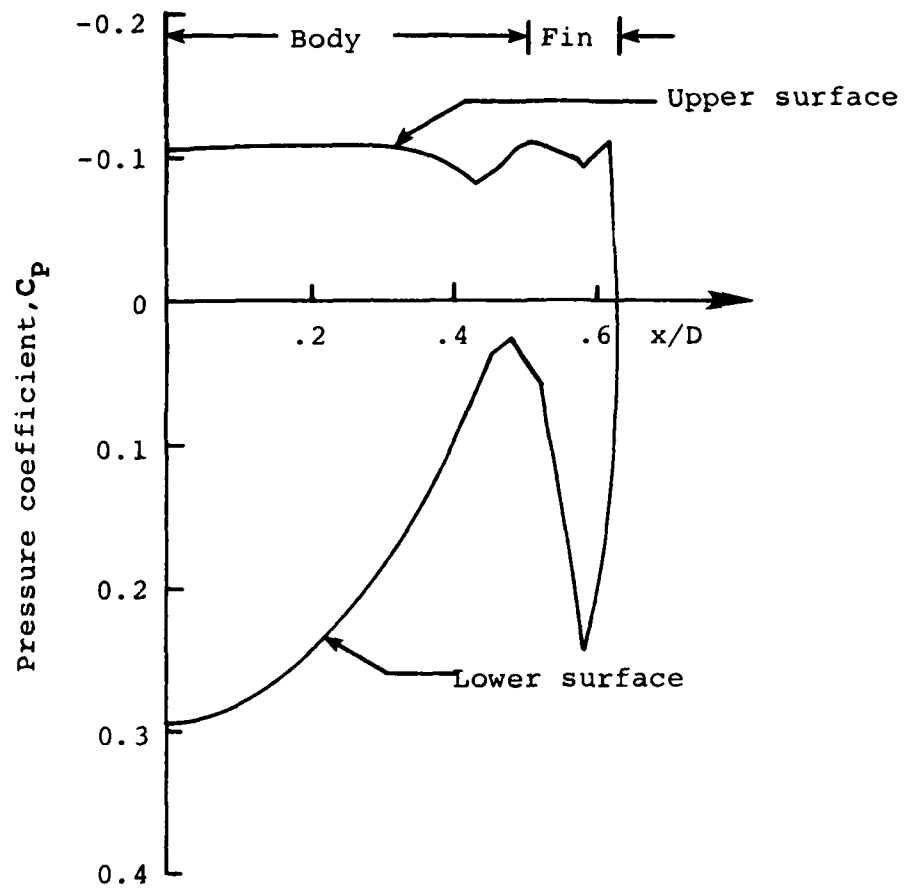
(e)  $z/D = 6.5$

Figure 17.- Concluded.



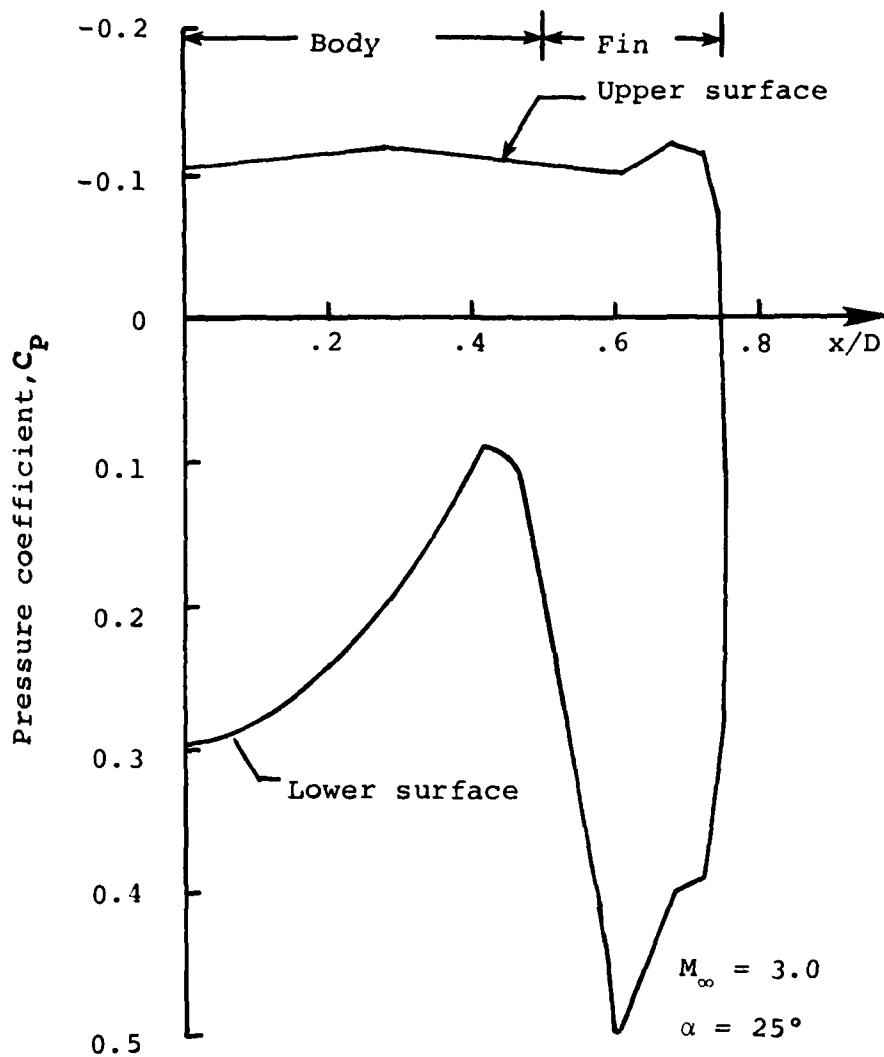
(a)  $z/D = 8.0$

Figure 18.- Pressure distributions in crossflow planes of winged part of example wing-body combinations.



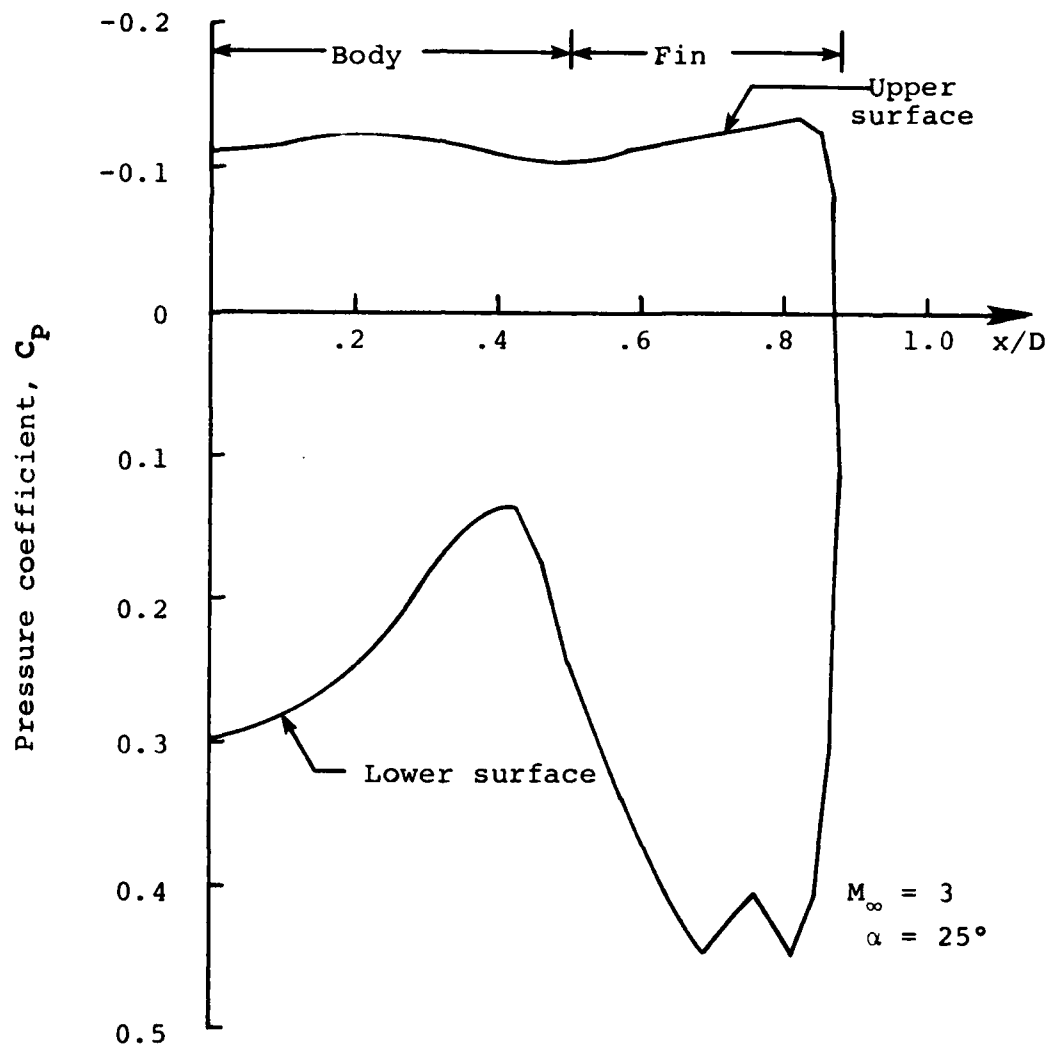
(b)  $z/D = 8.50$

Figure 18.- Continued.



(c)  $z/D = 9.0$

Figure 18.- Continued.



(d)  $z/D = 9.5$

Figure 18.- Continued.

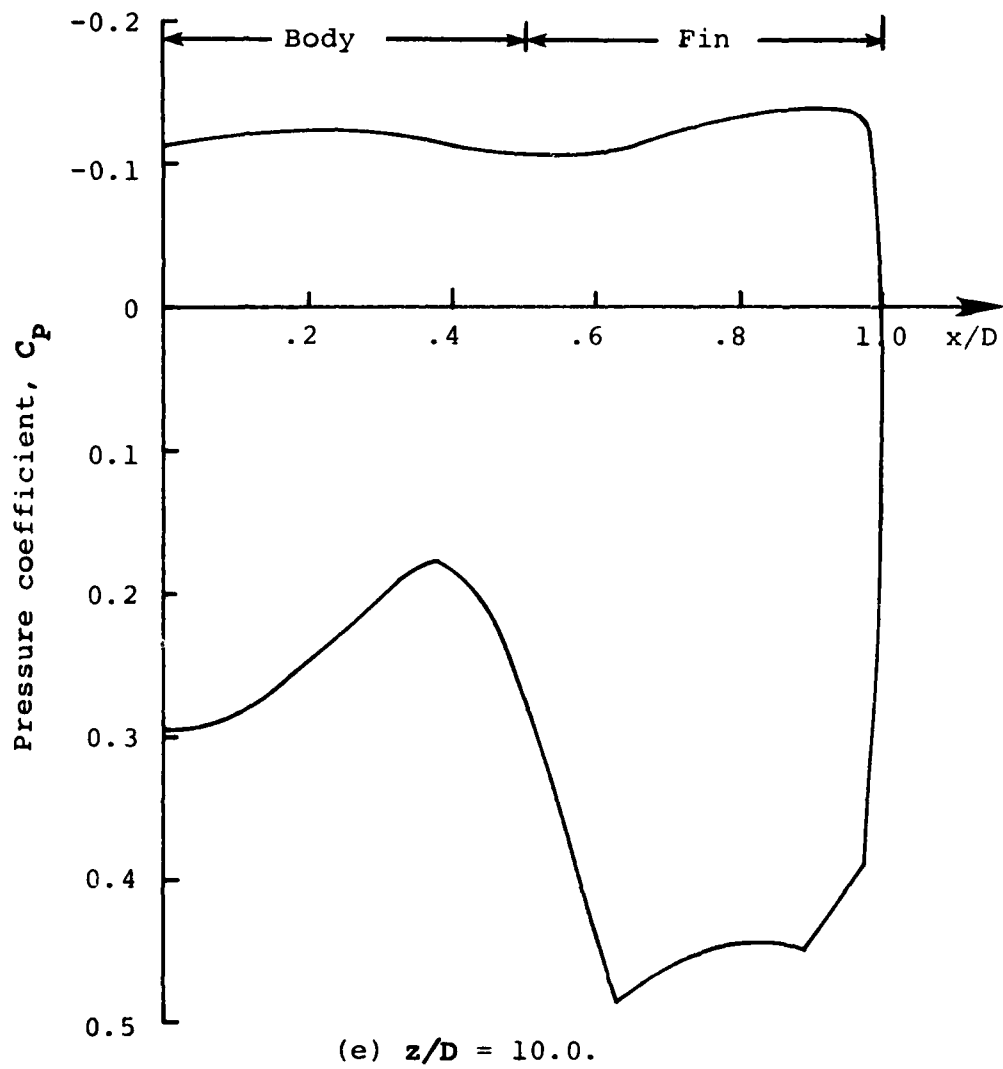


Figure 18.- Concluded.

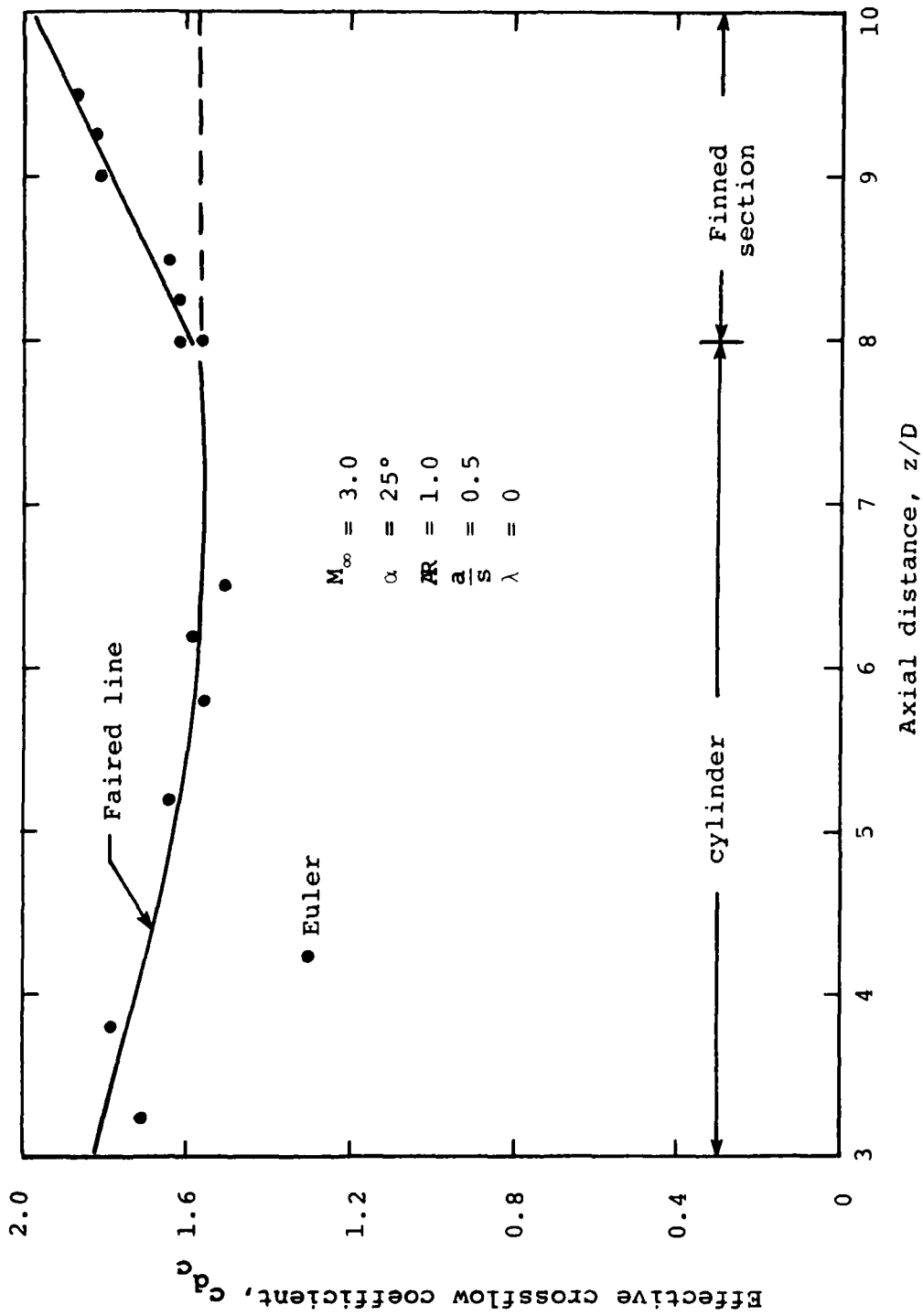


Figure 19.- Shape of axial loading over cylinder and finned section of example wing body combination.

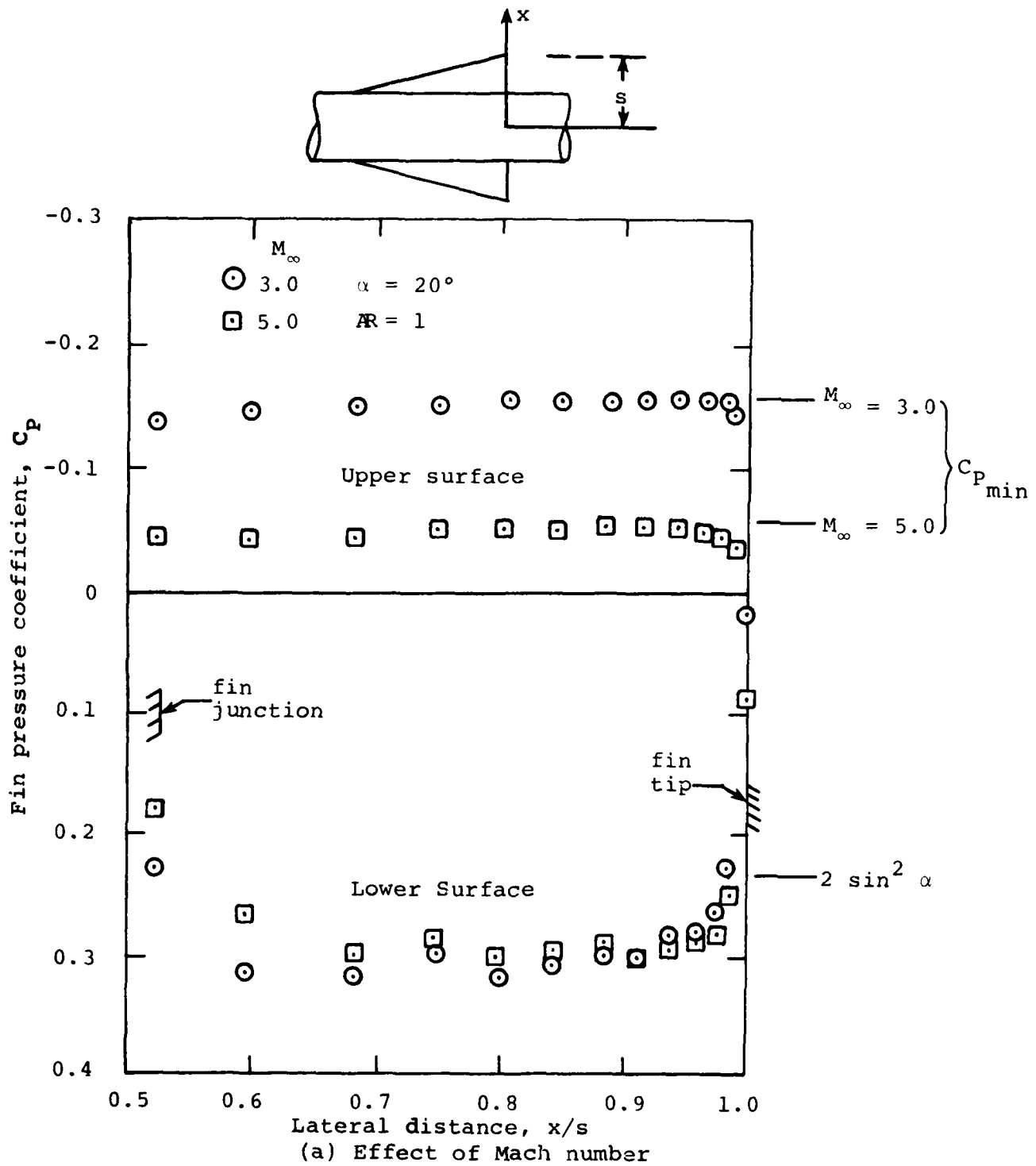
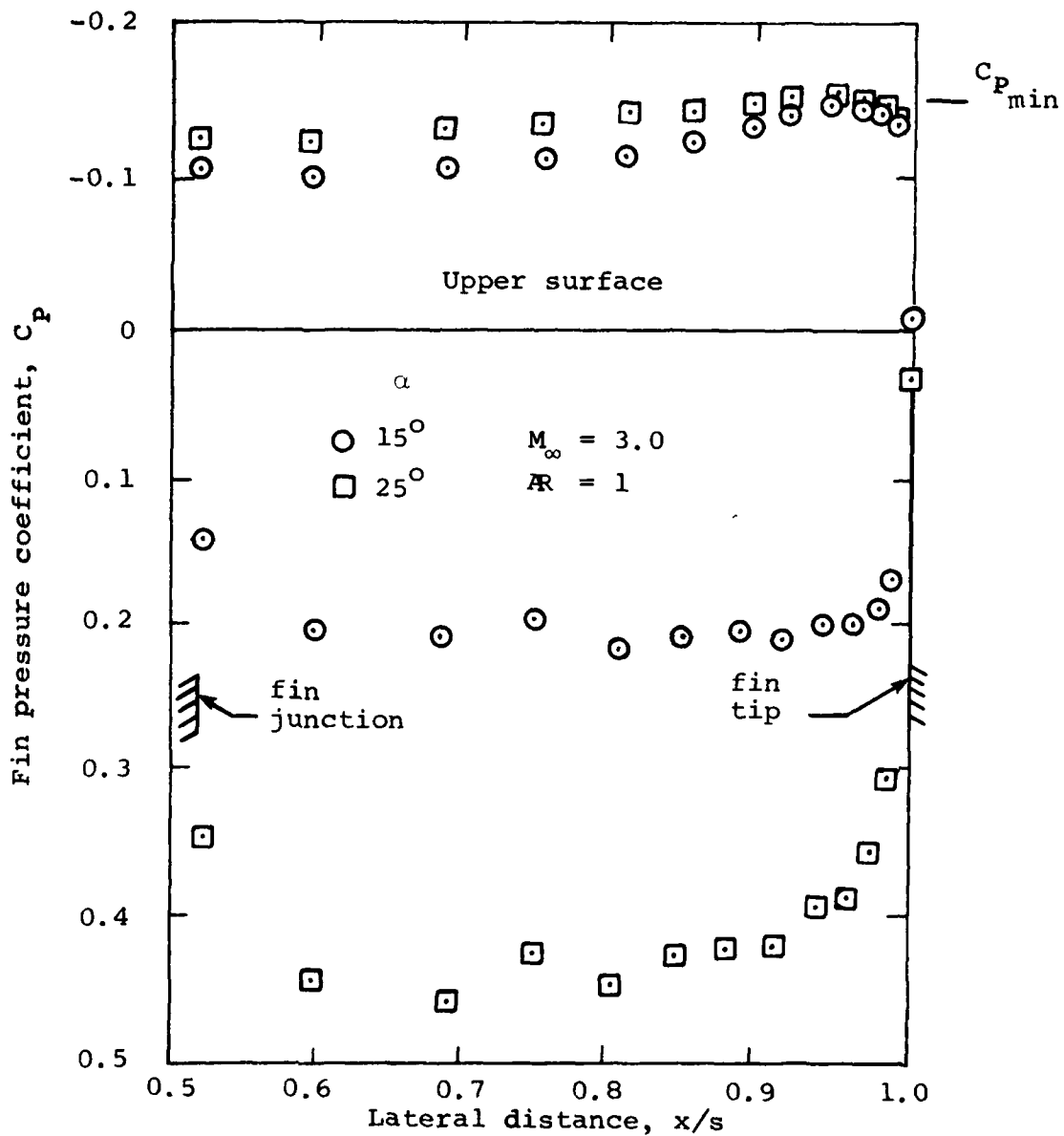
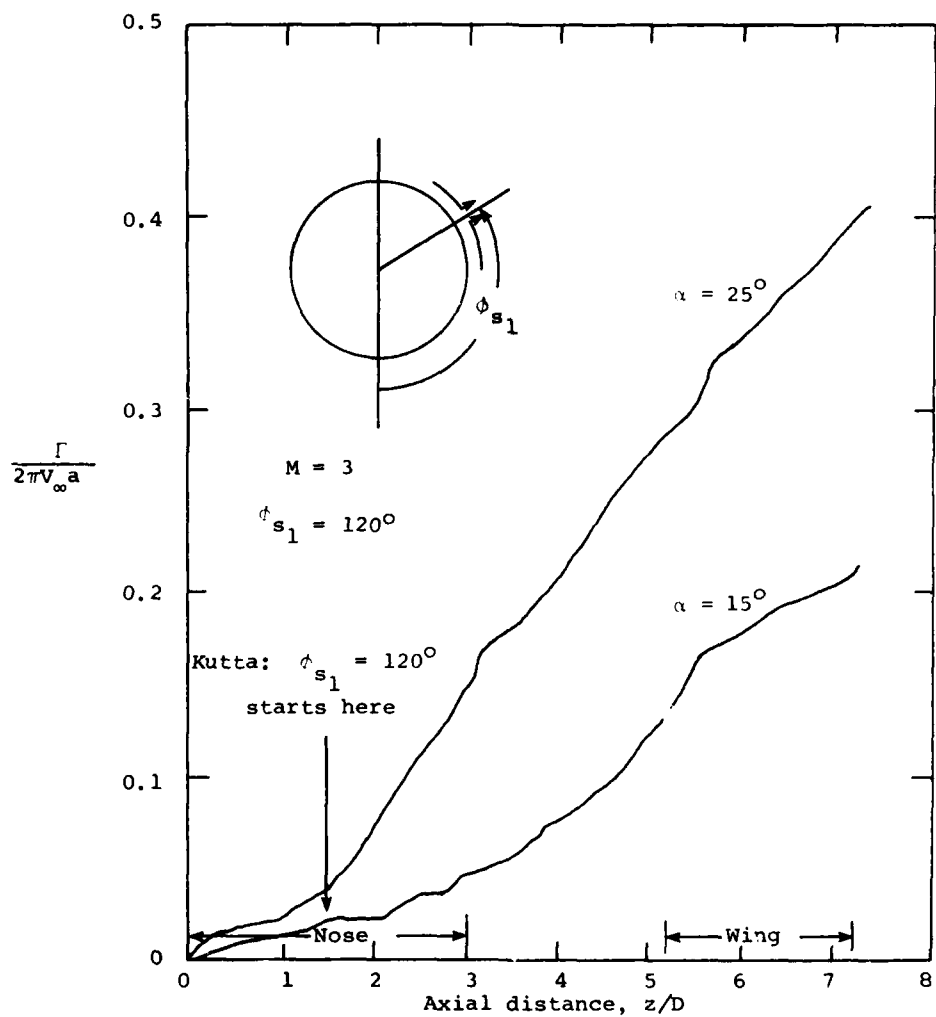
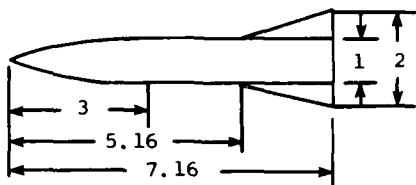


Figure 20.- Pressure distributions at trailing edge of fin mounted on circular body as calculated by an Euler code.



(b) Effect of angle of attack

Figure 20.- Pressure distributions at trailing edge of fin mounted on circular body as calculated by an Euler code.



(a) Effect of angle of attack

Figure 21.- Nondimensional circulation in right half plane as calculated by Euler equations for example wing-body combinations.

AD-A120 216

NIELSEN ENGINEERING AND RESEARCH INC MOUNTAIN VIEW CA F/G 20/4  
EULER SOLUTIONS OF SUPERSONIC WING-BODY INTERFERENCE AT HIGH IN--ETC(U)  
AUG 82 J N NIELSEN, G D KUHN, G H KLOPFER N00014-78-C-0490  
NEAR-TR-263 NL

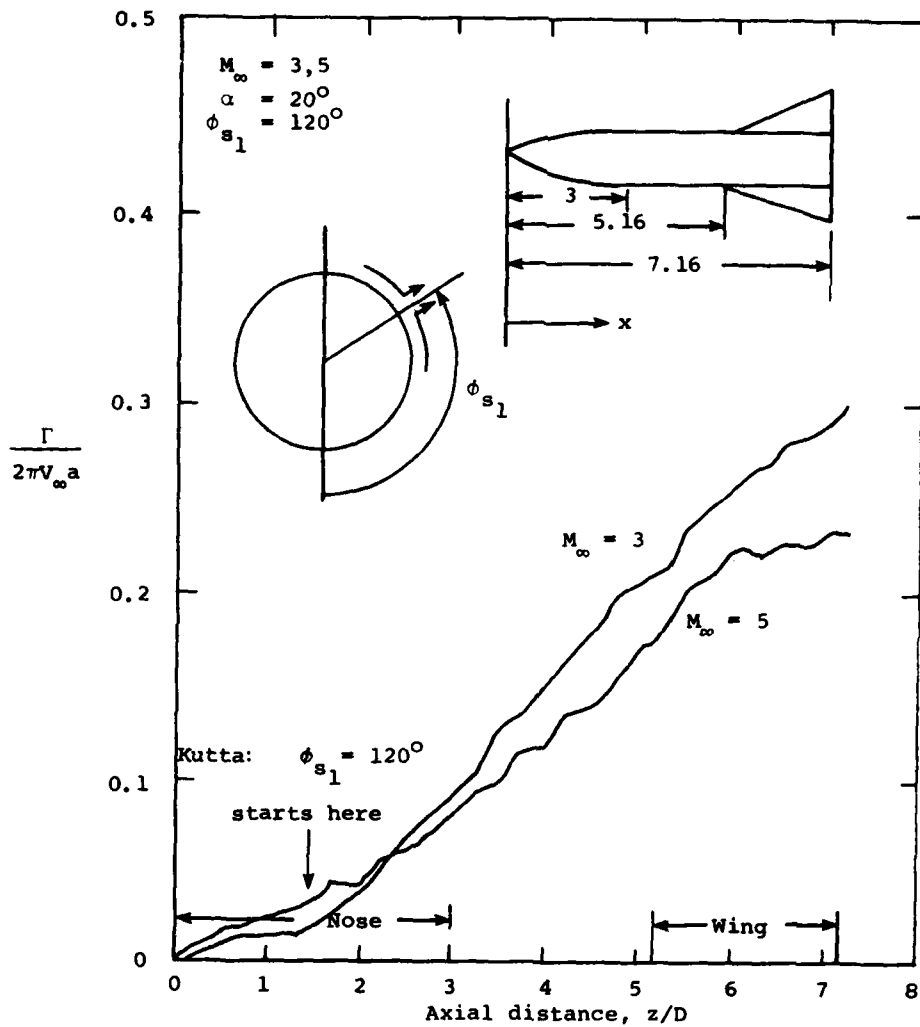
UNCLASSIFIED

2 of 2

40 A  
1,000 B



END  
DATE  
FILED  
11-82  
DTIC



(b) Effect of Mach number

Figure 21.- Concluded.

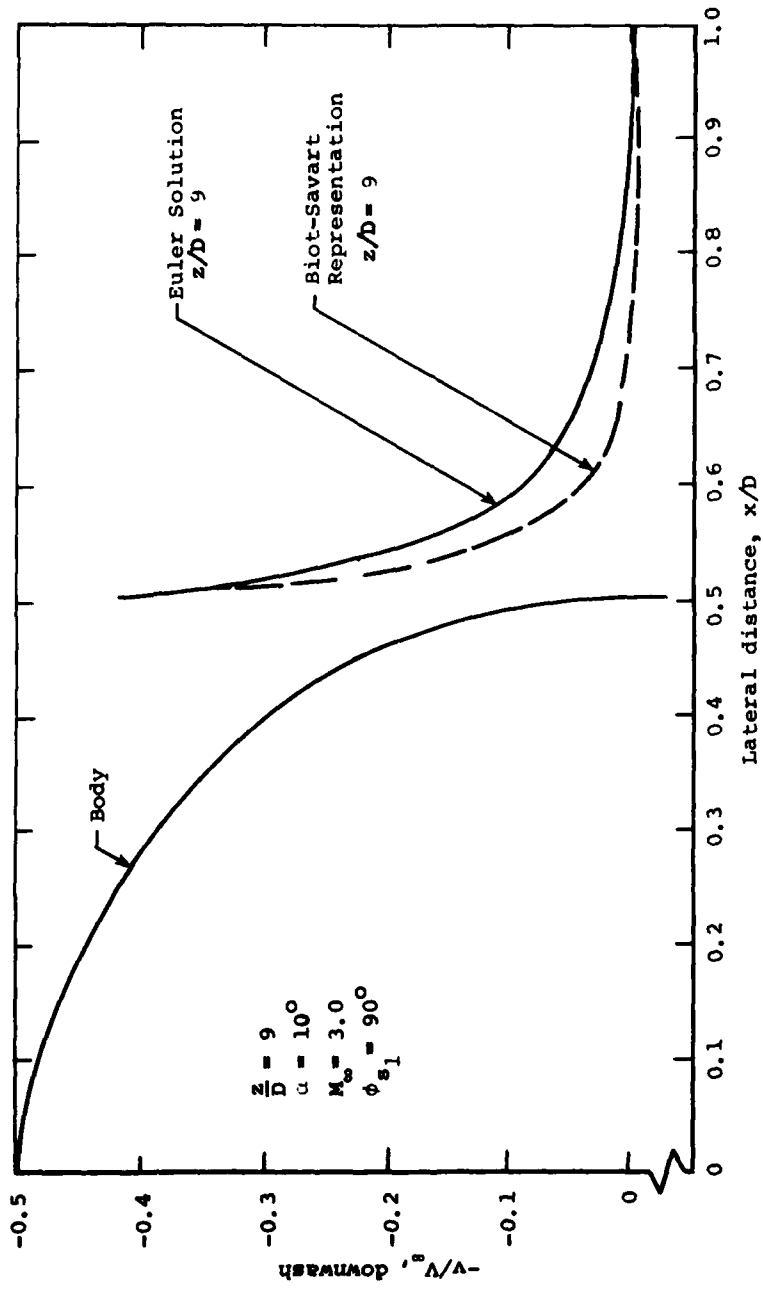
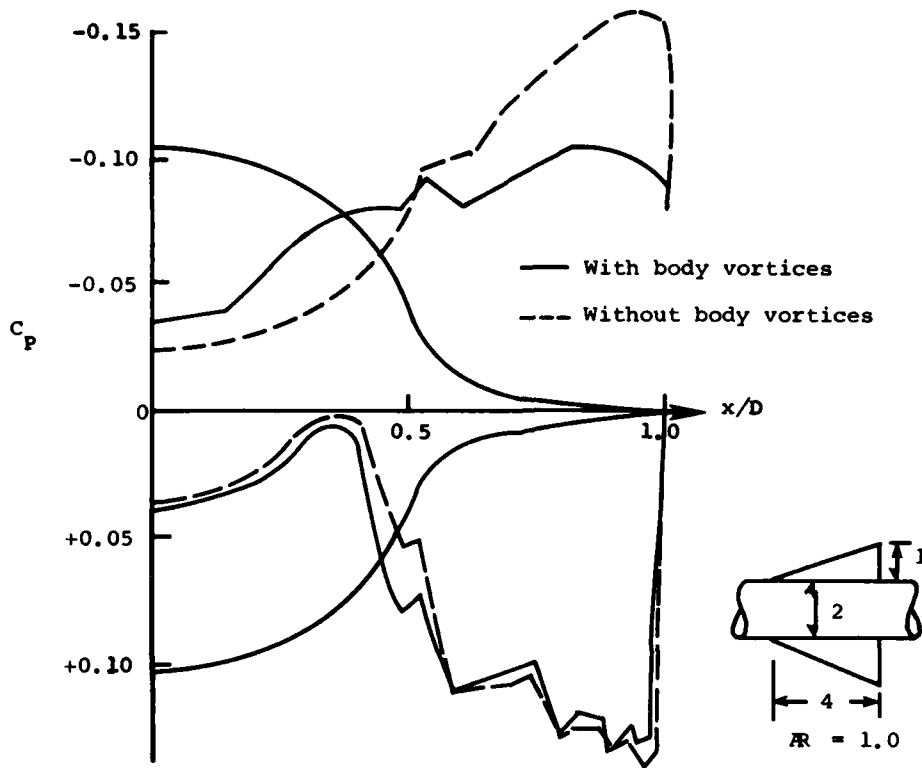
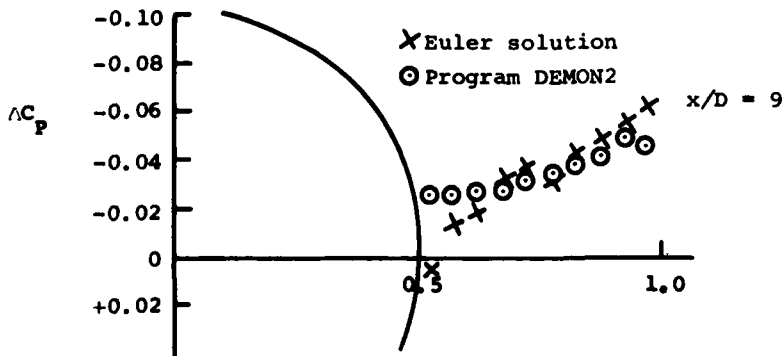


Figure 22.- Comparison of downwash distribution in front of fin as determined by Euler equations and Biot-Savart law.

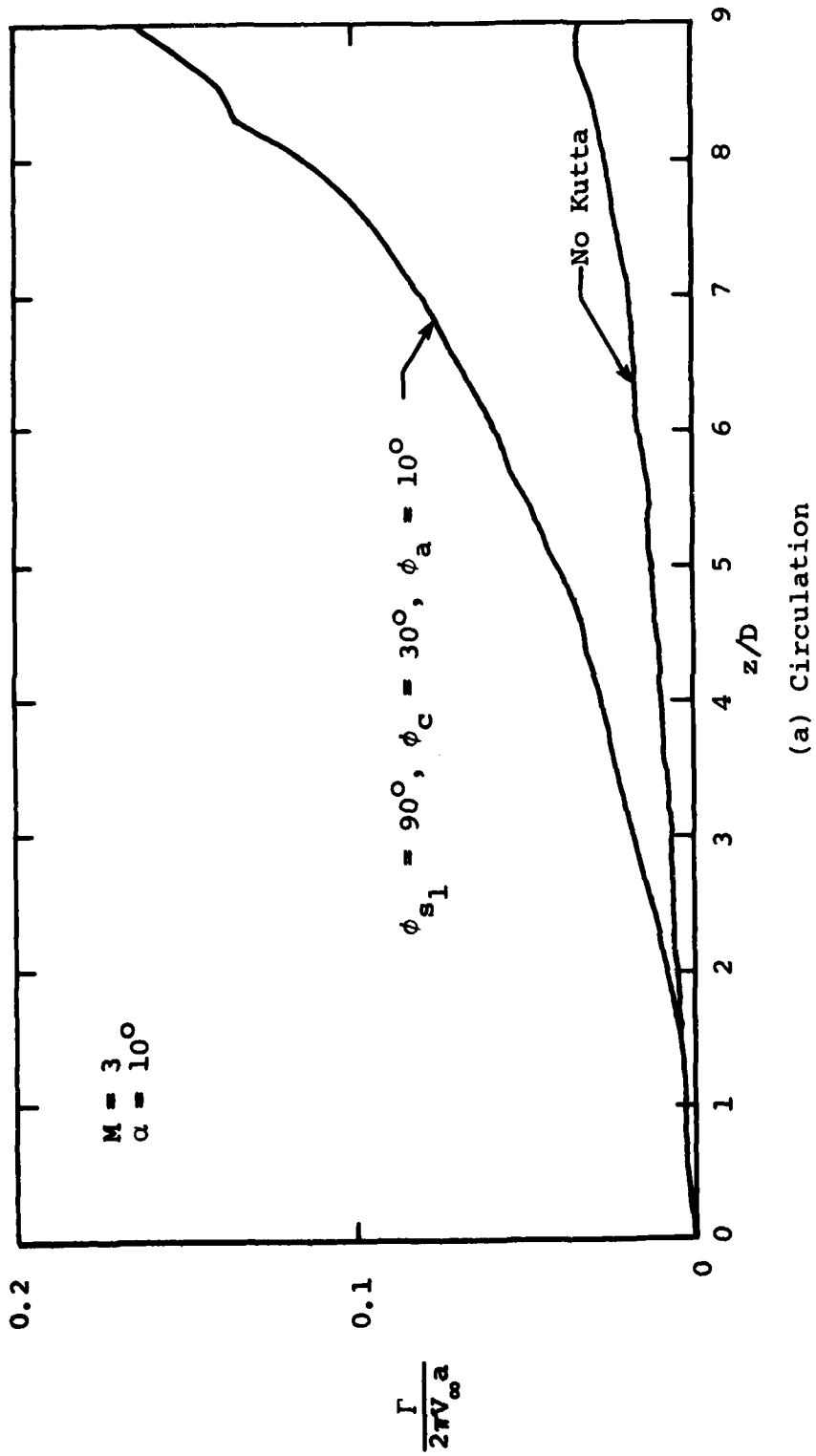


(a) Pressure distributions from Euler solutions



(b) Vortex loading distributions at trailing edge of fin.

Figure 23.- Pressure distribution on wing-body combination at fin trailing edge and fin vortex loading for a  $\alpha = 10^\circ$  and  $M_\infty = 3.0$ .



(a) Circulation

Figure 24.- Circulation and downwash distributions for example wing-body combination with and without Kutta condition.



DISTRIBUTION LIST

Technical Library  
Building 313  
Ballistic Research Laboratories  
Aberdeen Proving Ground, MD 21005

Mr. Aviars Celmins  
Ballistic Research Laboratory  
Ballistic Modelling Division  
Aberdeen Proving Ground, MD 21005

Dr. P. J. Roache  
Ecodynamics Research Associates, Inc.  
P. O. Box 8172  
Albuquerque, NM 87108

Defense Technical Information Center  
Cameron Station, Building 5  
Alexandria, VA 22314 (12)

Library  
Naval Academy  
Annapolis, MD 21402

Director, Tactical Technology Office  
Defense Advanced Research Projects  
Agency  
1400 Wilson Blvd.  
Arlington, VA 22209

Code 200B  
Office of Naval Research  
800 N. Quincy Street  
Arlington, VA 22217

Code 432  
Office of Naval Research  
800 N. Quincy Street  
Arlington, VA 22217 (2)

Dr. J. L. Potter  
Deputy Director, Technology  
von Karman Gas Dynamics Facility  
Arnold Air Force Station, TN 37389

Professor J. C. Wu  
School of Aerospace Engineering  
Georgia Institute of Technology  
Atlanta, GA 30332

Library  
Aerojet-General Corporation  
6352 North Irwindale Avenue  
Azusa, CA 91702

NASA Scientific and Technical  
Information Facility  
P. O. Box 8757  
Baltimore/Washington International  
Airport, MD 21240

Dr. K. C. Wang  
College of Engineering  
San Diego State University  
San Diego, CA 92182

Professor A. J. Chorin  
Department of Mathematics  
University of California  
Berkeley, CA 94720

Professor M. Holt  
Department of Mechanical Engineering  
University of California  
Berkeley, CA 94720

Dr. H. R. Chaplin  
Code 1600  
David W. Taylor Naval Ship Research  
and Development Center  
Bethesda, MD 20084

Dr. Hans Lugt  
Code 1802  
David W. Taylor Naval Ship Research  
and Development Center  
Bethesda, MD 20084

Dr. Francois Frenkiel  
Code 1802  
David W. Taylor Naval Ship Research  
and Development Center  
Bethesda, MD 20084

Dr. T. C. Tai  
Code 1606  
David W. Taylor Naval Ship Research  
and Development Center  
Bethesda, MD 20084

DISTRIBUTION LIST (Continued)

Dr. G. R. Inger  
Dept. of Aerospace Engineering  
University of Colorado  
Boulder, CO 80309

Professor C. H. Lewis  
Dept. of Aerospace and Ocean Engrg.  
Virginia Polytechnic Institute and  
State University  
Blacksburg, VA 24061

Professor A. H. Nayfeh  
Dept. of Engineering Science  
Virginia Polytechnic Institute and  
State University  
Blacksburg, VA 24061

Dr. A. Rubel  
Research Department  
Grumman Aerospace Corporation  
Bethpage, NY 11714

Commanding Officer  
Office of Naval Research  
Eastern/Central Regional Office  
666 Summer St., Bldg. 114, Section D  
Boston, MA 02210

Dr. J. C. Erickson, Jr.  
CALSPAN Corporation  
Advanced Technology Center  
P. O. Box 400  
Buffalo, NY 14225

Dr. T. J. Falk  
CALSPAN Corporation  
Advanced Technology Center  
P. O. Box 400  
Buffalo, NY 14225

Dr. C. Witliff  
CALSPAN Corporation  
Advanced Technology Center  
P. O. Box 400  
Buffalo, NY 14225

Prof. R. F. Probst  
Dept. of Mechanical Engineering  
Massachusetts Institute of Technology  
Cambridge, MA 02139

Commanding Officer  
Office of Naval Research Branch Office  
536 South Clark Street  
Chicago, IL 60605

Code 753  
Naval Weapons Center  
China Lake, CA 93555

Mr. J. Marshall  
Code 4063  
Naval Weapons Center  
China Lake, CA 93555

Professor R. T. Davis  
Dept. of Aerospace Engineering  
University of Cincinnati  
Cincinnati, OH 45221

Professor S. G. Rubin  
Dept. of Aerospace Engineering and  
Applied Mechanics  
University of Cincinnati  
Cincinnati, OH 45221

Library MS 60-3  
NASA Lewis Research Center  
21000 Brookpark Road  
Cleveland, OH 44135

Dr. J. D. Anderson, Jr.  
Chairman, Dept. of Aerospace Engrg.  
College of Engineering  
University of Maryland  
College Park, MD 20742

Professor O. Burggraf  
Dept. of Aeronautical and Astro-  
nautical Engineering  
Ohio State University  
1314 Kinnear Road  
Columbus, OH 43212

DISTRIBUTION LIST (Continued)

Technical Library  
Naval Surface Weapons Center  
Dahlgren Laboratory  
Dahlgren, VA 22448

Dr. F. Moore  
Naval Surface Weapons Center  
Dahlgren Laboratory  
Dahlgren, VA 22448

Technical Library 2-51131  
LTV Aerospace Corporation  
P. O. Box 5907  
Dallas, TX 75222

Library, United Aircraft Corporation  
Research Laboratories  
Silver Lane  
East Hartford, CT 06108

Professor G. Moretti  
Polytechnic Institute of New York  
Long Island Center  
Dept. of Aerospace Engrg. and  
Applied Mechanics  
Route 110  
Farmingdale, NY 11735

Dr. W. R. Briley  
Scientific Research Associates, Inc.  
P. O. Box 498  
Glastonbury, CT 06033

Professor P. Gordon  
Calumet Campus  
Dept. of Mathematics  
Purdue University  
Hammond, IN 46323

Library (MS 185)  
NASA Langley Research Center  
Langley Station  
Hampton, VA 23665

Professor A. Chapmann  
Chairman, Mechanical Engineering Dept.  
William M. Rice Institute  
Box 1892  
Houston, TX 77001

Technical Library  
Naval Ordnance Station  
Indian Head, MD 20640

Professor D. A. Caughey  
Sibley School of Mechanical and  
Aerospace Engineering  
Cornell University  
Ithaca, NY 14850

Professor E. L. Resler  
Sibley School of Mechanical and  
Aerospace Engineering  
Cornell University  
Ithaca, NY 14850

Professor S. F. Shen  
Sibley School of Mechanical and  
Aerospace Engineering  
Cornell University  
Ithaca, NY 14850

Library  
Midwest Research Institute  
425 Volker Boulevard  
Kansas City, MO 64110

Dr. M. M. Hafez  
Flow Research, Inc.  
P. O. Box 5040  
Kent, WA 98031

Dr. E. M. Murman  
Flow Research, Inc.  
P. O. Box 5040  
Kent, WA 98031

Dr. J. J. Riley  
Flow Research, Inc.  
P. O. Box 5040  
Kent, WA 98031

DISTRIBUTION LIST (Continued)

Dr. S. A. Orszag  
Cambridge Hydrodynamics, Inc.  
54 Baskin Road  
Lexington, MA 02173

Dr. P. Bradshaw  
Imperial College of Science and  
Technology  
Department of Aeronautics  
Prince Consort Road  
London SW7 2BY, England

Professor T. Cebeci  
Mechanical Engineering Department  
California State University, Long  
Beach  
Long Beach, CA 90840

Dr. H. K. Cheng  
University of Southern California  
Department of Aerospace Engrg.  
University Park  
Los Angeles, CA 90007

Professor J. D. Cole  
Mechanics and Structures Department  
School of Engineering and Applied  
Science  
University of California  
Los Angeles, CA 90024

Engineering Library  
University of Southern California  
Box 77929  
Los Angeles, CA 90007

Dr. C. -M. Ho  
Dept. of Aerospace Engineering  
University of Southern California  
University Park  
Los Angeles, CA 90007

Commanding Officer  
Naval Ordnance Station  
Louisville, KY 40214

Mr. B. H. Little, Jr.  
Lockheed-Georgia Company  
Department 72-74, Zone 369  
Marietta, GA 30061

Professor E. R. G. Eckert  
University of Minnesota  
241 Mechanical Engineering Bldg.  
Minneapolis, MN 55455

Dr. Gary Chapman  
Mail Stop 227-4  
Ames Research Center  
Moffett Field, CA 94035

Library  
Naval Postgraduate School  
Monterey, CA 93940

Dr. J. L. Steger  
Dept. of Aeronautics and Astronautics  
Durand Building  
Stanford University  
Stanford, CA 94305

Dr. S. S. Stahara  
Nielsen Engineering & Research, Inc.  
510 Clyde Avenue  
Mountain View, CA 94043

Engineering Societies Library  
345 East 47th Street  
New York, NY 10017

Professor A. Jameson  
Mechanical and Aeronautical Engrg.  
Dept.  
Princeton University  
E Quad  
Princeton, NJ 08540

DISTRIBUTION LIST (Continued)

Professor G. Miller  
Dept. of Applied Science  
New York University  
26-36 Stuyvesant Street  
New York, NY 10003

Office of Naval Research  
New York Area Office  
715 Broadway - 5th Floor  
New York, NY 10003

Dr. A. Vaglio-Laurin  
Dept. of Applied Science  
New York University  
26-36 Stuyvesant Street  
New York, NY 10003

Mr. D. Farmer  
Naval Ocean Research and Development  
Activity  
Code 332  
NSTL Station, MS 39522

Librarian, Aeronautical Library  
National Research Council  
Montreal Road  
Ottawa 7, Canada

Lockheed Missiles and Space Company  
Technical Information Center  
3251 Hanover Street  
Palo Alto, CA 94304

Commanding Officer  
Office of Naval Research Western  
Regional Office  
1030 East Green Street  
Pasadena, CA 91106

Engineering Division  
California Institute of Technology  
Pasadena, CA 91109

Library  
Jet Propulsion Laboratory  
4800 Oak Grove Drive  
Pasadena, CA 91103

Professor H. Liepmann  
Department of Aeronautics  
California Institute of Technology  
Pasadena, CA 91109

Mr. L. I. Chasen, MGR-MSD Lib.  
General Electric Company  
Missile and Space Division  
P. O. Box 8555  
Philadelphia, PA 19101

Technical Library  
Naval Missile Center  
Point Mugu, CA 93042

Professor S. Bogdonoff  
Gas Dynamics Laboratory  
Dept. of Aerospace & Mechanical Sci.  
Princeton University  
Princeton, NJ 08540

Professor S. I. Cheng  
Dept. of Aerospace & Mechanical Sci.  
Princeton University  
Princeton, NJ 08540

Dr. J. E. Yates  
Aeronautical Research Associates of  
Princeton, Inc.  
50 Washington Road  
Princeton, NJ 08540

Professor L. Sirovich  
Division of Applied Mathematics  
Brown University  
Providence, RI 02912

Redstone Scientific Information Center  
Chief, Document Section  
Army Missile Command  
Redstone Arsenal, AL 35809

U.S. Army Research Office  
P. O. Box 12211  
Research Triangle Park, NC 27709

DISTRIBUTION LIST (Continued)

Editor, Applied Mechanics Review  
Southwest Research Institute  
8500 Culebra Road  
San Antonio, TX 78228

Library and Information Services  
General Dynamics-CONVAIR  
P. O. Box 1128  
San Diego, CA 92112

Dr. R. Magnus  
General Dynamics-CONVAIR  
Kearny Mesa Plant  
P. O. Box 80847  
San Diego, CA 92138

Office of Naval Research  
San Francisco Area Office  
One Hallidie Plaza, Suite 601  
San Francisco, CA 94102

Library  
The RAND Corporation  
1700 Main Street  
Santa Monica, CA 90401

Dr. P. E. Rubbert  
Boeing Aerospace Company  
Boeing Military Airplane Development  
Organization  
P. O. Box 3707  
Seattle, WA 98124

Dr. H. Yoshihara  
Boeing Aerospace Company  
P. O. Box 3999  
Mail Stop 41-18  
Seattle, WA 98124

Librarian  
Naval Surface Weapons Center  
White Oak Laboratory  
Silver Spring, MD 20910

Dr. J. M. Solomon  
Naval Surface Weapons Center  
White Oak Laboratory  
Silver Spring, MD 20910

Professor J. H. Ferziger  
Dept. of Mechanical Engineering  
Stanford University  
Stanford, CA 94305

Professor K. Karamchetti  
Dept. of Aeronautics and Astronautics  
Stanford University  
Stanford, CA 94305

Professor O. Bunemann  
Institute for Plasma Research  
Stanford University  
Stanford, CA 94305

Engineering Library  
McDonnell Douglas Corporation  
Department 218, Building 101  
P. O. Box 516  
St. Louis, MO 63166

Dr. R. J. Hakkinen  
McDonnell Douglas Corporation  
Department 222  
P. O. Box 516  
St. Louis, MO 63166

Dr. N. Malmuth  
Rockwell International Science Center  
1049 Camino Dos Rios  
P. O. Box 1085  
Thousand Oaks, CA 91360

Library  
Institute of Aerospace Studies  
University of Toronto  
Toronto 5, Canada

Professor W. R. Sears  
Aerospace and Mechanical Engineering  
University of Arizona  
Tucson, AZ 95721

Professor A. R. Seebass  
Dept. of Aerospace and Mechanical  
Engineering  
University of Arizona  
Tucson, AZ 95721

DISTRIBUTION LIST (Concluded)

Dr. K. T. Yen  
Code 3015  
Naval Air Development Center  
Warminster, PA 18974

Air Force Office of Scientific  
Research (SREM)  
Building 410, Bolling AFB  
Washington, DC 20332

Chief of Research and Development  
Office of Chief of Staff  
Department of the Army  
Washington, DC 20310

Library of Congress  
Science and Technology Division  
Washington, DC 20540

Director of Research (Code RR)  
National Aeronautics and Space  
Administration  
600 Independence Avenue, SW  
Washington, DC 20546

Library  
National Bureau of Standards  
Washington, DC 20234

National Science Foundation  
Engineering Division  
1800 G Street, NW  
Washington, DC 20550

AIR 320D  
Naval Air Systems Command  
Washington, DC 20361

AIR 950D  
Naval Air Systems Command  
Washington, DC 20375

Code 2627  
Naval Research Laboratory  
Washington, DC 20375

SEA 03512  
Naval Sea Systems Command  
Washington, DC 20362

Phillip J. Andrews  
SEA 61R2  
Naval Sea Systems Command  
Washington, DC 20362

Dr. Charles Watkins  
Head, Mechanical Engineering Dept.  
Howard University  
Washington, DC 20059

Dr. A. L. Slafkosky  
Scientific Advisor  
Commandant of the Marine Corps (Code AX)  
Washington, DC 20380

Director  
Weapons Systems Evaluation Group  
Washington, DC 20350

Research Library  
AVCO Corporation  
Missile Systems Division  
201 Lowel Street  
Wilmington, MA 01887

AFAPL (APRC)  
AB  
Wright Patterson AFB, OH 45433

Dr. Donald J. Harney  
AFFDL/FX  
Wright Patterson AFB, OH 45433

Flow Research  
1320 Fenwick Lane  
Suite 401  
Silver Spring, MD 20910